

Stellingen behorende bij het proefschrift  
'Artificial atoms and molecules'

T.H. Oosterkamp

1. Het modelleren van een halfgeleider quantum dot is eenvoudiger dan het meten eraan.
2. Gezien de sterke koppeling tussen kunstmatige atomen en fononen in GaAs zijn deze in principe geschikt voor cavity QAD (quantum acousto-dynamics) experimenten.
3. Een gedetailleerde interpretatie van Kondo data in quantum dots wordt bemoeilijkt doordat het niet verstoorte spectrum moeilijk afzonderlijk kan worden gemeten; verticale en kleine dubbele quantum dots kunnen hier mogelijk uitkomst bieden.
4. De mens is geen individu.
5. Iemand die zich onder leden van een corporale vereniging begeeft, vergaat het als een kind in een ballenbad; als de ballendichtheid (bij gelijkblijvend volume) een zekere kritieke waarde overschrijdt, vindt er een faseovergang plaats.
6. Het overgrote deel van de ongelijkheid tussen mannen en vrouwen is terug te voeren op de grote moeite die het baren van kinderen met zich mee brengt.  
(Genesis 3:16)

7. Niet de mens is de kroon op Gods schepping, maar de sabbat; zo is in het wetenschappelijk bedrijf naast de transpiratie en de inspiratie een belangrijke rol voor de expiratie weggelegd.  
(proefschrift Jan J. Boersema, *Thora en Stoa over mens en natuur*, Callenbach, Baarn 1997)
8. Zolang het Nederlands voetbalelftal iets ter verontschuldiging weet aan te voeren na een verloren wedstrijd, wordt het geen kampioen.
9. De fietsenstalling voor menig groot station vertoont belangrijke overeenkomsten met de harde-schijfruimte op een computer.
10. Omwille van de symmetrie zou het overerven van de achternaam van moeder op dochter en van vader op zoon moeten geschieden.

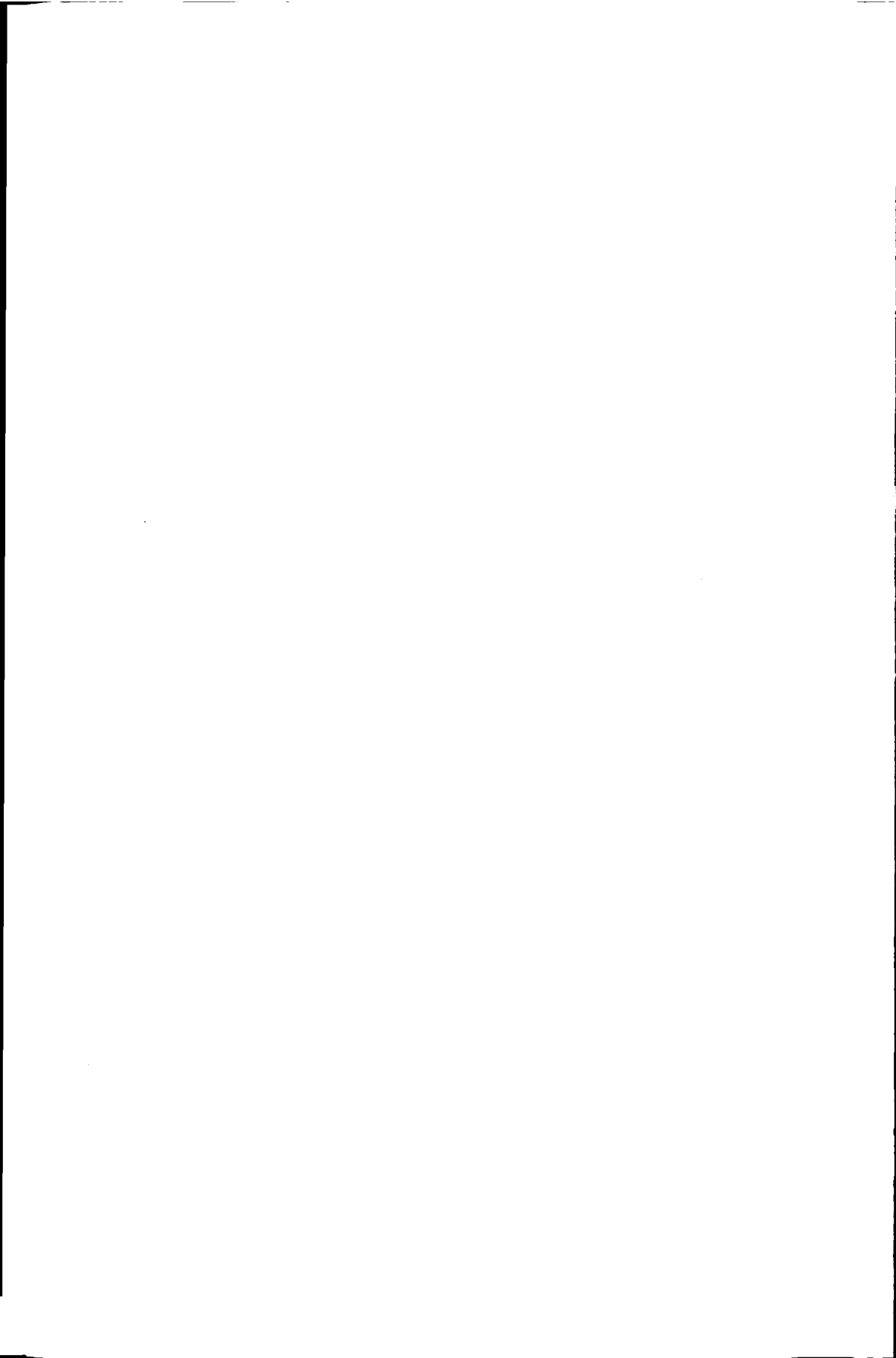
TR3281

2009/6/1

714000

300

**Artificial Atoms and Molecules:  
on manybody effects and coherence  
in semiconductor quantum dots.**



**Artificial Atoms and Molecules:  
on manybody effects and coherence  
in semiconductor quantum dots.**



**Proefschrift**

ter verkrijging van de graad van doctor  
aan de Technische Universiteit Delft,  
op gezag van de Rector Magnificus Prof. ir. K. F. Wakker,  
in het openbaar te verdedigen ten overstaan van een commissie  
door het College voor Promoties aangewezen,  
op vrijdag 22 januari 1999 te 10:30 uur

door

**Tjerk Hendrik OOSTERKAMP**

natuurkundig ingenieur  
geboren te Eindhoven

Dit proefschrift is goedgekeurd door de promotor:

Prof. dr. ir. J. E. Mooij

Samenstelling van de promotiecommissie:

Rector Magnificus,	voorzitter
Prof. dr. ir. J.E. Mooij,	Technische Universiteit Delft, promotor
Dr. ir. L.P. Kouwenhoven,	Technische Universiteit Delft, toegevoegd promotor
Prof. dr. ir. G. Bauer,	Technische Universiteit Delft
Prof. S. Tarucha,	Tokyo University and NTT Basic Research
Prof. dr. ir. T. Klapwijk,	Rijksuniversiteit Groningen
Prof. dr. A. Lagendijk,	Universiteit van Amsterdam
Prof. dr. C. Beenakker,	Universiteit Leiden

Het onderzoek beschreven in dit proefschrift is financieel ondersteund door de stichting voor Fundamenteel Onderzoek der Materie (F.O.M.).

Printed by:

Beeld en Grafisch Centrum, Facilitair Bedrijf

Kanaalweg 2 B

2628 EB Delft

The Netherlands

telephone: +31-15-2786012

fax: +31-15-2781749

Copyright © 1999 by T.H. Oosterkamp

All rights reserved. No part of the material protected by this copyright notice may be reproduced or utilized in any form or by any means, electronic or mechanical, including photocopying, recording or by any information storage and retrieval system, without permission from the author.

Printed in the Netherlands

# Preface

*De meetsnoeren vielen mij in liefelijke dreven,  
ja, mijn erfdeel bekoort mij. Psalm 16:6*

This thesis describes a number of experiments on *semiconductor quantum dots* performed from 1994 to 1998 in the Quantum Transport group of Prof. J.E. Mooij at Delft University of Technology. Quantum dots are small conductive regions in a semiconductor that contain a tunable number of electrons. They are often referred to as '*artificial atoms*', because the electrons are confined to an artificially made puddle, in much the same way as electrons are confined to the region around the nucleus of an atom. And although the shape of the confinement potential in artificial atoms is different from that of atoms they display much of the same physics. One of the properties that the electrons in quantum dots share with those in atoms is that they occupy discrete states. In other words, the energy of an electron in an atom or in a quantum dot cannot just have any value, the electron can only move in fixed orbitals. The yellow light coming from the sodium lightbulbs along dutch highways is a consequence of this fact. Due to the heat produced by the electricity in the light bulb, electrons are promoted from orbitals with low energy to orbitals with higher energy. As the electrons fall back again to an orbital with low energy, they emit light. The color of the light produced is determined by the energy difference between these states, and in sodium atoms the color of the emitted light turns out to be yellow.

Because we can vary the shape and the size of our quantum dots we can study the properties and interactions between the electrons in greater detail than is possible in atoms. A large part of this thesis discusses the discrete states (or orbitals) in quantum dots and how they change with a magnetic field. Some of our results can be understood with a model in which the interactions between the electrons on the quantum dot are greatly simplified. We have been especially interested in deviations from this simple model due to the interactions between the electrons. Such *many body effects* teach us how the electrons really interact and how this affects their energy levels.

If we can make an artificial atom, a natural question to ask is, whether it is also possible to combine two artificial atoms to form an *artificial molecule*. Technically it is not so difficult to fabricate two quantum dots very close together. It was much more difficult to show that when an electron can hop back and forth between two quantum dots, new molecular orbitals are formed. Whether this happens depends on the *coherence* of the system. We have shown that there are indeed molecular states that extend over both dots, by inducing transitions between them with light of an energy that matched their energy difference.

The research described in this thesis, is very much a group effort. It has been stimulating to work in the large group of Prof. Mooij. The way his group is organized provided a lot of colleagues to discuss with, an infrastructure that I have seen nowhere else and many visitors from different parts of the world. It has been very exciting and enjoyable to be part of the combined group effort that resulted in the publication of 10 articles in *Nature*, *Science* or *PRL* within one year. A lot of people have contributed to this thesis: people that fabricated samples, visitors, undergraduate students and a lot of colleagues.

None of the devices that are described in this thesis were fabricated by myself. The vertical quantum dots described in this thesis were fabricated by Guy Austing, who kindly provided the photos on the cover, Takashi Honda and Seigo Tarucha at NTT Basic Research Laboratories. I have been very fortunate to work with you. The year that Tarucha-san visited was enjoyable and turned out to be very valuable. Also from NTT visited Toshimasa Fujisawa, once our main competitor, with his lateral double dot sample. Measuring his double dot in our fridge, we could finally see the artificial molecule that we had been looking for so long. The other lateral quantum dots I had inherited from Nijs van der Vaart, when he left our group. He fabricated them together with Sandra Godijn and Bram van der Enden. Making good small quantum dots is no small accomplishment. It is a miracle that their samples have survived for such a long time.

It was great also to work with other visitors from abroad: Sara Cronenwett, when I brought the Kondo wine to your thanksgiving dinner I was close to bluffing. I am glad it turned out that we had really seen the Kondo effect. Koji Ishibashi, thank you for coming to measure with us and for bringing your sons to the lab in the weekends. The sauna in Japan was great. Michel Devoret, your politeness is exemplary, so is your approach to understanding the measurement data.

In Delft there are a lot of people I would like to thank. First of all there is Leo Kouwenhoven, my supervisor. I was fortunate to work with you and the many opportunities you created. Your continuous drive for concrete results has been very stimulating and productive. Your almost neverending criticism when it comes to writing has made every paper into a long story. I am glad there was the fridge where I could always start a new project before finishing the paper. Thank you also to prof. Hans Mooij, and the other staff members, Kees Harmans, Peter Hadley, Cees Dekker, Herre van der Zant and Bram van der Enden. I am proud of QT.

I would like to thank all the QT group members for making it fun to come to work. In particular I would like to mention Sander Tans, firm believer of Darwin



Sociology, Luuk Mur, Wilfred van der Wiel, inventor of the Quantum Explosion Device and director of the Wiellab's secret work on the artificial atom bomb, and my office mates Caspar van der Wal, Nijs van der Vaart, Erik Visscher, Henk Postma and Yann Kervennic.

I thank Bram van der Enden ('that will take about two weeks'), Leo Lander, Wim Schot, Willem den Braver (I never really ran out of helium), Gerard van der Gaag, Masscha van Oossanen and Anneke Delsing, for their technical assistance. I never learned how a pump works, I just press the button. If that doesn't help, I call you. I thank Ria van Heeren-van der Kramer for her assistance, travel arrangements and tea.

There is also life outside QT. On my way to the fridge I had to always pass the cookies and cake of HF. Thanks to Niels Hovenier, Tjeerd Klaassen and of course Raymond Schouten, for good small and physics talk on the way to the fridge. Raymond, thank you for all the electronics.

I also owe very much to the nanophysics group. Thank you to Bart Geerligs, Pieter Lukey and Jaap Caro for the discussions, pumps, cables and the fridge.

Bram Huis has two hands full of gold. The workshop will never be the same without him.

Thanks also to the theorists up above. The monday theory meetings that I attended ('Why do I have to interrogate you like this?'), always made for good conversation at lunch. Theo Stoof, your laugh I can hear a mile away; Mark Visscher, the best stop on the way to the library; Yuli 'what is actual orientation of frog?' Nazarov and Gerrit Bauer. The bookclub taught me some respect but of course the real work is done downstairs.

A lot of hours went into this thesis work. Most of the hours were put in by the undergraduate students. I want to thank -Armand Koolen, for photon assisted tunneling. I was very lucky to start my thesis work with you. Your programming has lasted and has paid off well; -Rob van der Hage, for generalized Hund's rule. The large datafiles you measured have really set a trend. Good luck in moving large amounts of money; -Jorg Janssen, for the MDD and many other things. Quenching a magnet at 17.5 Tesla is not something I would like to have done alone. Thank you for the copper powder filters; -Remko Hijman, for the double quantum dots. The molecule was too noisy at first but we got it after all; -Martin Danoesastro, for the excited states. Too bad the Pathfinder landed on Mars when we published. But now we finally made it onto a cover; -Benno Broer, for the relaxation times. Manager, consultant and headhunter. You know how to get a job done. I hope I'll finish my part of the paper soon; -Michiel Uilenreef, for the magnetization and the inelastic processes in the double dot. We should really get a temperature controller on our fridge now; -Michael Janus, for the Wigner

crystal that played 'kiekeboe' with us. You were thorough; Thank you all for so much Helium. It was a pleasure to work with you.

Thank you also to my family. In 1939 my grandfather got his Ph.D. in physics. His second son, my father, got his Ph.D. in 1969, in physics. I had a choice. Hanne, you were the best imaginable distraction during the time I had to write my thesis.

Jannette, thank you for bearing with me. You were the only one that reliably predicted the date of my thesis defense a year ago. It is comforting to know I have someone around, who is always right:

*Het duurt altijd langer dan je denkt  
ook als je denkt  
het zal wel langer duren dan ik denk  
dan duurt het toch nog langer  
dan je denkt*

*Maar ook:  
Het duurt veel korter dan je denkt  
ook als je denkt  
het zal wel korter duren dan ik denk  
dan duurt het toch  
nog korter dan je denkt.*

Tjerk Oosterkamp  
Delft, December 1998

# Contents

<b>1</b>	<b>Introduction</b>	<b>1</b>
1.1	Quantized charge tunneling . . . . .	2
1.2	Samples . . . . .	3
1.3	Measurement techniques . . . . .	5
1.3.1	filtering . . . . .	5
1.3.2	interference . . . . .	5
1.3.3	sample stability . . . . .	6
1.3.4	measurement electronics . . . . .	7
1.3.5	high frequency coax . . . . .	7
1.4	This thesis . . . . .	8
	References . . . . .	8
<b>2</b>	<b>Electron ground states in a few-electron quantum dot</b>	<b>11</b>
2.1	Introduction . . . . .	12
2.2	Device parameters and experimental set up . . . . .	13
2.3	Addition energies and shell filling . . . . .	16
2.4	Constant Interaction Model . . . . .	18
2.5	Single particle states of a 2D harmonic oscillator . . . . .	19
2.6	Magnetic field dependence of ground states . . . . .	22
2.7	Hund's rule and exchange energy . . . . .	25
2.8	Singlet - triplet transition . . . . .	27
	References . . . . .	32
<b>3</b>	<b>Excitation spectra of circular, few-electron quantum dots</b>	<b>35</b>
<b>4</b>	<b>Stability of the maximum density droplet in quantum dots at high magnetic fields</b>	<b>49</b>
<b>5</b>	<b>Spectroscopy in lateral quantum dots</b>	<b>59</b>

---

<b>6 Photon assisted tunneling in a single quantum dot</b>	<b>69</b>
6.1 Introduction . . . . .	70
6.2 PAT through a single junction . . . . .	70
6.3 The 0D-model based on a master equation . . . . .	72
6.4 Pumped current . . . . .	75
6.5 Experiments . . . . .	77
6.5.1 pumping . . . . .	78
6.5.2 low frequency regime . . . . .	81
6.5.3 high frequency regime . . . . .	81
6.5.4 frequency dependence . . . . .	82
6.5.5 magnetic field dependence . . . . .	83
6.5.6 power dependence . . . . .	85
References . . . . .	87
<b>7 Microwave spectroscopy of a quantum dot molecule</b>	<b>89</b>
<b>8 Spontaneous emission spectrum in double quantum dot devices</b>	<b>99</b>
<b>9 A tuneable Kondo effect in quantum dots</b>	<b>109</b>
Summary	121
Samenvatting	125
Curriculum Vitae	129
List of publications	131

# Chapter 1

## Introduction

The continuing miniaturization of solid state devices has raised the question how small transistors can be made without changing their properties. People interested in making increasingly more powerful computers will try to avoid these new properties, because things work fine as they are. Judging from the fact that the increasing performance of computers makes it worthwhile to buy a new computer every few years, they are quite successful at it. Other people prefer to ask how one can make devices that have fundamentally new properties, and where these come from.

The new properties that we are particularly interested in are those that arise from quantum mechanics or the quantization of charge in units of  $e$ . Mesoscopic physics is a subsection of solid state physics and studies systems with sizes in-between the microscopic and the macroscopic, where these effects play an important role. It is a mature field and many material systems and geometries have been studied. Examples include thin films, quantum point contacts, small superconducting devices, and many others [1].

This thesis focuses on electron transport through semiconductor quantum dots. Reviews on this subject can be found in Refs. [?]. Quantum dots are small conductive areas in a semiconductor, made of roughly a million atoms with an equivalent number of electrons. Virtually all of the electrons are tightly bound to the nuclei of the atoms, however, and the number of free electrons in the dot can be very small; from one to roughly a thousand. Connecting a dot to current and voltage contacts allows the properties of its free electrons to be probed by charge-transport measurements. The wavelength of the free electrons in the dot is comparable to the size of the dot, as is the case for atoms where the wavelength of the electrons orbiting a nucleus is comparable to the size of the atom. The electrons occupy well defined discrete quantum states and have a discrete excitation spectrum.

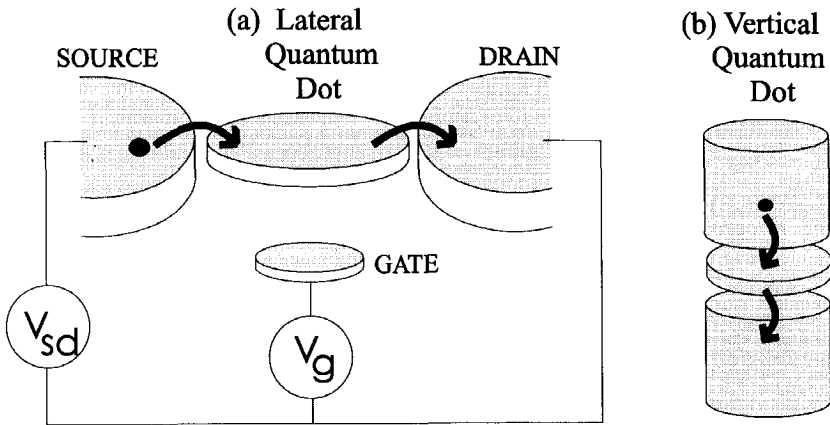


Figure 1.1: Schematic of a quantum dot, in the shape of a disk, connected to source and drain contacts by tunnel junctions and to a gate by a capacitor. (a) shows the lateral geometry and (b) the vertical geometry.

A quantum dot has another characteristic, usually called the charging energy, which is analogous to the ionization energy of an atom. This is the energy required to add or remove a single electron from the dot. Because of the analogies to real atoms, quantum dots are sometimes referred to as artificial atoms [2].

## 1.1 Quantized charge tunneling

In this section we examine the circumstances under which Coulomb charging effects are important. Let us consider the electronic properties of the small conductor depicted in Fig. 1.1a which is coupled to three terminals. Particle exchange can occur with only two of the terminals, as indicated by the arrows. These source and drain terminals connect the small conductor to macroscopic current and voltage meters. The third terminal provides an electrostatic or capacitive coupling and can be used as a gate electrode. If we first assume that there is no coupling to the source and drain contacts, then our small conductor acts as an island for electrons. The number of electrons on this island is an integer  $N$ , i.e. the charge on the island is quantized and equal to  $Ne$ . If we now allow tunneling to the source and drain electrodes, then the number of electrons  $N$  adjusts itself until the energy of the whole circuit is minimized.

When tunneling occurs, the charge on the island suddenly changes by the quantized amount  $e$ . The associated change in the Coulomb energy is conve-

niently expressed in terms of the capacitance  $C$  of the island. An extra charge  $e$  changes the electrostatic potential by the charging energy  $E_c = e^2/C$ . This charging energy becomes important when it exceeds the thermal energy  $k_B T$ . A second requirement is that the barriers are sufficiently opaque such that the electrons are located either in the source, in the drain, or on the island. This requirement translates to a lower bound for the tunnel resistances  $R_t$  of the barriers. To see this, consider the typical time to charge or discharge the island  $\Delta t = R_t C$ . Furthermore, for the charge to be quantized, the energy uncertainty  $\Delta E$  must be much smaller than the charging energy. The Heisenberg uncertainty relation  $\Delta E \Delta t = (e^2/C) R_t C \geq h$  then implies that  $R_t$  should be much larger than the resistance quantum  $h/e^2 = 25.8 \text{ k}\Omega$ . To summarize, the two conditions for observing effects to the discrete nature of charge are [4, 5]:

$$R_t \gg h/e^2 \quad (1.1)$$

$$e^2/C \gg k_B T \quad (1.2)$$

The first criterion can be met by weakly coupling the dot to the source and drain leads. The second criterion can be met by making the dot sufficiently small.

While the tunneling of a single charge changes the electrostatic energy of the island by a discrete value, a voltage  $V_g$  applied to the gate can change the island's electrostatic energy in a continuous manner. In terms of charge, tunneling changes the island's charge by an integer while the gate voltage induces an effective continuous charge  $q = C_g V_g$  that represents, in some sense, the charge that the dot would like to have. This charge is continuous even on the scale of the elementary charge  $e$ . If we sweep  $V_g$  the build up of the induced charge will be compensated in periodic intervals by tunneling of discrete charges onto the dot. This competition between continuously induced charge and discrete compensation leads to so-called Coulomb oscillations in a measurement of the current, as a function of gate voltage at a fixed source drain voltage.

## 1.2 Samples

In this thesis we have studied GaAs quantum dots formed in two different geometries, both with their specific advantages. In a vertical quantum dot (Fig. 1.2a and b) the current flows vertically while in a lateral quantum dot (Fig. 1.2c and d) the current flows laterally.

Our vertical quantum dot is a miniaturized resonant tunneling diode [7]. The pillar in Fig. 1.2a is etched from a semiconductor double-barrier heterostructure (DBH) and a metal gate electrode is deposited around it. On the InGaAs dot,

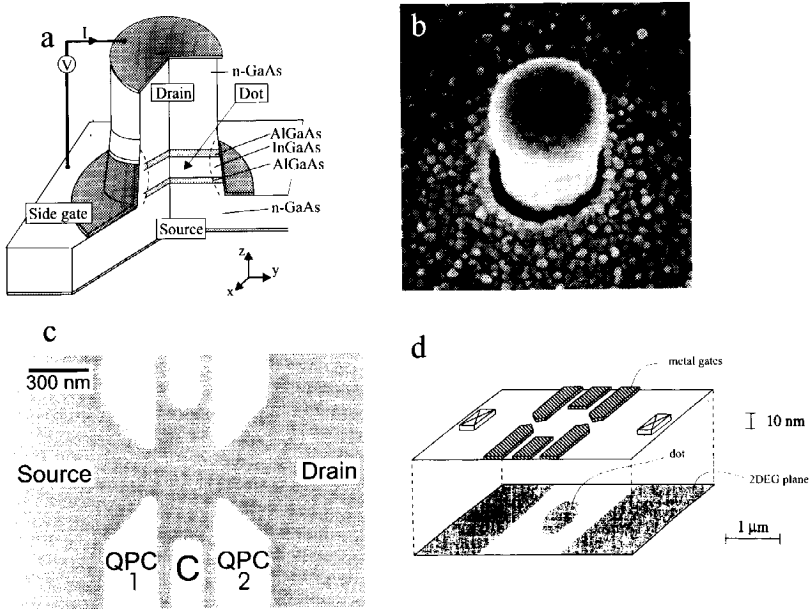


Figure 1.2: a) Schematic and (b) scanning electron microscope (SEM) photo of the top contact and the gate metal of a vertical quantum dot. The diameter of the pillar is  $0.5 \mu\text{m}$ . The bottom contact is not visible. c) A SEM photo of a typical lateral quantum dot device defined in a GaAs/AlGaAs heterostructure. d) Schematic of a lateral sample. The 2DEG is  $\sim 100 \text{ nm}$  below the surface. Negative voltages applied to the surface gates (i.e. the light areas in c) deplete the 2DEG underneath. The resulting dot contains a few electrons which are coupled via tunnel barriers to the large 2DEG regions. The tunnel barriers can be tuned individually with the voltages applied to the left/right pair of gates.

that is located between the two AlGaAs barriers, the electrons are confined in all three directions. Electrons can tunnel vertically through the barriers, which allows a current to flow. The number of electrons on the dot can be tuned by the voltage applied to the gate. They show very good symmetry and the number of electrons on the dot can be reduced down to zero. Because the barriers are due to the larger bandgap of AlGaAs, the barriers are not influenced by the gate voltage applied, unlike in the lateral quantum dots discussed below. Once the barrier thickness is chosen, however, the tunnel rates from the dot to the leads



can not be changed.

A lateral quantum dot is patterned from a two dimensional electron gas (2DEG) that is formed in a GaAs/AlGaAs heterostructure. When an AlGaAs crystal is grown on top of a GaAs crystal, the electrons coming from remote dopants form a 2DEG in the potential minimum that occurs at the interface between the two crystals, approximately 100 nm below the surface. The electrons are then confined in the  $z$ -direction and can be confined in the other directions by a suitable electric field that is applied through metallic gates that are patterned at the surface (Fig. 1.2c). They have the advantage that the tunnel rates through the barrier can be tuned by the voltage on the gates forming the tunneling barrier. They do not have the symmetry of the vertical quantum dots, however, and for small dots the barrier heights tend to change significantly when the electron number is changed.

## 1.3 Measurement techniques

To observe the effects of the atom-like orbitals and the charging energy on transport, the thermal energy  $k_B T$  must be well below the energy scales of the dot, which correspond to temperatures of order 1 K ( $k_B T = 86 \mu\text{eV}$  at 1K). Therefore, our experiments were performed in a dilution refrigerator that can cool down to 10 mK. Special care must be taken to avoid spurious heating of the electrons in the device, however. The lowest effective electron temperature that we were able to achieve in semiconductor quantum dots was  $\sim 45$  mK. Below we give a brief enumeration of the issues involved in doing these sensitive measurements.

### 1.3.1 filtering

A significant source of heating is the noise coming from the measurement electronics. The filters, used to attenuate the noise that arrives at the sample, have to be effective over a very large band width. They consist of a distributed RC network, usually a thin resistive wire going through a conducting medium such as copper powder or silver epoxy. The filters are installed at low temperatures to minimize the thermal noise of the resistors contained in them. The filters are integrated with the sample holder in such a way that all sample wires are carefully shielded once they are filtered (see Fig. ??).

### 1.3.2 interference

Another important source of heating is the interference picked up by the wiring that connects the measurement electronics to the device. Many different sources of interference can be distinguished. Loops in the electronic circuit need to be avoided to minimize magnetic pick up. All wires have to be carefully shielded to prevent them from being effective antennas for the radio and telecommunications signals filling the ether (0.1 MHz - 10 GHz). It is important that the circuit is grounded (connected to the shield) in only one place and that all shields have low impedance contact with this reference point.

A very significant source of interference in our high impedance samples are the vibrations of the sample wires. The vibrations tend to inject a current into the wires:  $I = \frac{d}{dt}Q = \frac{d}{dt}C\Phi = C\frac{d\Phi}{dt} + \Phi\frac{dC}{dt}$ , where  $\Phi$  is a potential difference that includes the difference in workfunctions of the wire metal and the metal of the ground (usually stainless steel). Due to the vibrations, the capacitance  $C$  of the wires to ground becomes timedependent. If the current doesn't find a low impedance path to ground, it will generate a considerable, unwanted voltage drop over the sample.

### 1.3.3 sample stability

To allow enough time to measure a reasonably complete set of data, the sample has to be sufficiently stable. Impurities or surface states that switch from one state to another are usually held responsible for switching in samples, as they change the details of the potential landscape in the sample. Some experiments can not be done if these switches happen more than once every ten minutes.

It is not quite understood which mechanisms cause some samples to be much more stable than others. The fabrication process is an important factor although two samples fabricated using identical conditions can have very different stability. It seems that as the electronic environment of the sample becomes more quiet the stability improves. Therefore a quiet set-up with low noise and little interference pays double. It not only allows one to measure faster because a larger bandwidth can be used, at the same time it also allows more time to measure between switches.

A separate issue is the lifespan of the samples. Since the samples are very small, a voltage transient picked up by the wires going to the sample may lead to large electric fields within the sample, which may fatally damage it. The sensitivity of the sample to electric discharges or other interference combined with the effort it takes to fabricate them has made experimentalists very cautious

when mounting a sample, previous to a cooldown. It has driven some people to take off their shoes when mounting samples. It is not clear whether this is out of superstitious beliefs or to prevent electrical discharges.

### 1.3.4 measurement electronics

The most crucial parts of the measurement electronics (the bias DACs for the gates, the low noise voltage source, and the current to voltage amplifier) are designed by Raymond Schouten and homebuilt. They are either battery powered or decoupled from the mains by separate transformers to reduce crosstalk of transients on the main power line to the electronics. They are galvanically decoupled from the conventional data acquisition electronics (oscilloscope, lock-in amplifier, multimeters, computer) through optical (fiber) links.

Special attention was given to the low noise current to voltage amplifier, to achieve a low equivalent input current noise ( $3\text{-}5 \text{ fA/Hz}^{\frac{1}{2}}$ ) and to overcome the stability problems of the amplifier associated with the large capacitance of the sample wires to ground.

### 1.3.5 high frequency coax

In order to do the high frequency experiments described in chapters 6 and 7 of this thesis, the dilution refrigerator was fitted with a coaxial cable (diameter .085 inch; all connectors used were 2.4 mm connectors from Hewlett Packard, which are specified up to 50 GHz). From a vacuum sealed connector at room temperature to the 1K-pot, a .085" semi rigid Be-Cu (inner and outer conductor) coaxial cable was used. Its outer conductor is thermally anchored at 4K. To cool the inner conductor also, a microwave attenuator is fitted at 1K.

From the 1K-pot to the mixing chamber, a .085" semi rigid stainless steel (inner and outer conductor) coaxial cable is used. Another microwave attenuator is fitted at the mixing chamber. Typically very little microwave power (pW - nW) is needed at the sample. Depending on the power available at the microwave source and the frequency range that is used in the experiment the value for the attenuation at the 1K-pot (3-10 dB) and at the mixing chamber (10-30 dB) are chosen. A larger attenuator will reduce the noise that is coupled into the sample through the coax. If the attenuation is too large, however, the mixing chamber will be warmed up due to the dissipated power in the attenuator.

From the mixing chamber to the sample, various types of low attenuation semirigid or flexible coaxial cable can be used because the heat conductivity through the coax is not a crucial issue anymore. Finally the inner conductor of

the coaxial cable is capacitatively coupled (1-100 pF) to one of the gates of the sample.

## 1.4 This thesis

The outline of this thesis is as follows. Chapters 2 to 4 are devoted to single *vertical* quantum dots. In chapter 2 the groundstates of a vertical dot are probed as a function of magnetic field. We compare the results to various different models, describing the 'atomic'-orbitals in the quantum dot. In chapter 3 we have looked at the excited states as well as the ground states and compare them with numerical calculations. In chapter 4 we investigate the vertical quantum dot in the quantum Hall regime. At these high magnetic fields interactions are very important, leading to the formation of a maximum density droplet.

The remaining chapters 5 to 9 are concerned with both single and double *lateral* quantum dots. We look at their spectroscopy in chapter 5, their interaction with time-varying fields in chapter 6 and 7, the 'molecular'-states in a double quantum dot in chapter 7, the interaction of the electrons with their environment in chapter 8, and a tuneable Kondo effect in a quantum dot in chapter 9.

## References

- [1] Proceedings of the NATO Advanced Study Institute on Mesoscopic Electron Transport, edited by L.L. Sohn, L.P. Kouwenhoven, and G. Schön (Kluwer Series E345, 1997). See also <http://vortex.tn.tudelft.nl/~leok/papers/>.
- [2] See for reviews in popular magazines: M. Reed, *Scientific American* **268**, 118 (1993); M.A. Kastner, *Physics Today* **46**, 24 (1993); R.C. Ashoori, *Nature* **379**, 413 (1996); C.J.P.M. Harmans, *Physics World* **5**, 50 (March 1992); L.P. Kouwenhoven and C.M. Marcus, *Physics World* **11**, (June 1998).
- [3] The first part of this chapter was partly taken from a review on quantum dots: L.P. Kouwenhoven, C.M. Marcus, P.L. McEuen, S. Tarucha, R.M. Westervelt and N.S. Wingreen, *Electron transport in quantum dots*, in *Mesoscopic Electron Transport*, edited by L.L. Sohn, G. Schön and L.P. Kouwenhoven, June 1996 (Kluwer, Series E 345, 1997). see also: <http://vortex.tn.tudelft.nl/~leok/papers/>. Other reviews may be found in: [4, 5, 6]
- [4] *Single Charge Tunneling*, edited by H. Grabert and M.H. Devoret (Plenum Press, 1991).

- 
- [5] D.V. Averin and K.K. Likharev, *J. Low Temp. Phys.* **62**, 345 (1986); and in: *Mesoscopic Phenomena in Solids*, edited by B.L. Altshuler, P.A. Lee, and R.A. Webb (Elsevier, 1991).
- [6] U. Meirav and E.B. Foxman, *Semicond. Sci. Technol.* **10**, 255 (1995).
- [7] H. Mizuto and T. Tanoue, *The Physics and Applications of Resonant Tunneling Diodes*, (Cambridge, 1996).



## Chapter 2

# Electron ground states in a few-electron quantum dot

T.H. Oosterkamp, W.G. van der Wiel, L.P. Kouwenhoven,  
D.G. Austing, T. Honda and S. Tarucha.

### Abstract:

We review the electronic ground states in few-electron quantum dots studied by measuring Coulomb oscillations in the linear transport regime. The number of electrons in our vertical quantum dots are changed one-by-one from zero up to about a hundred by means of the gate voltage. We identify the quantum numbers of the states by measuring the magnetic field dependence. We find that transitions in the ground states originate from crossings between single-particle states and Hund's rule. Most features can be explained with an extended constant interaction (CI) model. This model describes the electron-electron interactions by a charging energy plus an exchange energy which are both independent of magnetic field.

## 2.1 Introduction

Semiconductor quantum dots can be regarded as artificial atoms, since their electronic properties resemble the ionization energy and discrete excitation spectrum of atoms [1]. Quantum dots can be fabricated between source and drain contacts so that the atom-like properties can be probed in current-voltage (I-V) measurements. Additionally, with a gate electrode nearby, one can vary the exact number of electrons,  $N$ , on the quantum dot by changing the gate voltage,  $V_g$ . When an electron is added, the total charge on the dot changes by the elementary charge,  $e$ . The associated energy change, known as the addition energy, is a combination of the single-electron charging energy and the change in single-particle energy. Charging effects and discrete single-particle states have been studied in a variety of quantum dot systems, defined not only in semiconductors but also in metal grains and molecules [2].

Quantum dot devices usually contain some disorder due to impurities or because the shape is irregular [2]. Clean quantum dots, in the form of regular disks, have only recently been fabricated in a semiconductor heterostructure [3]. The circular symmetry of two dimensional (2D) disks gives rise to a 2D shell structure in the addition energies, analogous to the 3D shell structure in atomic ionization energies [4]. The 3D spherically symmetric potential around atoms yields the shells 1s, 2s, 2p, 3s, 3p,.... The ionization energy has a large maximum for atomic numbers 2, 10, 18,... corresponding to complete filling of a shell. Up to atomic number 23 these shells are filled sequentially with electrons (i.e. mixing between shells starts at atomic number 24). Within a shell, Hund's rule determines whether a spin-down or a spin-up electron is added [4].

Our vertical quantum dots have the shape of a disk with a diameter roughly ten times its thickness [3]. We find that their lateral confinement potential has good cylindrical symmetry with a rather soft boundary profile, which can be approximated by a harmonic potential. The symmetry of such a 2D harmonic potential leads to complete filling of 2D shells by 2, 6, 12, .... electrons. This sequence of electron numbers are the 'magic numbers' for a 2D harmonic dot. In this chapter we review the atomic-like properties observed in single-electron transport. We find unusually large addition energies when the electron number coincides with a magic number. Furthermore, we can identify the quantum numbers of the single-particle states by studying their magnetic field dependence. At sufficiently small magnetic fields ( $B < 0.4$  T) we see that spin filling obeys Hund's rule. At higher magnetic fields we observe that spin-degenerate states are filled by spin-up electrons alternating with spin-down electrons (i.e. an even-odd filling of the single-particle states).



The measured addition energies can be understood qualitatively in terms of an extended constant interaction (CI) model. In the CI model the direct Coulomb energy,  $E_c$ , between any two electrons on the dot is assumed to be independent of  $B$ . The energy  $E_c = e^2/C$  can be thought of as the charging energy of a single-electron on a capacitor  $C$ . To account for effects like Hund's rule we extend the CI model with a constant exchange energy  $E_{ex}$ . This extended CI model qualitatively explains the evolution of the ground state energies with  $B$ .

## 2.2 Device parameters and experimental set up

Our vertical quantum dot is a miniaturized resonant tunneling diode [5]. The pillar in Fig. 2.1a is etched from a semiconductor double-barrier heterostructure (DBH) and a metal gate electrode is deposited around it. Electrons are confined on the dot in all three dimensions. The surface potential together with the gate potential confines the electrons in the lateral  $x$ - and  $y$ -directions while the DBH provides the confinement in the growth  $z$ -direction.

The DBH consists of an undoped 12.0-nm  $\text{In}_{0.05}\text{Ga}_{0.95}\text{As}$  well and undoped  $\text{Al}_{0.22}\text{Ga}_{0.78}\text{As}$  barriers of thickness 9.0 and 7.5 nm (the thinner one is closest to the substrate). The source and drain contacts are made from Si doped n-GaAs which are separated by 3.0 nm undoped GaAs spacer layers from the barriers. The concentration of the Si dopants increases stepwise, on both sides starting with  $0.75 \cdot 10^{17} \text{ cm}^{-2}$  at 3 nm away from the barriers and increasing to  $2.0 \cdot 10^{18} \text{ cm}^{-2}$  at 400 nm from the barriers. An electron moving through the conduction band experiences a varying electrostatic potential landscape due to the changing band gap in the growth direction. Fig. 2.1b shows the calculated self-consistent energy profile in the growth direction for the large unpatterned DBH [5, 6].

A key ingredient of this material system is the inclusion of 5% indium in the  $\text{In}_{0.05}\text{Ga}_{0.95}\text{As}$  well. This lowers the conduction band bottom in the well to 32 meV below the Fermi level of the n-GaAs contacts. From the confinement potential in the  $z$ -direction and the effective mass  $m^*$  in  $\text{In}_{0.05}\text{Ga}_{0.95}\text{As}$  it follows that the lowest quantum state in the well is at an energy  $E_z = 26$  meV above the conduction band bottom. This is still 6.1 meV below the Fermi level of the contacts. To reach equilibrium the well is filled with electrons until the Fermi level of the dot is as close as possible to the Fermi levels in the contacts. Our vertical quantum dot system thus contains electrons without applying external voltages. This is important since it allows to study the linear transport regime; i.e. the current in response to a very small source-drain voltage,  $V_{sd}$ .

Previously, GaAs without indium was used as the well material [7, 8, 9]. The

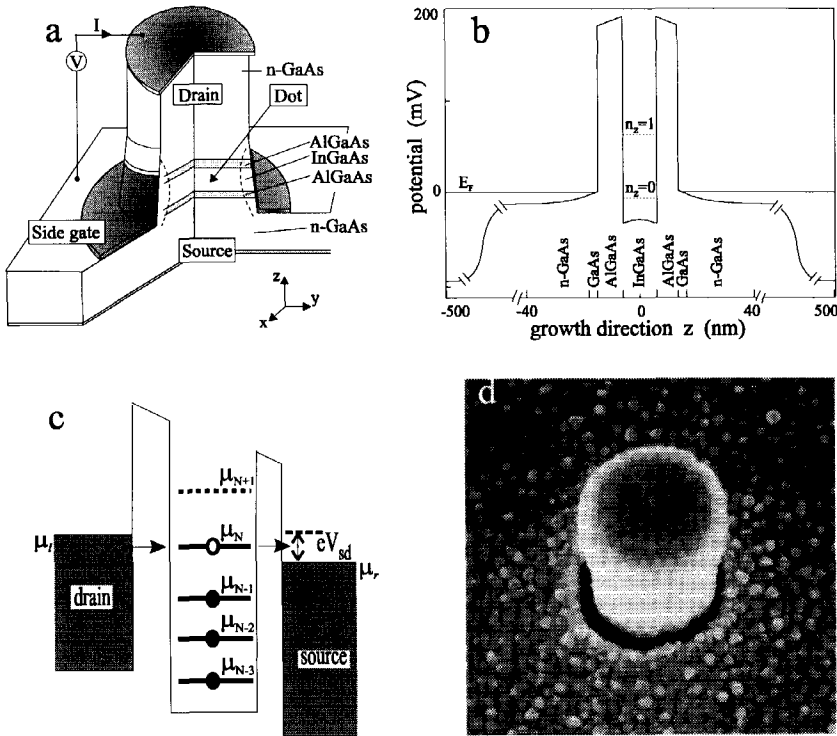


Figure 2.1: a) Schematic diagram of the device. The dot is located between the two heterostructure barriers. b) Self-consistent calculation [6] of the energy diagram of the unpatterned double barrier heterostructure from which the device is fabricated. c) Schematic energy diagram of the electron states in the dot. Shaded areas represent the states in the leads which are continuously filled up to the Fermi levels. A voltage,  $V_{sd}$ , applied between the source and the drain shifts one Fermi level relative to the other. Current may flow when the electro-chemical potential of the dot for a certain number of electrons (solid lines) lies between the Fermi levels of the leads. d) SEM photo of a circular quantum dot. The diameter of the pillar is  $D = 0.5 \mu\text{m}$ .

lowest state in the well is then above the Fermi level of the contacts. In this case, it is necessary to apply a large  $V_{sd}$  to force electrons into the well and to obtain a current flow. Subsequently, all experiments then have to be performed far out of equilibrium, which limits the energy resolution. From these materials two-terminal [7, 8] as well as three-terminal devices [9] have been fabricated. These early three-terminal devices could only be studied in the non-linear regime. Other techniques, in which the barriers are doped with Si, have been successful to accumulate some electrons in the well [10, 11]. This has the disadvantage that it introduces strong potential fluctuations in the dot. By optimizing the doping profile and using capacitance spectroscopy (which allows one barrier to be very thick), Ashoori et al. [12] succeeded in measuring the linear response of few-electron quantum dots. However, these capacitance-dots did not show signatures of circular symmetry. Our new dots allow, for the first time, to study both the linear and the non-linear response.

To put the gate around the pillar we first define a metal circle with geometrical diameter  $D$  which will serve later as the top contact. The metal circle is then used as a mask for a dry etch followed by a wet etch to a point just below the region of the DBH. This etch combination gives the pillar a somewhat smaller diameter than the top such that evaporation from above deposits the metal gate on the substrate and against the lower part of the pillar [13]. We find that when the diameter is around  $D \sim 0.5 \mu\text{m}$  we can vary the number of electrons on the dot,  $N$ , one-by-one from 0 to more than 80, by increasing the gate voltage,  $V_g$ .

The electron density in the well follows from self-consistent calculations and is equal to  $n_e = 1.67 \cdot 10^{15} \text{ m}^{-2}$ , which agrees with  $n_e = 1.7 \cdot 10^{15} \text{ m}^{-2}$  deduced from Shubnikov-de Haas oscillations measured on large area ( $D = 50 \mu\text{m}$ ) devices. From density times area we estimate to have about 10 electrons in the dot when the effective diameter  $d_{eff} = 100 \text{ nm}$ .

The geometry of our samples leads to strong screening of the Coulomb interactions inside the dot by the metallic regions in the source and drain which are only 10 nm away. This is illustrated when we compare the self-capacitance with the total capacitance of the dot. The self-capacitance of a disk with diameter  $d_{eff} = 100 \text{ nm}$  is given by  $C_{self} = 4\epsilon_r\epsilon_0d_{eff} = 50 \text{ aF}$ . A measure of the unscreened Coulomb interactions is the charging energy  $e^2/C_{self} = 4 \text{ meV}$ . The real capacitance is much better approximated by two parallel capacitors between dot and source and drain leads,  $C = C_s + C_d = 2\frac{\epsilon_r\epsilon_0\pi d_{eff}^2}{4d} \sim 200 \text{ aF}$ . Here  $d \sim 10 \text{ nm}$  is the distance between dot and leads. So, a measure of the screened Coulomb interactions follows from  $e^2/C = 1 \text{ meV}$ ; a value four times smaller than in the unscreened case. Electrons in the dot will thus have a short-range interaction. The strength of this interaction is further weakened by the finite thickness of the

disk.

An important parameter for our device is the ratio of the charging energy to the confinement energy. To estimate the confinement energy we assume a harmonic potential with an oscillator frequency  $\omega_0$  and note that for  $N \sim 10$  electrons the third shell is partially filled. From equating the energy at the classical turning point to the energy of the third shell ( $\frac{1}{2}m^*\omega_0^2\frac{d_{eff}^2}{2} = 3\hbar\omega_0$ ), we get  $\hbar\omega_0 = 3$  meV. This implies that the separation of the single-particle states is of order or even larger than the charging energy. This puts vertical dots in a very different regime compared to lateral quantum dots where the separation between single-particle states is typically 5 to 10 times smaller than the charging energy [2].

The well can in good approximation be regarded as a 2D system. The second quantum state due to confinement in the growth direction is 63 meV above the Fermi level. This energy is much larger than the lateral confinement energy. As we already mentioned, the finite thickness of the well has important consequences for the electron-electron interactions since the thickness of the well (12 nm) is comparable to the screening length due to the near vicinity of the leads (10 nm).

The devices are mounted in a dilution refrigerator for measurements at 50 mK. Due to external noise and interference, the effective electron temperature is typically 100-200 mK. We measure the current,  $I$ , flowing vertically through the dot in response to a dc voltage,  $V_{sd}$ , applied between the source and drain contacts. The gate voltage  $V_g$  can typically be varied from -2.5 to +0.7 V. Beyond these values leakage occurs through the Schottky barrier between the gate and source. We can use a magnetic field  $B$  up to 16 T directed parallel to the current.

## 2.3 Addition energies and shell filling

Figure 2.2a shows the current as a function of  $V_g$ . Clear Coulomb oscillations are observed with each peak corresponding to a change of exactly one electron on the dot. As we show below, the first peak corresponds to the transition from 0 to 1 electrons on the dot. This means that we know the absolute number of electrons on the dot; i.e.  $N = 1$  between the 1<sup>st</sup> and 2<sup>nd</sup> peaks;  $N = 2$  between the 2<sup>nd</sup> and 3<sup>rd</sup> peaks, etc. For  $N < \sim 20$ , the spacings between peaks fluctuate. This increasing 'irregularity' for smaller  $N$  has previously been reported for dots containing a few electrons [7, 8, 9, 10, 11, 12]. In this study, however, we find that the 'irregularity' in peak spacings is in fact systematic with respect to  $N$ .

In Fig. 2.2b the measured size of the Coulomb gap (i.e. the source-drain voltage at which current starts to flow) is plotted as a function of gate voltage.

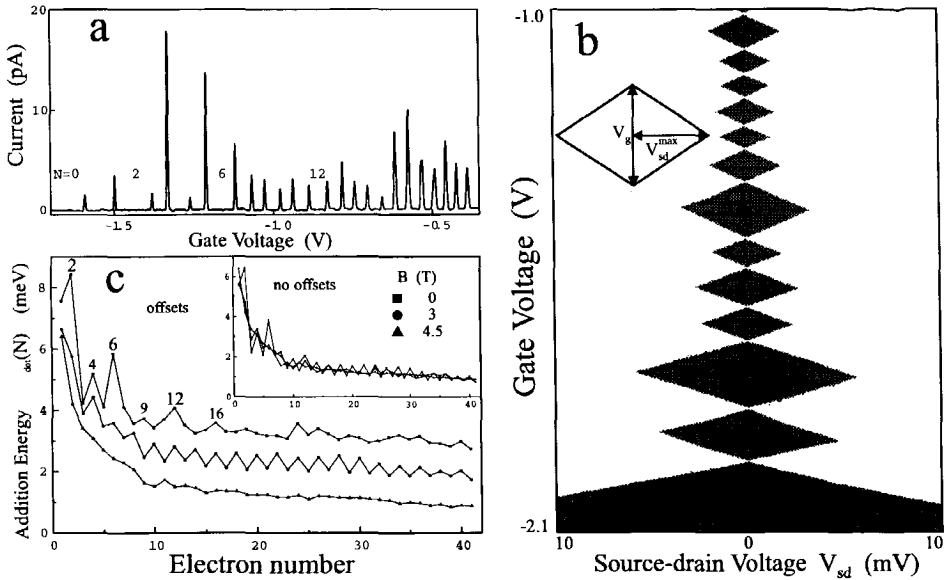


Figure 2.2: a) Coulomb oscillations in the current vs. gate voltage at  $B = 0$  T observed for a  $D = 0.5 \mu\text{m}$  dot.  $V_{sd} = 150 \mu\text{V}$ . b) Measured size of the Coulomb gap versus gate voltage. In the dark diamond shaped areas the device is in Coulomb blockade. In the light regions current flows. The sizes of the diamonds directly correspond to the peak spacings in a). c) Addition energy  $\Delta\mu(N)$  vs. electron number at different magnetic fields for a  $D = 0.5 \mu\text{m}$  dot. The curves for  $B = 0$  and 3 T have been given offsets of 2 and 1 meV, respectively for clarity. The inset shows the same curves without offsets.

The dark regions indicate zero current due to Coulomb blockade, while in the light regions the Coulomb gap is overcome and current is flowing through the dot. The vertical  $V_{sd} = 0$  axis corresponds directly to the data in Fig. 2.2a. Note, for instance, that the peak spacings along the  $V_{sd} = 0$  axis are the same as the peak spacings for the corresponding  $N$  in Fig. 2.2a. The width of the zero-current region, labeled as  $N = 0$ , keeps increasing when we make  $V_g$  more negative. This implies that here the dot is indeed empty which allows us to assign absolute electron numbers to the blocked regions.

As we discuss in section 2.4, the peak spacing is a measure for the amount of energy necessary to add an electron to the dot. Figure 2.2c shows the addition energy as a function of  $N$  for three different magnetic fields. As  $N$  is decreased,

the addition energy generally becomes larger due to the increase of the Coulomb interaction as the effective dot size is reduced. We find that the addition energy at  $B = 0$  T is unusually large for  $N = 2, 6$  and  $12$ . As we discuss below, these are the expected magic numbers for a 2D harmonic dot with circular symmetry.

In about twenty devices with  $D$  between  $0.4$  and  $0.54 \mu\text{m}$  we find that the addition energy is unusually large for  $N = 2$  and  $6$ . A large addition energy for  $N = 12$  is observed in about ten devices. We also observe relatively large addition energies for  $N = 4, 9$  and sometimes also  $16$ . We note that traces as in Fig. 2.2a reproduce in detail (including peak spacings and heights, but not the precise gate voltages) after we cycle the device to room temperature. In the remaining part of this paper we focus on one particular  $D = 0.5 \mu\text{m}$  device. All the main features, however, have been reproduced in several other devices.

The observation of the magic numbers at  $B = 0$  implies that the 2D lateral potential is parabolic within the resolution of our experiments. Note that for any 2D potential with circular symmetry there remains a twofold orbital degeneracy associated with positive and negative angular momentum states (except for the lowest energy state which has zero angular momentum). This makes the magic numbers  $2$  and  $6$  very robust. The assumption of a parabolic potential should be valid when  $N$  is small [3, 7, 8]. For larger  $N$ , the potential will be flattened in the center due to screening effects. This could be the reason why we do not observe the third shell in all of the devices.

## 2.4 Constant Interaction Model

In this section we introduce the constant interaction CI model that describes the electronic states of the dot. The CI model is based on two important assumptions. First, the Coulomb interactions of an electron on the dot with its environment and with other electrons on the dot are parametrized by a constant capacitance  $C$ . Second, the discrete energy spectrum of a single particle on the dot, which we discuss in the next section, is not affected by the interactions. The CI model approximates the total energy  $U(N)$  of an  $N$  electron dot by

$$U(N) = \frac{[e(N - N_0) - C_g V_g]^2}{2C} + \sum_N E_{n,l}(B) \quad (2.1)$$

where  $N_0$  is the number of electrons on the dot at zero gate voltage. The term  $C_g V_g$  is a continuous variable and represents the charge that is induced on the dot by the gate voltage  $V_g$  through the capacitance  $C_g$ . The total capacitance between the dot and the source, drain and gate is  $C = C_s + C_d + C_g$ . The last term is a sum over the occupied states  $E_{n,l}(B)$  which are the solutions to the

single-particle Schrödinger equation described in section 2.5. Note that only the single-particle states depend on magnetic field.

The electro-chemical potential of the dot is defined as  $\mu_{dot}(N) \equiv U(N) - U(N-1)$ . Electrons can flow from left to right when  $\mu_{dot}$  is between the electro-chemical potentials,  $\mu_{left}$  and  $\mu_{right}$ , of the leads:  $\mu_{left} > \mu_{dot}(N) > \mu_{right}$ . From eqn. 2.1 we get the electro-chemical potential of the dot

$$\mu_{dot}(N) = (N - N_0 - \frac{1}{2})E_c - e\frac{C_g}{C}V_g + E_N \quad (2.2)$$

The addition energy is given by

$$\Delta\mu(N) \equiv \mu_{dot}(N+1) - \mu_{dot}(N) = E_c + E_{N+1} - E_N \quad (2.3)$$

with  $E_N$  the topmost filled single-particle state for an  $N$  electron dot.

The electro-chemical potential is changed linearly by the gate voltage with a proportionality factor  $\alpha = e\frac{C_g}{C}$  (see Eqn. 2.2). This  $\alpha$  factor also relates the peak spacing to the addition energy. We define the spacing between the  $N^{th}$  Coulomb peak at  $V_g^N$  and the next peak at  $V_g^{N+1}$  as  $\Delta V_g(N) = V_g^{N+1} - V_g^N$ . The addition energy follows from  $\Delta\mu(N) = \alpha\Delta V_g(N)$ .

The inset to Fig. 2.2b illustrates how to determine the  $\alpha$  factor from the slopes of the sides of the Coulomb diamonds:  $\alpha = \left| e\frac{V_g^{max}}{\Delta V_g} \right|$ . Since the gate voltage changes the dot area, the  $\alpha$  factor changes with  $N$ . We therefore determine  $\alpha$  for each  $N$ . We find that, in the  $D = 0.5 \mu\text{m}$  dot,  $\alpha$  varies from 57 to 42 meV/V for  $N = 1$  to  $N = 6$ , and then gradually decreases to 33 meV/V as  $N$  approaches 20. On close inspection we can see that the sides of the diamonds for small  $N$  are a little curved indicating that  $\alpha$  changes somewhat even inside a diamond. These notions on addition energy and peak spacings are valid for any kind of confining potential. In the next section, we discuss the single-particle states in a specific potential.

## 2.5 Single particle states of a 2D harmonic oscillator

For the simplest explanation of the 'magic numbers' we ignore, for the moment, Coulomb interactions between the electrons on the dot. The familiar spectrum of a one-dimensional harmonic oscillator  $E_n = (n + \frac{1}{2})\hbar\omega$  becomes  $E_{n,l} = (2n + |l| + 1)\hbar\omega_0$  in two dimensions. Here  $n$  ( $= 0, 1, 2, \dots$ ) is the radial quantum number,  $l$  ( $= 0, \pm 1, \pm 2, \dots$ ) is the angular momentum quantum number of the oscillator and  $\omega_0$  is the oscillator frequency.

The electronic states are expected to be significantly modified by a magnetic field,  $B$ , applied perpendicular to the plane of the dot. The eigenenergies  $E_{n,l}$  as a function of  $B$  can be solved analytically for a 2D parabolic confining potential  $V(r) = \frac{1}{2}m^*\omega_0^2r^2$  [14]

$$E_{n,l}(B) = (2n + |l| + 1) \hbar \sqrt{\frac{1}{4}\omega_c^2 + \omega_0^2} - \frac{1}{2}l\hbar\omega_c \quad (2.4)$$

where  $\hbar\omega_0$  is the electrostatic confinement energy,  $\hbar\omega_c = \frac{\hbar eB}{m^*}$  is the cyclotron energy and  $m^* = 0.067m_e$  is the effective mass in GaAs ( $\hbar\omega_c = 1.7$  meV at 1 T). Since GaAs has a small  $g$ -factor ( $g = -0.44$  and  $g\mu_B B = 25\mu\text{eV}$  at 1 T) we can neglect the Zeeman energy. This makes each orbital state two-fold spin-degenerate.

In Fig. 2.3a we plot  $E_{n,l}$  vs.  $B$  for  $\hbar\omega_0 = 3$  meV. It shows that the orbital degeneracies at  $B = 0$  are lifted in the presence of a B-field. As  $B$  is initially increased from 0 T, a single-particle state with a positive or negative  $l$  shifts to lower or higher energy, respectively. At  $B = 0$  the lowest energy state has  $(n, l) = (0, 0)$  and is twofold spin degenerate. The next state has a double orbital degeneracy  $E_{0,1} = E_{0,-1}$ . We denote these degenerate states the second shell. Including spin degeneracy this shell can contain up to 4 electrons, so it will be filled when there are 6 electrons on the dot. In the third shell states with quantum numbers  $(1,0)$ ,  $(0,2)$  and  $(0,-2)$  are degenerate. With spin this shell may contain up to 6 electrons, leading to the magic number 12. Note that the degeneracy of the  $(1,0)$  state with the  $(0,2)$  and  $(0,-2)$  states is lifted if the potential has a non-parabolic component [16].

When we put 7 non-interacting electrons in the dot and increase  $B$ , the 7th electron will make several transitions into different states. We have indicated this in Fig. 2.3a with a dashed line. The transitions are from  $(0, 2)$  to  $(0, -1)$  at 1.3 T and then to  $(0, 3)$  at 2 T. Similar transitions are also seen for other  $N$ . After the last crossing the electrons occupy states forming the lowest orbital Landau Level which is characterized by the quantum numbers  $(0, l)$  with  $l \geq 0$ . Together with spin we can label the last crossing as filling factor 2; this in analogy to the quantum Hall effect in a 2D electron gas. In contrast to the bulk 2D case, the confinement lifts the degeneracy in this Landau level. The calculated separations between single-particle states at, for example,  $B = 3$  T, is still quite large (between 1 and 1.5 meV in Fig. 2.3a). If we would speak of magic numbers at  $B = 3$  T the sequence would simply be 2, 4, 6, 8, etc.

In the CI model a Coulomb charging energy is added to the non-interacting single-particle states of Eqn. 2.4 to take into account the interaction. The addition spectrum of a quantum dot then follows from the electro-chemical potential



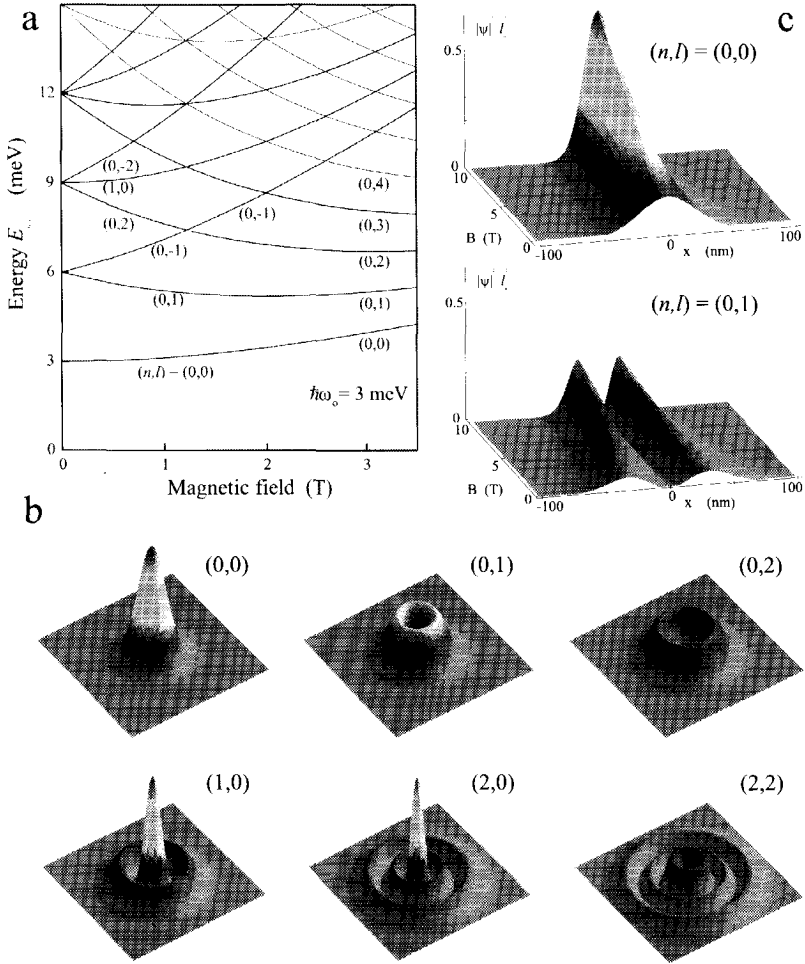


Figure 2.3: a) Calculated single-particle energy vs. magnetic field for a parabolic potential with  $\hbar\omega_0 = 3 \text{ meV}$ . Each state is twofold spin-degenerate. The dashed line indicates the transitions that the 7<sup>th</sup> and 8<sup>th</sup> electron on the dot make as the magnetic field is increased. b) Single particle wavefunctions for different quantum numbers  $(n,l)$  c) Magnetic field dependence of the single particle wavefunctions of quantum numbers  $(0,0)$  and  $(0,1)$ .

$\mu_{dot}(N)$  (Eqn. 2.2) where the topmost filled state  $E_N$  in Fig. 2.3a is added to the charging energy. The addition spectrum versus  $B$  is shown in Fig. 2.4b. Note that spin-degenerate states are now separated by  $E_c$ , so each line appears double. The magic numbers 2, 6, 12, 20, etc. are still visible at  $B = 0$  as enhanced energy separations which are equal to  $E_c + \hbar\omega_0$ . An even-odd parity effect is seen at  $B = 5$  T where the energy separations for  $N = \text{even}$  are larger than those for  $N = \text{odd}$ .

For some applications it is helpful to know the wavefunctions belonging to the eigenenergies of Eqn. 2.4. They are given by

$$\psi_{n,l}(r, \phi) = \frac{1}{\sqrt{2\pi}} e^{il\phi} \frac{1}{l_B} \sqrt{\frac{n!}{(n+|l|)!}} e^{-r^2/4l_B^2} (r/\sqrt{2}l_B)^{|l|} L_n^{|l|}(r^2/2l_B^2) \quad (2.5)$$

where  $l_B = (\hbar/m^*\Omega)^{1/2}$  with  $\Omega = \sqrt{\frac{1}{4}\omega_c^2 + \omega_0^2}$  is the characteristic length and  $L_n^{|l|}$  are generalized Laguerre polynomials. The square of the wavefunction  $|\psi_{n,l}(r, \phi)|^2$  is plotted in Fig. 2.3b for different quantum numbers  $(n, l)$ . Note that two wavefunctions with quantum numbers  $(n, \pm l)$  only differ in the phase factor  $e^{\pm il\phi}$ . The number of nodes of the wavefunction going out from the center is given by the radial quantum number  $n$ . If the angular momentum quantum number is not zero there is an additional node at  $r = 0$ . The larger  $|l|$  the wider the node around  $r = 0$ . When a magnetic field is applied, the characteristic length  $l_B$  set by the oscillator frequency  $\Omega$  becomes smaller and the extent of the wavefunction shrinks as is shown in Fig. 2.3c for the square of the wavefunctions with quantum numbers  $(0,0)$  and  $(0,1)$ . This turns out to be an important effect that leads to deviations from the CI model when  $B$  is changed on a relatively large scale (e.g. 10 T). For example, two electrons in the  $(0,0)$  state are pushed closer together when  $B$  is increased which enhances their Coulomb interaction. In this case,  $E_c$  will not be completely independent of  $B$ .

## 2.6 Magnetic field dependence of ground states

Fig. 2.4a shows the measured B-field dependence of the positions of the current peaks. It is constructed from  $I-V_g$  curves for  $B$  increasing from 0 to 3.5 T in steps of 0.05 T. The evolution of the first 22 current peaks are plotted. The positions of the first three peaks depend monotonously on  $B$ , whereas the other peaks oscillate up and down a number of times. The number of 'wiggles' increases with  $N$ . Each  $N = \text{odd}$  peak has a neighbour for  $(N + 1) = \text{even}$  that wiggles in-phase. This pairing implies that the  $N^{\text{th}}$  and  $(N + 1)^{\text{th}}$  electrons occupy the same single-particle state with opposite spin. We see this pairing up to  $N = 40$ .

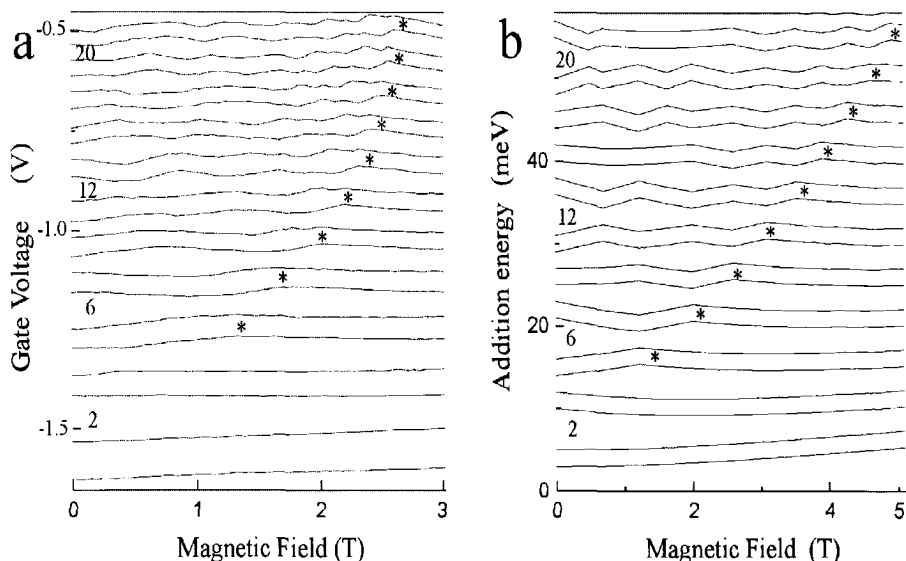


Figure 2.4: *Plot of the gate voltage positions of the current oscillations vs. magnetic field for a dot with  $D = 0.5 \mu\text{m}$ . b) Calculated electro-chemical potential  $\mu(N)$  using the constant interaction (CI) model (Eqn. 2.1), with  $E_c = 2 \text{ meV}$  and  $\hbar\omega_0 = 3 \text{ meV}$ .*

Around 3 T the peaks have stopped wiggling and now evolve smoothly with  $B$ . Close inspection shows that the peak spacing alternates between 'large' for even  $N$  and 'small' for odd  $N$ . This is particularly obvious when we convert peak spacing to addition energies. Then a clear even-odd parity is seen in the addition energy versus  $N$  at 3 T (see the middle trace of Fig. 2.2c). The amplitude of the even-odd oscillations is a good measure of the separation between the single-particle states at 3 T. We observe a slowly decreasing amplitude from  $\sim 1$  to  $\sim 0.5 \text{ meV}$  for  $N$  increasing to 40, suggesting that the confining energy decreases with increasing gate voltage. This trend is also seen in the  $B$  dependence of the last transition (i.e. filling factor 2 which is indicated by \*'s). We find that for larger  $N$  the transition into the lowest Landau level occurs at a  $B$ -value lower than calculated (note the different field scales of figures 2.4a and b). The evolution of the \*'s saturate at  $\sim 3 \text{ T}$  for  $N \sim 50$  which means that for these larger electron numbers increasing  $V_g$  increases the area and  $N$  such that the electron density stays constant. Note that at 4.5 T the addition energy versus  $N$  in Fig. 2.2c becomes smoother, suggesting that the dot becomes more and more

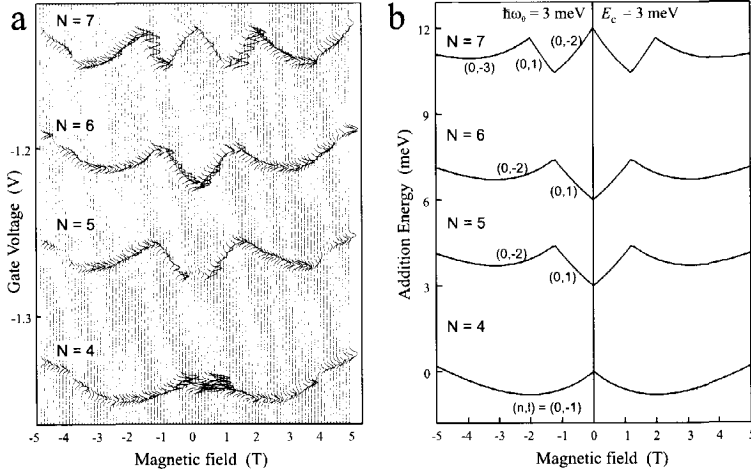


Figure 2.5: a) Evolution of the 4<sup>th</sup>, 5<sup>th</sup>, 6<sup>th</sup> and 7<sup>th</sup> current peaks with  $B$ -field from  $-5$  to  $5$  T observed for the  $D = 0.5 \mu\text{m}$  dot. The original data consist of current vs. gate voltage traces for different magnetic fields which are offset. b) Calculated electro-chemical potential  $\mu_{\text{dot}}(N)$  using the CI model, with  $E_c = 3 \text{ meV}$  and  $\hbar\omega_0 = 3 \text{ meV}$ .

spin polarized as  $B$  is increased.

A more detailed comparison can be made from Fig. 2.5a, which focuses on the range in  $B$  from  $-5$  to  $5$  T for  $N = 4$  to  $7$ . For comparison Fig. 2.5b shows the calculated addition spectrum. It is clear that the 5<sup>th</sup> and 6<sup>th</sup> peaks form a pair. At  $1.3$  T the evolution of the 6<sup>th</sup> peak has a maximum whereas the 7<sup>th</sup> peak has a minimum. This corresponds to the crossing of the energy curves of the  $(0, -1)$  and  $(0, 2)$  quantum states at  $1.3$  T in Fig. 2.3a. The effective dot diameter when there are 6 or 7 electrons on the dot is derived from the wavefunctions ( $d \sim 5l_B$  for  $(0, 2)$ , see Fig. 2.3b). From the estimated confinement potential  $\hbar\omega_0 = 3 \text{ meV}$  it follows that the diameter is about  $d_{\text{eff}} \sim 100 \text{ nm}$ .

A closer look at Fig. 5a shows that peaks 4 and 5 are not exact replicas. In particular around  $B = 0$ , peak 4 has a sharp cusp down while peak 5 has a cusp up in the range  $-0.4 < B < 0.4$  T. We discuss in the next section that

this deviation from the CI model results from the exchange interaction between electrons with parallel spins in the second shell.

## 2.7 Hund's rule and exchange energy

We now focus on the evolution of the peak positions near  $B = 0$  T and show that deviations from the CI model are related to Hund's rule. Figure 2.6a shows the B-field dependence of the 3<sup>rd</sup>, 4<sup>th</sup>, 5<sup>th</sup> and 6<sup>th</sup> current peaks for a B-field up to 2 T. The pairing of the 3<sup>rd</sup> and 4<sup>th</sup> peaks and the 5<sup>th</sup> and 6<sup>th</sup> peaks *above* 0.4 T is clearly seen. However, we find that *below* 0.4 T the 3<sup>rd</sup> and 5<sup>th</sup> peaks are paired, and the 4<sup>th</sup> and 6<sup>th</sup> peaks are paired. Note that this pairing is also seen in the peak heights. The evolution as a pair of the 3<sup>rd</sup> and 5<sup>th</sup> peaks for  $B < 0.4$  T is continued by the 3<sup>rd</sup> and 4<sup>th</sup> peaks for  $B > 0.4$  T. Similarly, the evolution as a pair of the 4<sup>th</sup> and 6<sup>th</sup> peaks for  $B < 0.4$  T is continued by the 5<sup>th</sup> and 6<sup>th</sup> peaks for  $B > 0.4$  T. From these observations, we conclude that the 4<sup>th</sup> electron undergoes an angular momentum transition from  $l = -1$  to  $l = 1$  at 0.4 T, whereas the 5<sup>th</sup> electron undergoes an angular momentum transition from  $l = 1$  to  $l = -1$ . These 'extra' transitions can be understood in terms of Hund's rule, which states that a degenerate shell of states will be filled by electrons with parallel spins [4].

To explain the above transitions we need to extend the CI model. If we leave out the contributions from the gate voltage one can write for the total energy  $U(N) = \frac{1}{2}N(N-1)E_c + \sum E_{n,l} - E_{exch}(\sigma)$ . The last term allows to take into account a reduction of the total energy due to the exchange interaction between electrons with parallel spins. For simplicity we assume that only electrons in quantum states with identical radial quantum number and opposite angular momentum ( $n, \pm l$ ) have an appreciable exchange interactions and ignore all other contributions. Let us first write out explicitly  $U(N)$  and  $\mu(N)$  for  $N$  from 1 to 6 assuming that spin is always minimized (i.e. total spin  $S = \frac{1}{2}$  or 0):

$$\begin{aligned} U(1) &= E_{0,0} & U(2) &= E_c + 2E_{0,0} \\ U(3) &= 3E_c + 2E_{0,0} + E_{0,1} & U(4) &= 6E_c + 2E_{0,0} + 2E_{0,1} \end{aligned}$$

$$U(5) = 10E_c + 2E_{0,0} + 2E_{0,1} + E_{0,-1} - E_{exch}$$

$$U(6) = 15E_c + 2E_{0,0} + 2E_{0,1} + 2E_{0,-1} - 2E_{exch}$$

and

$$\mu(1) = U(1) - 0 = E_{0,0} \quad \mu(2) = U(2) - U(1) = E_c + E_{0,0}$$

$$\mu(3) = U(3) - U(2) = 2E_c + E_{0,1} \quad \mu(4) = U(4) - U(3) = 3E_c + E_{0,1}$$

$$\mu(5) = U(5) - U(4) = 4E_c + E_{0,-1} - E_{exch}$$

$$\mu(6) = U(6) - U(5) = 5E_c + E_{0,-1} - E_{exch}$$

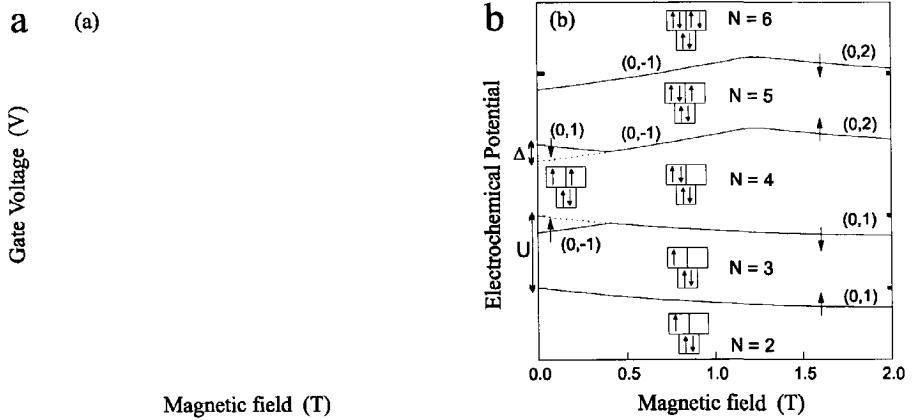


Figure 2.6: a) Evolution of the 3<sup>rd</sup>, 4<sup>th</sup>, 5<sup>th</sup> and 6<sup>th</sup> current peaks with B-field from 0 to 2 T. The original data consist of current vs. gate voltage traces for different magnetic fields which are offset. b) Calculated electrochemical potential vs. magnetic field for the model including a constant exchange energy as described in the text. Parameters are  $E_c = 3$  meV,  $\hbar\omega_0 = 3$  meV and  $E_{exch} = 0.7$  meV.

For  $N = 4$  we can also put the 3<sup>rd</sup> and 4<sup>th</sup> electron with parallel spins (i.e.  $S = 1$ ) in the separate single-particle states  $E_{0,1}$  and  $E_{0,-1}$ . In this case we get:  $U^*(4) = 6E_c + 2E(0,0) + E(0,1) + E(0,-1) - E_{exch}$ . The ground state for  $N = 4$  has  $S = 1$  if  $U^*(4) < U(4)$ , or  $E_{0,-1} - E_{0,1} = \hbar\omega_c < E_{exch}$ . A transition from  $S = 1$  to  $S = 0$  occurs for larger B-fields. The experimentally observed transition field  $B = 0.4$  T yields  $E_{exch} = 0.7$  meV.

Below  $B = 0.4$  T not only the electro-chemical potential of  $N = 4$  but also of  $N = 5$  is affected by this extra transition due to  $E_{exch}$ :

$$\mu^*(4) = U^*(4) - U(3) = 3E_c + E_{0,-1} - E_{exch}$$

$$\mu^*(5) = U(5) - U^*(4) = 4E_c + E_{0,1}$$

Note that  $\mu^*(4)$  follows the B-dependence of  $E_{0,-1}$  which implies that the 4<sup>th</sup> peak should pair with the 6<sup>th</sup> peak. Similarly, the 5<sup>th</sup> peak should pair with the 3<sup>rd</sup> peak for  $B < 0.4$  T.

We find a remarkable agreement between what we measure in Fig. 2.6a and the calculation in Fig. 2.6b if we assume  $E_c = 3$  meV and  $E_{exch} = 0.7$  meV. In

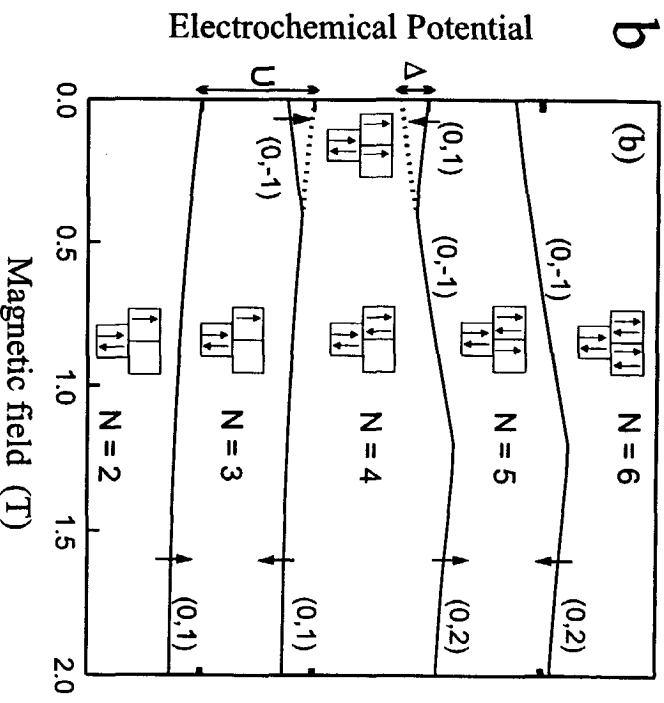
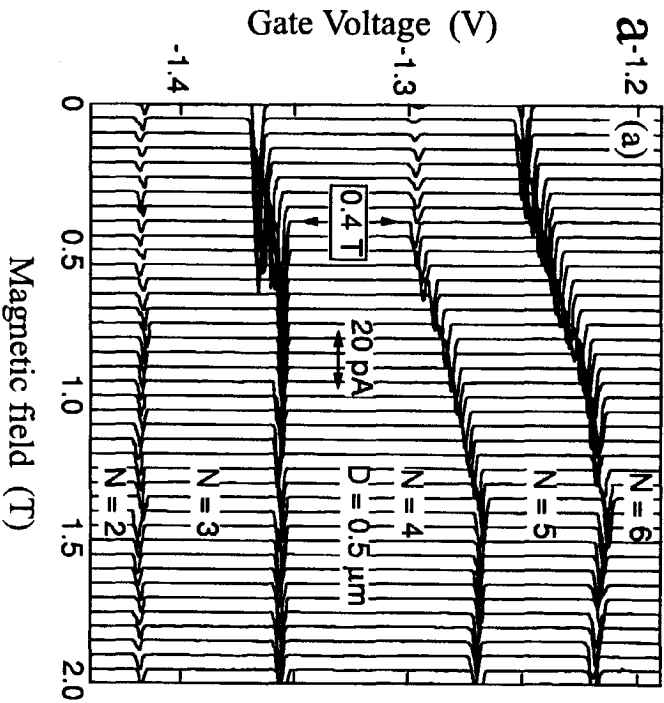


Figure 2.6

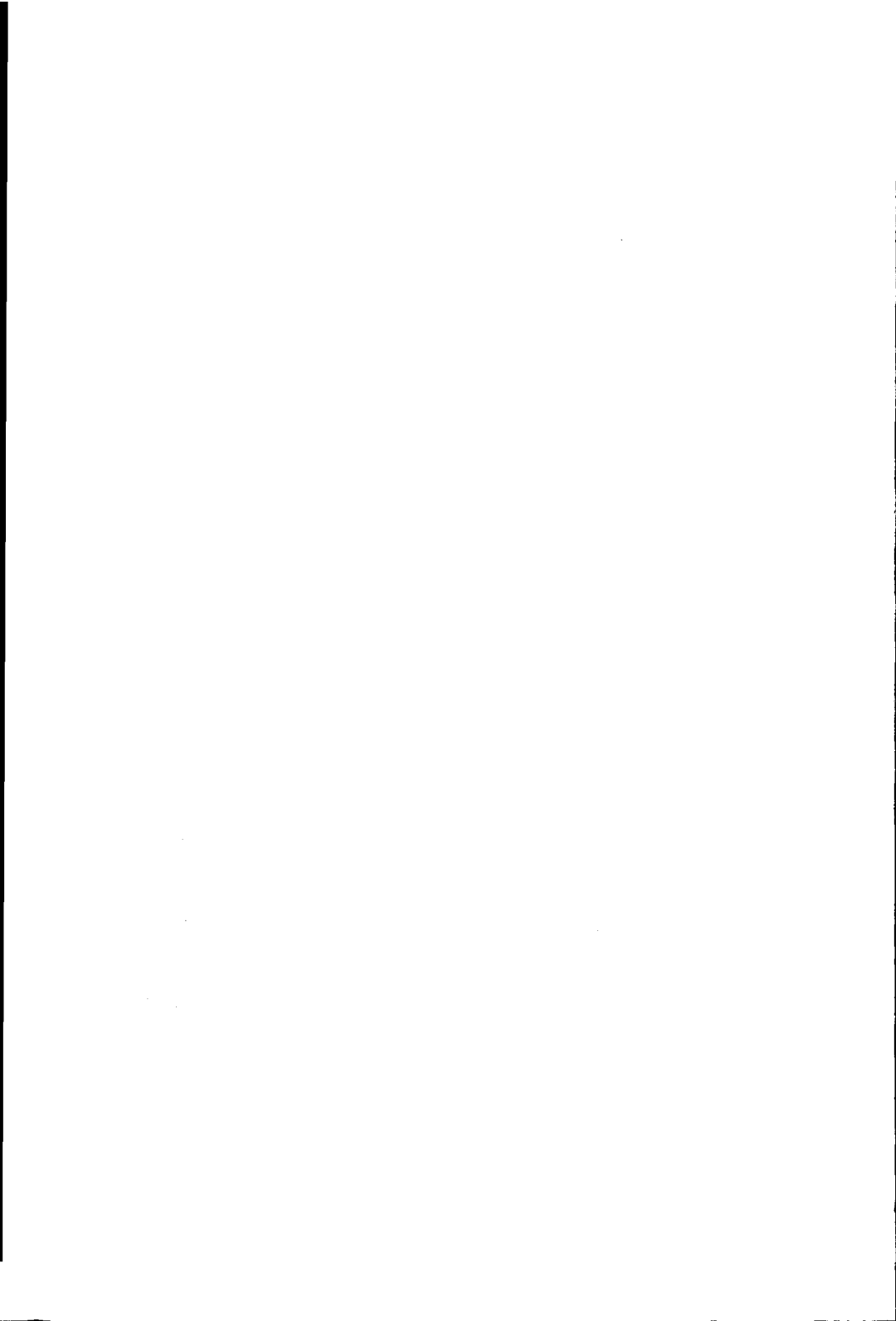




Fig. 2.6b we include quantum numbers ( $n, l$ ) to identify the angular momentum transitions, and pictorial diagrams to illustrate the spin configurations.

At  $B = 0$  the ground-state addition energies  $\Delta\mu(N) \equiv \mu(N + 1) - \mu(N)$  become:

$$\begin{aligned} \Delta\mu(1) &= E_c & \Delta\mu(2) &= E_c + E_{0,1} - E_{0,0} & \Delta\mu(3) &= E_c - E_{exch} \\ \Delta\mu(4) &= E_c + E_{exch} & \Delta\mu(5) &= E_c - E_{exch} \end{aligned}$$

While the peak spacing for  $N = 2$  is enhanced due to the separation in single-particle energies, the spacing for  $N = 4$  is expected to be larger than the spacings for  $N = 3$  and 5 by twice the exchange energy  $2E_{exch}$  ( $= 1.4$  meV). These enhancements are indeed observed in the addition curve for  $B = 0$  in Fig. 2.2b. Similar bookkeeping as above also explains the enhancements of  $N = 9$  and 16 which correspond to a spin-polarized half-filled third shell ( $S=3/2$ ) and fourth shell ( $S=2$ ), respectively. The above simple example shows that inside a shell the symmetry can be broken and degeneracies can be lifted due to interactions. This spin-polarized filling and symmetry-breaking is completely analogous to Hund's rule in atomic physics. Although our bookkeeping method is very simple it explains the data well. Self-consistent calculations of several different approaches have confirmed this model of constant charging and exchange energies [15, ?].

## 2.8 Singlet - triplet transition

The CI model assumes that the Coulomb interactions between electrons are independent of the magnetic field, so that changes in the observed ground state energies are fully described to changes in the single-particle *energies*. At larger  $B$  it is essential to include a varying Coulomb interaction [17]. Here, we discuss this non-constant interaction regime for dots with one to four electrons and  $B$  between 0 and 9 T. In particular, we describe the singlet-triplet (ST) transition induced by a magnetic field for a dot with two electrons.

For a two-electron dot, we only consider the two lowest single-electron states,  $E_{0,0}$  and  $E_{0,1}$ , which are relevant to the discussion here. For any value of  $B$ ,  $E_{0,0} < E_{0,1}$  and hence the two electrons both occupy the state  $E_{0,0}$  with opposite spin; i.e. a singlet,  $S = 0$  state. Including the Zeeman energy, we obtain:  $E_{0,0} = \hbar\sqrt{\frac{1}{4}\omega_c^2 + \omega_0^2} \pm \frac{1}{2}g^*\mu_B B$  and  $E_{0,1} = 2\hbar\sqrt{\frac{1}{4}\omega_c^2 + \omega_0^2} - \frac{1}{2}\hbar\omega_c \pm \frac{1}{2}g^*\mu_B B$  with  $g^*$  the effective Landé factor and  $\mu_B$  the Bohr magneton. We now expect a crossing between  $E_{0,0,\downarrow}$  and  $E_{0,1,\uparrow}$  beyond which the two electrons are spin-polarized; i.e. a triplet,  $S = 1$  state. For  $\hbar\omega_0 = 5.6$  meV and  $g^* = -0.44$  in GaAs, we obtain a ST transition driven by the Zeeman energy at  $B = 25$  T. Note that this estimate neglects electron-electron interactions. As we now discuss, the Coulomb

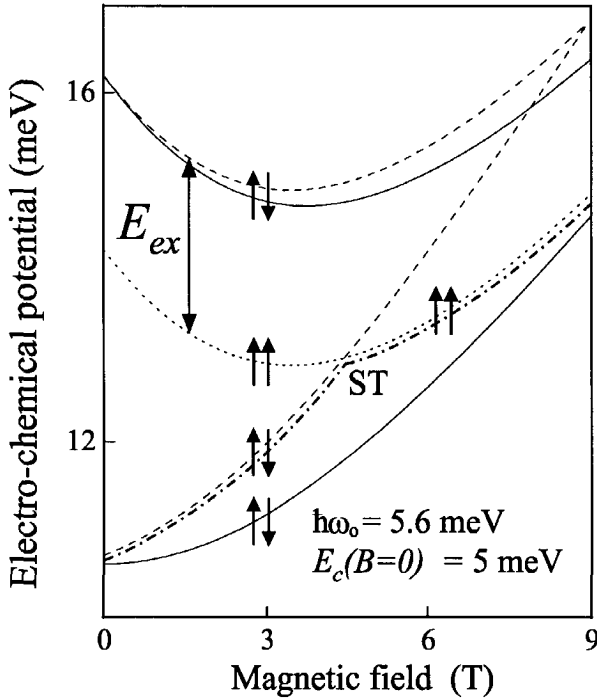


Figure 2.7: Electro-chemical potential  $\mu(2)$  of a two-electron dot as function of magnetic field ( $\hbar\omega_0 = 5.6$  meV,  $E_c(B=0) = 5$  meV). The lower solid curve represents the CI ground-state electro-chemical potential  $\mu^{\uparrow\downarrow}(2) = E_{0,0} + E_c$  (spins indicated by arrows), whereas the upper solid curve corresponds to the excited state,  $\mu^{\uparrow\downarrow,ES}(2) = E_{0,1} + E_c$ . The dashed lines schematically represent the situation in which a  $B$ -dependent Coulomb interaction is taken into account. Note that the dashed lines grow faster than the solid ones. The rise of the lower one is larger, due to the larger overlap of states when both electrons are in the ground-state. The upper dashed curve with subtraction of a constant exchange energy  $E_{ex}$  results in the dotted curve  $\mu^{\uparrow\uparrow}(2) = E_{0,1} + E_c(B) - E_{ex}$ .  $\mu^{\uparrow\downarrow}(2)$  and  $\mu^{\uparrow\uparrow}(2)$  cross at  $B \simeq 4.5$  T. The ground state before and after the singlet-triplet (ST) transition is indicated by a dashed-dotted line.

interactions between the two electrons drive the ST transition to much lower  $B$ .

The interdependence of Coulomb interactions and single-particle states becomes important when a magnetic field changes the size of the electron states. As was shown in section 2.5, the size of the DF-states shrinks in the radial direction as  $B$  is increased. When two electrons both occupy the  $E_{0,0}$  state, the average distance between them decreases with  $B$  and hence the Coulomb interaction increases. At some magnetic field it is energetically favorable if one of the two electrons makes a transition to a state with a larger radius (i.e. from  $l = 0$  to  $l = 1$ ), thereby increasing the average distance between the two electrons. This transition occurs when the gain in Coulomb energy exceeds the costs in single-particle energy. So, beside the Zeeman energy, the shrinking of wavefunctions favors a transition in angular momentum.

Numerical calculations by Wagner et al. [18] have predicted these ST transitions. In our discussion here, we generalize the CI model in order to keep track of the physics that gives rise to the ST transition. The electro-chemical potential of a dot containing  $N$  electrons was defined above as  $\mu(N) \equiv U(N) - U(N - 1)$  where  $U(N)$  is the total energy of the dot. For an  $N = 1$  dot,  $U^\uparrow(1) = E_{0,0}$  is the exact ground state energy (spins are indicated by arrows). In the CI model,  $U^\downarrow(2) = 2E_{0,0} + E_c$ , so that the ground-state electro-chemical potential is  $\mu^\downarrow(2) = E_{0,0} + E_c$ . Note that the Coulomb interactions are assumed to be described by a constant charging energy  $E_c$ . The first excited state is  $U^{\uparrow\downarrow,ES}(2) = E_{0,0} + E_{0,1} + E_c$  and  $\mu^{\uparrow\downarrow,ES}(2) = E_{0,1} + E_c$ . The solid lines in Fig. 2.7 show  $\mu^\downarrow(2)$  and  $\mu^{\uparrow\downarrow,ES}(2)$ , where we neglect the small contribution of the Zeeman energy.

The next level of approximation is to include the magnetic field dependence of the charging energy to account for the shrinking wavefunctions. The dashed curves in Fig. 2.7 rise somewhat faster than the solid curves, reflecting the  $B$ -dependence of the charging energy,  $E_c(B)$ . These dashed lines are schematic curves and do not result from calculations.

When both electrons occupy the  $E_{0,0}$  state their spins must be anti-parallel. However, if one electron occupies  $E_{0,0}$  and the other  $E_{0,1}$ , the two electrons can also take on parallel spins; i.e. the total spin  $S = 1$ . In this case, the Coulomb interaction is reduced by an exchange energy  $E_{ex}$  and the corresponding electro-chemical potential becomes  $\mu^\uparrow(2) = E_{0,1} + E_c(B) - E_{ex}$ ; see the dotted line in Fig. 2.7. (The exchange energy is due to a deformation of the distribution functions of Fig. 2.3 for electrons with parallel spin, which yields a reduction of the Coulomb repulsion.) Importantly,  $\mu^\downarrow(2)$  and  $\mu^\uparrow(2)$  cross at  $B \simeq 4.5$  T for the parameters chosen in Fig. 2.7. So, while for  $B < 4.5$  T the ground state energy corresponds to two electrons with anti-parallel spins in the lowest single-particle state, for  $B > 4.5$  T the ground state has contributions from two

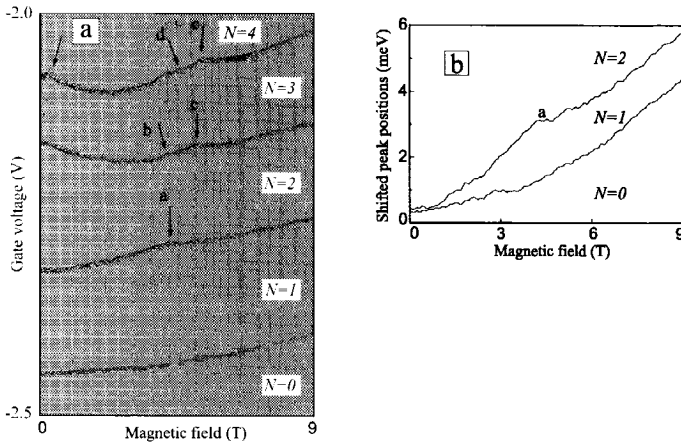


Figure 2.8: (a) Current measurement as function of gate voltage and magnetic field (0–9 T in steps of 25 mT) for  $N = 1$  to 4 and  $V_{sd} = 30 \mu\text{V}$ . The indicated transitions are discussed in the text. (b) Peak positions extracted from the data in (a) and shifted towards each other. Gate voltage is converted to electro-chemical potential.

single-particle states and has total spin  $S = 1$  (the two-electron ground state is indicated by a dashed-dotted line in Fig. 2.7). Thus, while the Zeeman-driven transition would occur at 25 T, the electron-electron interactions push the ST transition to a lower value depending on the confinement (4.5 T in our case) [19].

Capacitance [12] and tunneling [7] spectroscopy have provided evidence for ST transitions in the two-electron ground state energy. Here, we report the evolution of the ground-state as well as the first excited state versus  $B$ . Fig. 2.8a shows the linear response Coulomb blockade peaks for  $N = 0$  to 4. The four curves reflect how the ground state electrochemical potentials  $\mu(N)$  for  $N = 1$  to 4 evolve with  $B$ . We emphasize that, based on the DF-spectrum for non-interacting electrons, one does not expect transitions or kinks in the  $B$ -dependence of  $\mu(N)$  for  $N = 1$  to 4. The peak for  $N = 1$  indeed has a smooth  $B$ -dependence. For  $N = 2, 3$ , and 4, however, we observe kinks, which are indicated by arrows. These kinks must arise from interactions not included in the CI model. The left arrow in the  $N = 4$  trace is due to the destruction of a Hund's rule state, which has been discussed previously [17, 3]. To blow up the different kinks, we extracted the peak positions and converted their values from gate voltage to energy using the

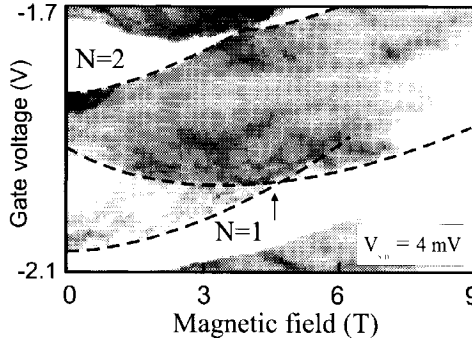


Figure 2.9: *Gray scale plot of  $I(V_g, B)$  for  $V_{sd} = 4$  mV. The stripe for the second electron entering the dot is shown. The ground state and first excited state are accentuated by dashed curves. The crossing corresponds to the ST transition.*

$\alpha$ -factors introduced in section 2.4. The plotted curves in Fig. 2.8b are shifted towards each other and represent the variation of the electro-chemical potential with  $B$ . The lowest curve for  $N = 1$  shows a smooth [20] increase in energy in accordance with the expected solid curve for  $E_{0,0}$  in Fig. 2.7. The next curve for  $N = 2$  rises faster with  $B$  than the  $N = 1$  curve, which reflects the magnetic field dependent interaction  $E_c(B)$  (see lower dashed curve in Fig. 2.7). At 4.5 T, indicated by "a", we observe a kink in the  $N = 2$  curve. This is the expected ST transition. Our choice of shifting the peak position curves for  $N = 1$  and 2 to zero at  $B = 0$  in Fig. 2.8b, allows a direct comparison, and shows a good agreement with the lower solid curve and the dashed-dotted curve in Fig. 2.7.

For larger source-drain voltage,  $V_{sd}$ , the current peaks become stripes with a width equal to  $V_{sd}$  [17]. In Fig. 2.9 an  $I(V_g, B)$  gray scale plot is given of the  $N = 2$  stripe measured for  $V_{sd} = 4$  mV. The edges of the stripe represent the ground state electro-chemical potential  $\mu(2)$ , which clearly contain the ST transition at  $\sim 4.5$  T. Within the stripe, we clearly observe the first excited state. The down-going  $B$ -dependence of the first excited state is similar to  $\mu^{\uparrow\uparrow}(2)$  (dotted curve in Fig. 2.7). The crossing of the dashed curves in Fig. 2.9 is a direct observation of a crossing between the first excited state and ground state, which is in close agreement with Fig. 2.7.

We briefly discuss the  $N = 3$  and 4 curves in Fig. 2.8a, which both contain two kinks. The left kink (labeled "b") in  $\mu(3) = U(3) - U(2)$  is not due to a

transition in the energy  $U(3)$  of the three electron system, but is a remnant of the two electron ST transition in  $U(2)$ . The right kink (labeled "c") corresponds to the transition from  $U(3) = E_{0,0}(\uparrow) + E_{0,0}(\downarrow) + E_{0,1}(\uparrow) + 3E_c$  to the spin-polarized case  $U(3) = E_{0,0}(\uparrow) + E_{0,1}(\uparrow) + E_{0,2}(\uparrow) + 3E_c$ . Detailed analysis shows that also this transition to increasing total angular momentum and total spin is driven largely by interactions. Similar transitions occur for the  $N = 4$  system where on the right of the last kink (labeled "e") the system is again in a polarized state with sequential filling of the angular momentum states:  $U(4) = E_{0,0}(\uparrow) + E_{0,1}(\uparrow) + E_{0,2}(\uparrow) + E_{0,3}(\uparrow) + 6E_c$ .

In conclusion, we use single-electron tunneling spectroscopy to probe electronic states of a few-electron vertical quantum dot-atom. At zero magnetic field the addition energy reveals a shell structure associated with a 2D harmonic potential. As a function of magnetic field, current peaks evolve in pairs, arising from the antiparallel filling of spin-degenerate states. Close to zero magnetic field, however, this pairing behavior is altered to favour the filling of states with parallel spins in line with Hund's rule. The results are in good agreement with an extended constant interaction model. For the system with two electrons  $N = 2$  we investigate a singlet-triplet transition. In this case the extended constant interaction is not sufficient to explain the value of the magnetic field at which the transition occurs.

We thank H. Akera, R.J. van der Hage, T. Fujisawa, J. Janssen, Y. Kerven-  
nic, J.E. Mooij, S.K. Nair, R. Schouten, H. Tamura, Y. Tokura, T. Uesugi and  
M. Wegewijs for help and discussions. The work was supported by the Dutch  
Foundation of Fundamental Research on Matter (FOM) and L.P.K. by the Royal  
Netherlands Academy of Arts and Sciences (KNAW).

## References

- [1] See for reviews in popular magazines: M. Reed, *Scientific American* **268**, 118 (1993); M.A. Kastner, *Physics Today* **46**, 24 (1993); R.C. Ashoori, *Nature* **379**, 413 (1996); C.J.P.M. Harmans, *Physics World* **5**, 50 (March 1992); L.P. Kouwenhoven and C.M. Marcus, *Physics World* **11**, (June 1998).
- [2] See for a review on quantum dots: L.P. Kouwenhoven, C.M. Marcus, P.L. McEuen, S. Tarucha, R.M. Westervelt and N.S. Wingreen, *Electron transport in quantum dots*, in *Mesoscopic Electron Transport*, edited by L.L. Sohn, G. Schön and L.P. Kouwenhoven, June 1996 (Kluwer, Series E 345, 1997), p. 105-214; see also: <http://vortex.tn.tudelft.nl/~leo/papers/>.
- [3] S. Tarucha, D.G. Austing, T. Honda, R.J. van der Hage and L.P. Kouwen-

- hoven, Phys. Rev. Lett. **77**, 3613 (1996).
- [4] M. Alonso and E.J. Finn, *Quantum and Statistical Physics* (Addison-Wesley, 1968); L. I. Schiff, *Quantum Mechanics* (MacGraw-Hill, 1949).
- [5] H. Mizuto and T. Tanoue, *The Physics and Applications of Resonant Tunneling Diodes*, (Cambridge, 1996).
- [6] Y. Tokura (private communications).
- [7] B. Su, V.J. Goldman and J.E. Cunningham, Phys. Rev. B **46**, 7644 (1992); T. Schmidt, M. Tewordt, R.H. Blick, R.J. Haug, D. Pfannkuche, K. von Klitzing, A. Förster and H. Lüth, Phys. Rev. B **51**, 5570 (1995).
- [8] M. Tewordt, L. Martín-Moreno, V.J. Law, M.J. Kelly, R. Newbury, M. Pepper, D.A. Ritchie, J.E.F. Frost and G.A.C. Jones, Phys. Rev. B **46**, 3948 (1992).
- [9] M.W. Dellow, P.H. Beton, C.J.G.M. Langerak, T.J. Foster, P.C. Main, L.Eaves, M. Henini, S.P. Beaumont and C.D.W. Wilkinson, Phys. Rev. Lett. **68**, 1754 (1992); P. Gueret, N. Blanc, R. Germann and H. Rothuizen, Phys. Rev. Lett. **68**, 1896 (1992).
- [10] S. Tarucha, D.G. Austing and T. Honda, Superlattices and Microstructures **18**, 121 (1995).
- [11] R.C. Ashoori, H.L. Störmer, J.S. Weiner, L.N. Pfeiffer, S.J. Pearton, K.W. Baldwin and K.W. West, Phys. Rev. Lett. **68**, 3088 (1992).
- [12] R.C. Ashoori, H.L. Störmer, J.S. Weiner, L.N. Pfeiffer, K.W. Baldwin and K.W. West, Phys. Rev. Lett. **71**, 613 (1993).
- [13] D.G. Austing, T. Honda, Y. Tokura and S. Tarucha, Jap. J. Appl. Phys. **34**, 1320 (1995); D. G. Austing, T. Honda and S. Tarucha, Semicond. Sci. Technol. **11**, 388 (1996).
- [14] C. G. Darwin, Proc. Cambridge Philos. Soc. **27**, 86 (1930); V. Fock, Z. Phys. **47**, 446 (1928).
- [15] M. Macucci, K. Hess and G.J. Iafrate, Phys. Rev. B **48**, 17354 (1993); A. Natori, M. Fujito, H. Yasunaga, Superlattices and Microstructures **22**, 65 (1997); A. Angelucci and A. Tagliacozzo, Phys. Rev. B **56**, R7088 (1997); M. Koskinen, M. Manninen, S.M. Reimann, Phys. Rev. Lett. **79**, 1389 (1997); I.H. Lee, V. Rao, R.M. Martin, J.P. Leburton, Phys. Rev. B **57**, 9035 (1998); M. Rontani, F. Rossi, F. Manghi and E. Molinari, Appl. Phys. Lett. **72**, 957 (1998).

- [16] V. Halonen, P. Hyvönen, P. Pietiläinen and Tapash Chakraborty, *Phys. Rev. B* **53**, 6971 (1996).
- [17] L.P. Kouwenhoven, T.H. Oosterkamp, M.W.S. Danoesastro, M. Eto, D.G. Austing, T. Honda, and S. Tarucha, *Science* **278**, 1788 (1997); see also chapter 3 in this thesis; W.G. van der Wiel, *Physica B* **256-258**, 173-177 (1998).
- [18] M. Wagner, U. Merkt, and A.V. Chaplik, *Phys. Rev. B* **45**, 1951 (1992).
- [19] An analogous singlet-triplet transition is predicted to occur in He atoms in the vicinity of white dwarfs and pulsars at  $B = 4 \cdot 10^5$  T, see G. Thurner, H. Herold, H. Ruder, G. Schlicht, and G. Wunner, *Phys. Lett.* **89A**, 133 (1982). Due to the larger dimensions, the transition is expected to occur around 4.5 T in our dots.
- [20] A small irregularity is visible around 3 T. This feature cannot be ascribed to a crossing of states in the dot, which is verified at finite source-drain voltages where both ground and excited states can be distinguished



## Chapter 3

# Excitation spectra of circular, few-electron quantum dots

L.P. Kouwenhoven, T.H. Oosterkamp,  
M.W.S. Danoesastro, M. Eto,  
D.G. Austing, T. Honda, and S. Tarucha.

### Abstract:

Studies of the ground and excited states in semiconductor quantum dots containing 1 to 12 electrons show that the quantum numbers of the states in the excitation spectra can be identified and compared to exact calculations. A magnetic field induces transitions between ground and excited states. These transitions are discussed in terms of crossings between single-particle states, singlet-triplet transitions, spin polarization, and Hund's rule. These impurity-free quantum dots allow "atomic physics" experiments to be performed in magnetic field regimes not accessible for atoms.

Small solid state devices known as quantum dots are often referred to as artificial atoms because their electronic properties resemble, for example, the ionization energy and discrete excitation spectrum of atoms [1]. Quantum dots are usually fabricated between source and drain contacts so that the atom-like properties can be probed in current-voltage ( $I$ - $V$ ) measurements. Additionally, with a gate electrode nearby, one can vary the exact number of electrons  $N$  on the quantum dot by changing the gate voltage  $V_g$ . When an electron is added, the total charge on the dot changes by the elementary charge  $e$ . The associated energy change, known as the addition energy, is a combination of the single electron charging energy and the change in single-particle energy. Charging effects and discrete single-particle states have recently been studied in a variety of quantum dot systems, defined not only in semiconductors but also in metal grains and molecules [2].

Quantum dot devices usually contain some disorder caused, for example, by impurities [2]. Clean quantum dots, in the form of regular disks, have only recently been fabricated in a semiconductor heterostructure [3,4]. The circular symmetry of the two dimensional (2D) disks gives rise to a 2D shell structure in the addition energies, analogous to the 3D shell structure in atomic ionization energies [5]. Measurements of the ground states have shown that the 2D shells in dots are filled according to Hund's rule [4]: Up to half shell filling, all electrons have parallel spins; more electrons can only be added with antiparallel spins. We now report the excitation spectra for dots with different numbers of electrons and identify the quantum numbers of the excited states. We also show the relation between spectra of successive  $N$  and how the spectra evolve with an applied magnetic field  $B$ . The relatively large dimension of quantum dots ( $\sim 100$  nm) allows one to use accessible  $B$ -fields that would correspond in real atoms to inaccessible fields of the order  $10^6$  T.

Fig. 3.1a shows a schematic drawing of the device which, from bottom to top, consists of an n-doped GaAs substrate, undoped layers of 7.5 nm  $\text{Al}_{0.22}\text{Ga}_{0.78}\text{As}$ , 12 nm  $\text{In}_{0.05}\text{Ga}_{0.95}\text{As}$ , 9.0 nm  $\text{Al}_{0.22}\text{Ga}_{0.78}\text{As}$ , and a  $\sim 500$  nm n-doped GaAs top layer. A sub-micrometer pillar is fabricated using electron-beam lithography and etching techniques [3]. Source and drain wires are connected to the top and substrate contacts and a third wire is attached to the metal side gate which is placed around the pillar. The energy landscape is shown in Fig. 3.1b. The  $\text{AlGaAs}$  layers are insulating, but thin enough to allow for tunneling from the source to drain through the central, disk-shaped  $\text{InGaAs}$  layer. By making  $V_g$  more negative the effective diameter of this disk can be reduced from a few hundred nanometers down to zero, decreasing  $N$  one-by-one from  $\sim 70$  to zero. At a particular  $V_g$ , we can probe the excitation spectrum by increasing the source-

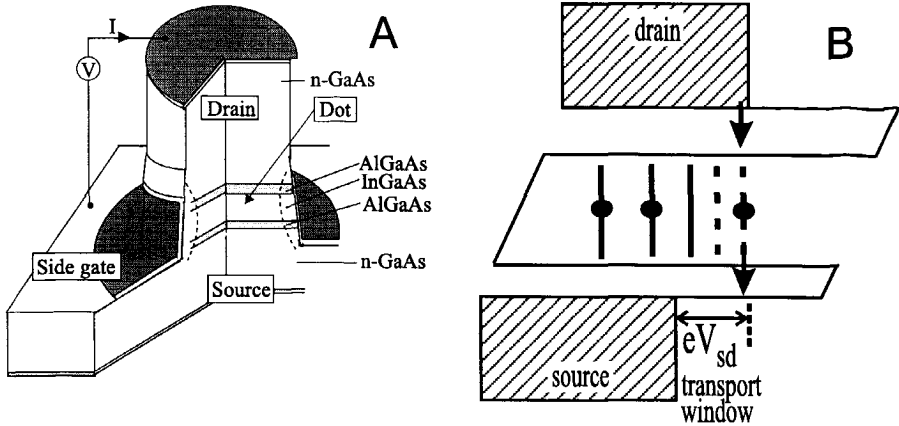


Figure 3.1: (a) Schematic of the semiconductor layers and the metal side gate. The diameter of the pillar is  $0.5 \mu\text{m}$ . (b) Schematic energy (horizontal axis) diagram along the vertical axis of the pillar. Hatched regions are occupied electron states in the source and drain contacts. For the case shown, two electrons are permanently trapped in the quantum dot. The third electron can choose to tunnel through the  $N = 3$  ground state (solid line) or through one of the two excited states which lie in the transport window. This situation corresponds to the  $N = 3$  current stripe.

drain voltage,  $V_{sd}$ , which opens up a transport window between the Fermi energies of the source and drain. Only ground states and excited states lying within this energy window contribute to  $I$  (see Fig. 3.1b). When  $V_g$  is increased, the levels in Fig. 3.1b shift down in energy; when an extra state moves through the Fermi energy of the drain  $I$  increases. Unlike atoms, excitations do not occur inside the dot by, for instance, absorption of radiation. For dots, excitations are created when an electron tunnels out from the ground state and the next electron tunnels in to an excited state. The devices are measured in a dilution refrigerator with the temperature set at 100 mK.

The differential conductance  $I/V_{sd}$  as a function of  $V_{sd}$  and  $V_g$  is shown in Fig. 3.2 for  $N$  increasing from 0 to 12. Along the  $V_{sd} \approx 0$  axis  $N$  changes to  $N + 1$  when adjacent diamond-shaped regions of zero current touch. The size of the diamonds is a measure of the minimum energy to add or subtract an electron. The diamonds for  $N = 2, 6,$  and  $12$  are unusually large, which correspond to filled shells [4]. At the two upper edges of the  $N$  electron diamond, an extra electron

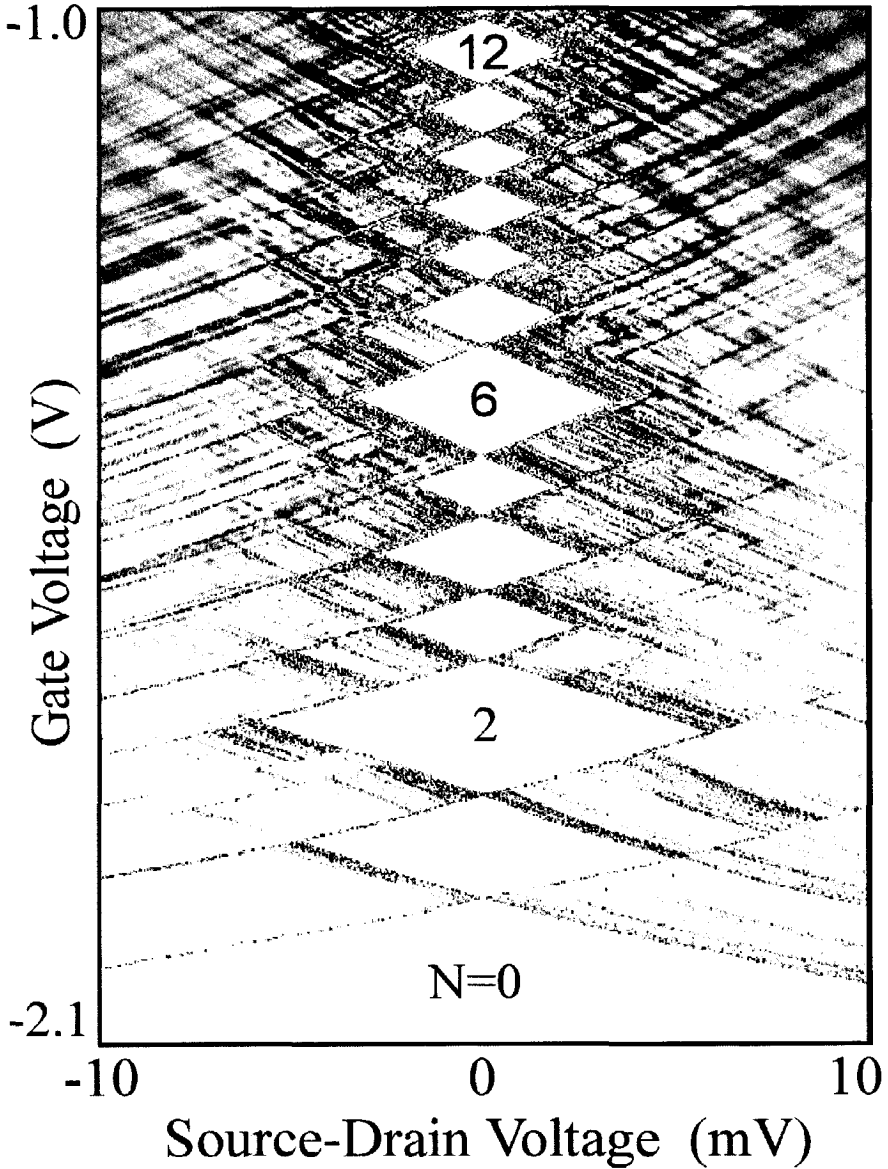


Figure 3.2: Differential conductance  $I/V_{sd}$  plotted in color scale in the  $V_g - V_{sd}$  plane at  $B = 0$ . In the white diamond shaped regions,  $I/V_{sd} \approx 0$  due to Coulomb blockade.  $N$  is fixed in each of the diamond regions. The lines outside the diamonds, running parallel to the sides, identify excited states.

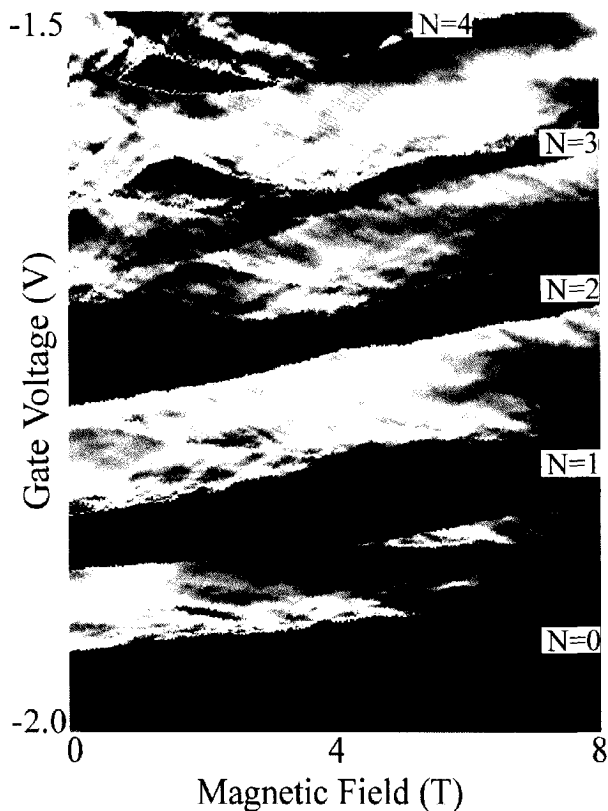


Figure 3.3:  $I(V_g, B)$  for  $N = 0$  to 4 and a part of  $N = 5$  measured with  $V_{sd} = 3$  meV.  $I < 0.1$  pA in the dark blue regions and  $I > 10$  pA in the dark red regions. Both ground states and the first few excited states can contribute to the current. Current stripes between the Coulomb blockade regions (dark blue) for  $N - 1$  and  $N$  electrons are called the  $N$  electron stripe throughout the report.

can tunnel through the dot via the  $N + 1$  electron ground state. Excited states of the  $N + 1$  electron system that enter the transport window are seen as "lines" running parallel to the upper edges of the diamond. At the two lower edges of a diamond, an electron can tunnel out of the dot ( $N$  to  $N - 1$  transitions). However, some of the lines outside the diamonds in Fig. 3.2 could be due to fluctuations in the density of states in the narrow leads [6,7]. Below we show that we can distinguish between lead and disk states by measuring  $I(V_g, B)$  for different values for  $V_{sd}$  and for  $B$  being parallel to  $I$ .

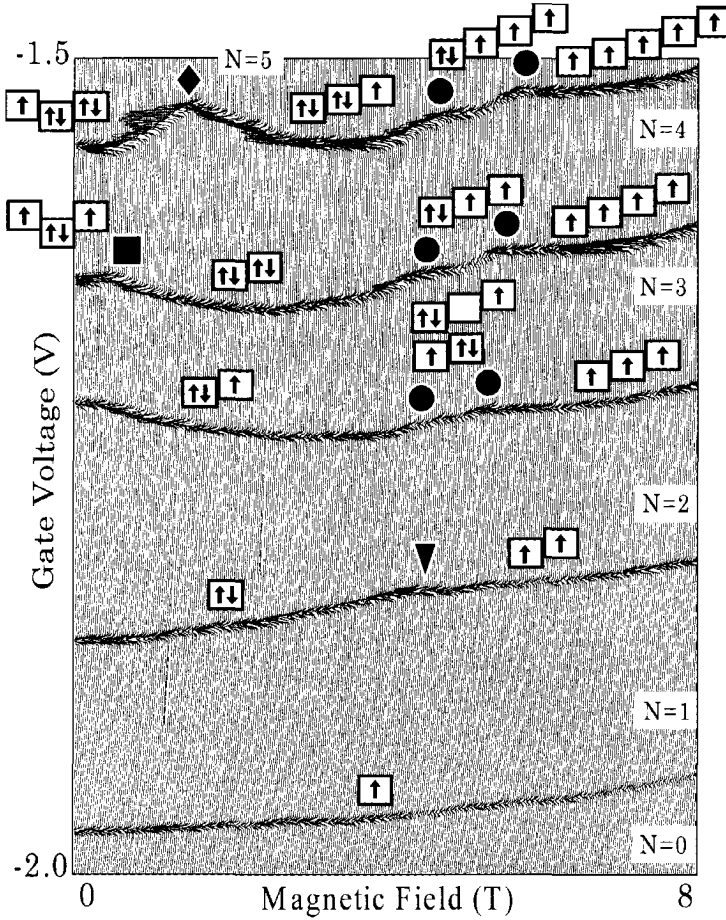


Figure 3.4:  $I(Vg, B)$  for  $N = 0$  to 5 measured with small  $V_{sd} = 0.1$  meV such that only ground states contribute to the current. Ground state transitions are indicated by different labels. The arrows in the squares indicate the spin configuration. The lowest square corresponds to a single-particle state with angular momentum  $l = 0$ . For squares to the right  $l$  increases to 1, 2, 3, etc. For  $N = 4$  and 5, near  $B = 0$ , also the  $l = -1$  square is shown on the left of the  $l = 0$  square. For  $N = 3$  there are two important configurations for the occupation of single-particle states in the region between the two kinks.

Fig. 3.4 shows the  $B$ -field dependence of the ground states. We have taken  $V_{sd} = 0.1$  mV so that only ground states can lie within the transport window. The observed peaks in the current at  $B = 0$  directly correspond to where the  $N = 0$  to  $N = 5$  diamonds touch each other in Fig. 3.2. The  $B$ -field dependence of the peak positions in gate voltage reflects the evolution of the ground state energies. Besides an overall smooth  $B$ -field dependence, we observe several kinks which we have labeled. For the regions between kinks, we can identify the quantum numbers, including the spin configurations.

Increasing  $V_{sd}$  to 3 mV yields the data summarized in Fig. 3.3 [8]. The transport window is such that  $I$  is non-zero over wider  $V_g$  ranges. Instead of the "sharp" current peaks as in Fig. 3.4, we now observe "stripes". Adjacent stripes sometimes overlap, implying that here  $eV_{sd}$  exceeds the addition energy. The lower edge of the  $N^{th}$  current stripe (which lies between the Coulomb blockade regions of  $N - 1$  and  $N$  electrons) measures when the ground state of the  $N$  electron dot enters the transport window as  $V_g$  is made more positive. Inside a stripe, the somewhat random-looking and less-pronounced changes in  $I$  are attributed to fluctuations in the density of states in the leads [6]. However, also inside the stripes changes in  $I$  can be seen as pronounced curves, which we will argue are the excited states in the dot.

For  $N = 1$ , a transport window of 3 meV is too small to observe the excitations clearly. Therefore, we show in Fig. 3.5a the  $N = 1$  stripe and a part of the  $N = 2$  stripe for  $V_{sd} = 5$  mV. For this voltage, the  $N = 1$  and 2 stripes just touch at  $B = 0$ . A pronounced change in  $I$  [that is, from blue ( $< 1$  pA) to dark red ( $> 10$  pA)] occurs at the upper edge of the  $N = 1$  stripe at  $B = 0.2$  T. This change identifies the first excited state for the  $N = 1$  dot [we discuss the index (0,1) below]. At higher  $B$  values higher excited states also enter the stripe. The energy separation between ground state and first excited state can be read from the relative position inside the stripe. For instance, when the first excited state is two-thirds of the width of the stripe away from the ground state, the excitation energy is two-thirds of  $eV_{sd}$ . So, the excitation energy is 5 meV at  $B = 0$  and decreases for increasing  $B$ . Even over this wide  $B$  range of 16 T, the first excited state never crosses with the ground state. Below 4 T, the excitation energy exceeds 3 meV and therefore the first excited state only starts to become visible for  $B > 4$  T in the first stripe of Fig. 3.3.

In the second,  $N = 2$ , stripe in Fig. 3.3, we see the first excited state crossing the ground state at  $B = 4.15$  T; that is, the first excited state for  $B < 4.15$  T (seen as the change in  $I$  from blue to red inside the second stripe) becomes the ground state for  $B > 4.15$  T. The kink labeled by the triangle in Fig. 3.4 also denotes this crossing. For  $N = 3$  and 4, we also observe a crossing at 1.7 T in the

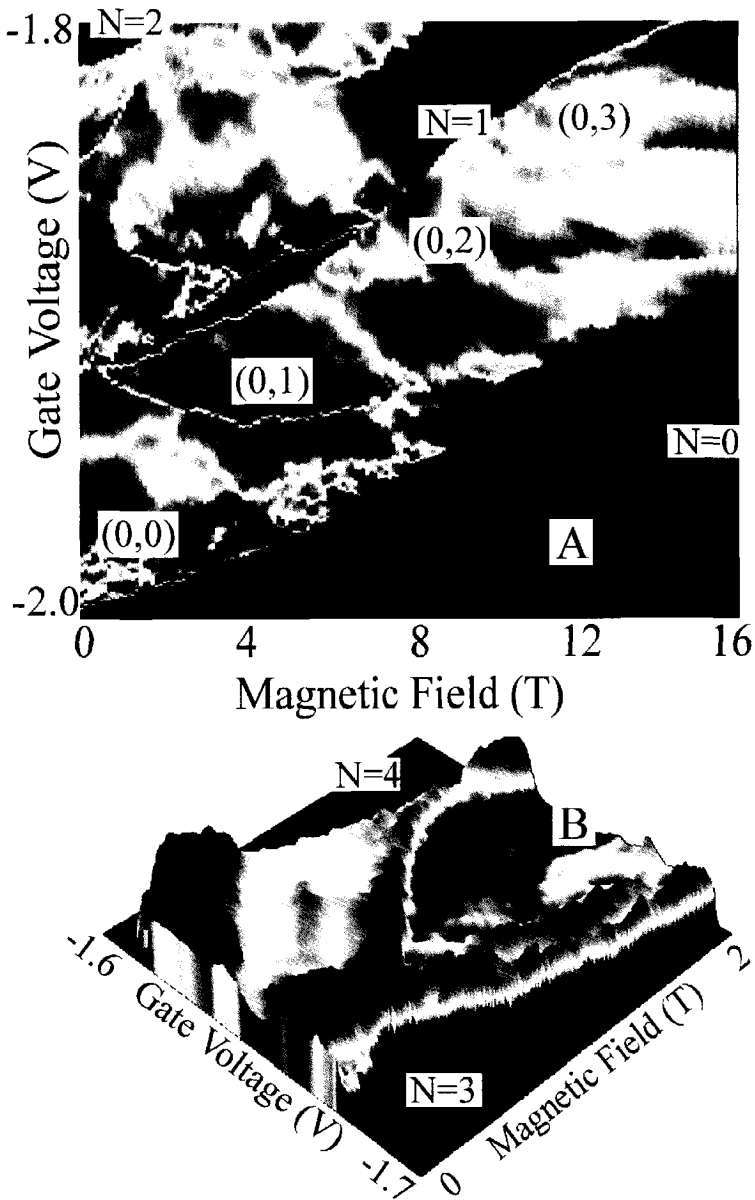


Figure 3.5: a)  $I(V_g, B)$  for  $N = 1$  and  $2$  measured with  $V_{sd} = 5$  meV up to  $16$  T. The states in the  $N = 1$  stripe are indexed by the quantum numbers  $(n, l)$ . (b) Surface plot of the  $N = 4$  stripe measured with  $V_{sd} = 1.6$  meV up to  $2$  T.



middle of the third and fourth stripes in Fig. 3.3 between an up-going excited state and a down-going excited state. A similar up and-down going crossing is seen in the ground state for  $N = 5$  at 1.2 T (see also the kink in Fig. 3.4 labeled by the diamond).

To describe the electron states in a quantum dot, we must calculate the energy spectrum  $U(N, B)$ . In our experiment we measure the electrochemical potential of the quantum dot which is defined as  $\mu(N) \equiv U(N) - U(N - 1)$ . For a few electrons,  $U(N, B)$  can be calculated exactly, including the Coulomb interactions [9]. However, it is easier to explain the experimental results when we first consider the spectrum of non-interacting electrons in a 2D circular disk. The thickness of the thin disk freezes the electrons in the lowest state in the vertical direction. We therefore only have to consider the confinement in the plane of the disk. For this we take a parabolic potential  $V(r) = \frac{1}{2}m^*\omega_0^2r^2$ , where  $m^* = 0.06m_0$  is the effective mass of electrons in our InGaAs disk. The single-particle eigenenergies with radial quantum number  $n = 0, 1, 2, \dots$  and angular momentum quantum number  $l = 0, \pm 1, \pm 2, \dots$  are given by [10]:

$$E_{n,l} = (2n + |l| + 1)\hbar\sqrt{\frac{1}{4}\omega_c^2 + \omega_0^2} - \frac{1}{2}l\hbar\omega_c \quad (3.1)$$

where the cyclotron frequency  $\omega_c = eB/m^*$  and  $\hbar$  is Planck's constant divided by  $2\pi$ . We neglect the much smaller Zeeman energy. The first few spin-degenerate states,  $E_{n,l}$ , are plotted in Fig. 3.6a for a confinement energy  $\omega_0 = 5$  meV. The two thick solid lines identify the transport window relative to the (0,0) curve for  $V_{sd} = 5$  mV. The states within this stripe can be compared to the changes in  $I$  seen in the  $N = 1$  stripe in Fig. 3.5a. The agreement is not unexpected because the non-interacting model of Eq. 3.1 is in fact exact for  $N = 1$ . We note that Eq. 3.1 with  $\omega_0 = 5$  meV fits both the ground state and the first excited state very well up to about 7 T [11].

If we first neglect Coulomb interactions for  $N = 2$ , then the two-electron ground state energy is given by  $U(N = 2) = 2E_{0,0}$  and the measured value for  $\mu(2) = U(2) - U(1) = E_{0,0} = \mu(1)$ . The simplest way to include interactions is to assume that the Coulomb energy  $E_c$  is independent of  $B$ . In this constant interaction model,  $\mu(2) - \mu(1) = E_c$ ; implying that the first and second peaks in  $I$  are separated by a constant  $V_g$  and both peaks have the same  $B$ -field dependence. The constant interaction model has been successful in describing most Coulomb blockade experiments [1,2]. However, we see in Figs. 3.4 and 3.3 that the  $N = 1$  and 2 ground states evolve differently with  $B$ . In particular, while  $E_{0,0}$  is the  $N = 1$  ground state over the entire  $B$  range, a transition occurs at 4.15 T in the  $N = 2$  ground state. To explain this transition we have to consider that the

$l = 0$  orbits shrink in size when  $B$  is turned on. Two electrons in a shrinking  $l = 0$  orbit experience an increasing Coulomb interaction. (We indeed observe in Fig. 3.4 that the second peak increases faster with  $B$  compared to the first peak.) The increasing Coulomb interaction will, at some  $B$  value, force one of the two electrons to occupy the larger  $l = 1$  orbit. This transition costs kinetic energy  $E_{0,1} - E_{0,0}$ , but it reduces the Coulomb interaction because of the larger spatial separation between the two electrons. In addition, the system gains exchange energy when the two electrons take on parallel spins. The transition in angular momentum is thus accompanied by a transition in the total spin from the singlet  $S = 0$  to the triplet state  $S = 1$ . An analogous singlet-triplet (S-T) transition is predicted to occur in He atoms in the vicinity of white dwarfs and pulsars at  $B = 4 \times 10^5$  T [12]. Because of the much larger size of our artificial atoms, the transition occurs at accessible fields of a few Tesla. This effect was first predicted by Wagner et al. [13] and evidence for the S-T crossing has been seen [14].

The exact calculation in Fig. 3.6b of  $\mu(N)$  for the  $N = 2$  to 5 ground states and first two excited states shows extra transitions between many-body states that are not included in the single-particle states of Eq. 3.1 [15]. The S-T transition for  $N = 2$  is one such example [16]. In Fig. 3.6a,  $E_{0,0}$  never crosses with  $E_{0,1}$ , whereas in Fig. 3.6b a transition labeled by a triangle occurs between the first (dashed) excited state and (solid) ground state at  $\omega_c = 1.5\omega_0$ . For  $\omega_0 = 5$  meV, this S-T transition is expected at  $B = 4.2$  T (the experimental value is 4.15 T). The calculated second (dotted) excited state in Fig. 3.6b for  $N = 2$  can also be seen in the second stripe of Fig. 3.5a (the line between blue and red current regions which has a maximum near  $\sim 2$  T).

We now discuss transitions between the first excited state and the ground state for  $N = 3, 4,$  and  $5$ . The ground state for  $N = 3$  has two transitions labeled by circles. On increasing  $B$ , the total spin,  $S$ , and total angular momentum,  $M$ , of the many-body states changes from  $(S, M) = (\frac{1}{2}, 1)$  to  $(\frac{1}{2}, 2)$  to  $(\frac{3}{2}, 3)$ . These transitions to larger angular momentum states reduce the Coulomb interactions [1]. In addition, the spin increases in order to gain exchange energy. A double transition in the ground state energy is indeed observed as two kinks in the  $N = 3$  trace of Fig. 3.4. In most regions in Fig. 3.4, there is one main configuration for the occupation of single-particle states. For  $N = 3$ , in the region between the two circles, there are two important configurations, which both have the same  $S$  and  $M$ . In a similar way, the  $N = 4$  and  $5$  ground states make transitions to higher angular momentum states and an increasing total spin when  $B$  is increased. The occupation of many-body states in the region between the two circles is hard to determine because in this region different states lie very close in energy (see Fig. 3.6b). For  $B$  larger than the right circles, there is again a clear ground

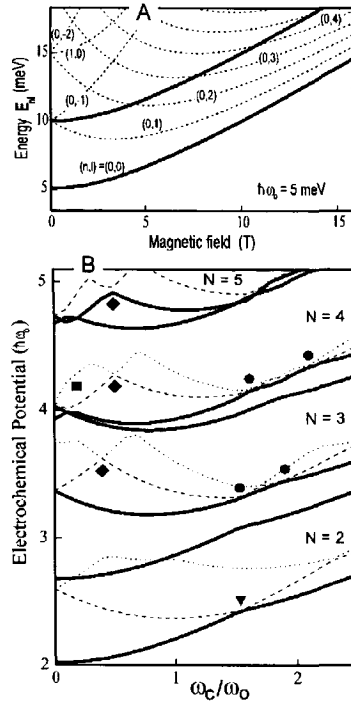


Figure 3.6: a) Calculated energy spectrum from Eq. 3.1 for  $N = 1$  and  $\omega_0 = 5$  meV. The lowest thick line is the ground state energy. The upper thick line is the ground state energy shifted upwards by 5 meV. Dashed states between the two thick lines can be seen in the experimental stripe for  $N = 1$  in Fig. 3.5. (b) Exact calculation of energy spectra for  $N = 2$  to 5. Current stripes of width  $0.66\hbar\omega_0$  are bounded by solid lines. The Coulomb blockade regions are hatched. For  $\omega_0 = 5$  meV,  $\omega_c = \omega_0$  corresponds to 2.8 T. The square, circle, triangle and diamond symbols indicate the same transitions as in Fig. 3.4.

state where electrons are fully spin-polarized and they occupy successive angular momentum states.

A different type of crossing is between two excited states (crossings inside a stripe). We now argue that the crossing between two excited states in the  $N = 3$  and 4 stripes labeled by diamonds in Fig. 3.6b is a crossing between single-particle states. For non-interacting electrons, we expect from Fig. 3.6a that  $E_{0,0}$  and  $E_{0,1}$  are the two occupied single-particle states in the ground states

for both  $N = 3$  and 4. The first excited state is  $E_{0,-1}$  for  $B < 2$  T and  $E_{0,2}$  for  $B > 2$  T. Together with the ground state they form a triangle. The same triangular shape is observed in both the  $N = 3$  and  $N = 4$  stripes in Fig. 3.3 where it has a maximum near 1.7 T. Continuing these arguments we expect the transition in the first excited state for  $N = 3$  and 4 to become a transition in the ground state for  $N = 5$ . Indeed this is seen in Fig. 3.3 and at the kink labeled by the diamond in Fig. 3.4 (this transition in  $l$  from -1 to 2 is indicated in Fig. 3.4 in the diagrams adjacent to this kink). We emphasize that the discussion of the above crossings demonstrates a direct relation between the excitation spectrum of an  $N$  electron system with the ground state of the  $N + 1$  electron system [17].

The last crossing we discuss is indicated by the square in Fig. 3.4. We have identified this crossing earlier [4] as a manifestation of Hund's rule. As the adjacent spin diagrams show for the third and fourth electrons a transition from parallel spins (in accordance with Hund's rule) to antiparallel spins occurs. When the states  $E_{0,1}$  and  $E_{0,-1}$  are sufficiently close, there is an energy gain due to the exchange interaction between electrons with parallel spins. As  $B$  is increased,  $E_{0,1}$  and  $E_{0,-1}$  diverge from each other (see Fig. 3.6a) and at some value a transition is made to antiparallel spins where the third and fourth electrons both occupy  $E_{0,1}$ . Fig. 3.5b shows a surface plot of the  $N = 4$  stripe measured at  $V_{sd} = 1.6$  mV. This surface plot shows the  $B$  dependence of the single-particle states  $E_{0,1}$  and  $E_{0,-1}$  including a Hund's rule crossing between the ground state and first excited state at 0.4 T. Interestingly, a second excited state is seen with a  $B$  dependence parallel to the first excited state. Parallel first and second excited states are also seen in the calculation of Fig. 3.6b (see just above and below the square label in the  $N = 4$  stripe). The difference between the two parallel lines is that in the lower energy line the third and fourth electrons have parallel spins (in accordance with Hund's rule) and in the higher energy line they have antiparallel spins. The energy difference is a direct measure of the exchange energy. From the experimental  $N = 4$  stripe in Fig. 3.3 we can read directly that the gain in exchange energy is  $\sim 1$  meV.

We thank R.J. van der Hage, J. Janssen, Y. Kervennic, J.E. Mooij, S.K. Nair, L.L. Sohn, Y. Tokura, and T. Uesugi for help and discussions. The work was supported by the Dutch Foundation for Fundamental Research on Matter (FOM). L.P.K. was supported by the Royal Netherlands Academy of Arts and Sciences (KNAW).

## References

- [1] R.C. Ashoori, *Nature* **379**, 413 (February, 1996).
- [2] See for a review on quantum dots: L.P. Kouwenhoven, C.M. Marcus, P.L. McEuen, S. Tarucha, R.M. Westervelt and N.S. Wingreen, *Electron transport in quantum dots*, in *Mesoscopic Electron Transport*, edited by L.L. Sohn, G. Schön and L.P. Kouwenhoven, June 1996 (Kluwer, Series E 345, 1997), p. 105-214; see also: <http://vortex.tn.tudelft.nl/~leo/papers/>.
- [3] D.G. Austing, T. Honda, S. Tarucha, *Semicond. Sci. Technol.* **11**, 212 (1996).
- [4] S. Tarucha, D.G. Austing, T. Honda, R.J. van der Hage, L.P. Kouwenhoven, *Phys. Rev. Lett.* **77**, 3613 (1996). B.L. Altshuler et al., *Phys. Rev. Lett.* **66**, 88 (1991).
- [5] M. Alonso and E.J. Finn, *Quantum and Statistical Physics* (Addison-Wesley 1968).
- [6] T. Schmidt et al., *Phys. Rev. Lett.* **78**, 1544 (1997).
- [7] Fig. 3.2 actually reproduces in large detail in four different samples implying that the structure in the density of states in the leads is not originating from a random impurity potential but probably from the lateral confinement potential of the pillar.
- [8] The sign of  $V_{sd}$  is such that electrons first tunnel through the thicker barrier. In this situation, only the excited states above the ground state electrochemical potential are observed. For equal tunnel barriers tunneling out of the dot from excited states below the ground state electrochemical potential can also be measured; see [2]. Note that for a thick enough entrance barrier we can assume relaxation to the ground- state between tunneling out and tunneling into the dot of the next electron.
- [9] See for example: J.J. Palacios, L. Martin-Moreno, G. Chiappe, E. Louis, C. Tejedor, *Phys. Rev. B* **50**, 5760, (1994); See for more references the review by N.F. Johnson, *J. Phys.: Condens. Matter* **7**, 965 (1995).
- [10] V. Fock, *Z. Phys.* **47**, 446 (1928); C.G. Darwin, *Proc. Cambridge Philos. Soc.* **27**, 86 (1930).
- [11] We believe that the smaller slopes in the experimental data of Fig. 3.5 for  $B \gtrsim 7$  T are due to a changing confinement potential because screening from the leads is modified by the formation of Landau levels in the leads. This is also reflected in the changing stripe width at high B.)

- [12] G. Thurner, H. Herold, H. Ruder, G. Schlicht, G. Wunner, *Phys. Lett.* **89A**, 133 (1982).
- [13] M. Wagner, U. Merkt, A.V. Chaplik, *Phys. Rev. B* **45**, 1951 (1992).
- [14] B. Su, V.J. Goldman, J.E. Cunningham, *Phys. Rev. B* **46**, 7644 (1992); R.C. Ashoori, et al., *Phys. Rev. Lett.* **71**, 613 (1993); T. Schmidt et al., *Phys. Rev. B* **51**, 5570 (1995).
- [15] See for details of the calculation: M. Eto, *Jpn. J. Appl. Phys.* **36**, 3924 (1997). In the numerically exact calculations, every electron is assumed to occupy one of the lowest 15 single-particle states at  $B = 0$ . The strength of the Coulomb interaction is fixed such that  $e^2/\varepsilon\sqrt{\hbar/m^*\omega_0} = \hbar\omega_0$  ( $\varepsilon$  is the permittivity). (Interactions between electrons in the dot and in the leads are neglected.) The calculated results indicate that the many-body states consist of one main configuration [two main configurations for  $N = 3$  and  $(S, M) = (\frac{1}{2}, 2)$ ] and several small contributions from other configurations. The depicted configurations in Fig. 3.4 overlap by  $\sim 70\%$  or more with the many body ground states (the spin-polarized states overlap by more than 95%).
- [16] For a theoretical analyses of the  $N = 2$  excitation spectrum see e.g.: D. Pfannkuche, R.R. Gerhardts, P.A. Maksym, V. Gudmundsson, *Physica B* **189**, 6 (1993).
- [17] Also in  $N \sim 100$  quantum dots the excitation spectra of  $N$  and  $N+1$  can be strongly correlated, as observed recently by D. R. Stewart, et al. *Science* **278**, 1784 (1997).

## Chapter 4

# Stability of the maximum density droplet in quantum dots at high magnetic fields

T.H. Oosterkamp, J.W. Janssen, L.P. Kouwenhoven,  
D.G. Austing, T. Honda and S. Tarucha.

### **Abstract:**

We have measured electron transport through a vertical quantum dot containing a tunable number of electrons between 0 and 40. Over some region in magnetic field the electrons are spin polarized and occupy successive angular momentum states, i.e. the maximum density droplet (MDD) state. The stability region where the MDD state is the ground state, decreases for increasing electron number. The instability of the MDD is accompanied by a redistribution of charge which increases the area of the electron droplet.

Quantum dots are small semiconductor devices containing a tunable number of electrons that occupy discrete quantum states. Their properties combine remarkable similarities to atoms with the flexibility to study the energy spectra for different shapes and sizes of the confinement potential [1, 2]. The electron orbits are significantly modified in a magnetic field of a few Tesla. In a large 2D electron gas (2DEG) the scale of a few Tesla corresponds to the quantum Hall regime. In this letter we study quantum dots in the quantum Hall regime and exploit the fact that dots contain a tunable and well-defined number of electrons. In particular, we focus on the spin-polarized, maximum-density-droplet state that corresponds to filling factor  $\nu = 1$  in a 2DEG. The stability of this spin-polarized state is set by a balance of forces acting on this finite electron system; namely the inward force of the confining potential, the repulsive force of the direct Coulomb interaction between electrons, and a binding force due to the exchange interaction. By tuning the relative strengths of these forces with the magnetic field and the electron number, we study transitions which reconstruct the *charge distribution* of this many-body system.

Our vertical quantum dot is made from a double barrier resonant tunneling structure with an InGaAs well, AlGaAs barriers, and  $n$ -doped GaAs source and drain contacts [3]. The heterostructure is processed in the shape of a submicron circular pillar with a diameter of  $0.54 \mu\text{m}$  and a self-aligned gate around it. We discuss data taken on one particular device but comparable results have been obtained on several devices. A magnetic field,  $B$ , is applied parallel to the tunneling current (i.e. perpendicular to the plane in which the electrons are confined). The energy spectrum of the quantum dot is derived from transport experiments at a temperature of 100 mK in the Coulomb blockade regime. A small dc source-drain voltage,  $V_{SD}$ , is applied and the current,  $I$ , is measured versus gate voltage,  $V_g$ , which reduces the electron number,  $N$ , from about 40 at  $V_g = 0$  to  $N = 0$  at the pinch-off voltage,  $V_g = -2.5$  V.

Figure 4.1 shows the Coulomb blockade current peaks versus  $B$  for  $N = 0$  to 18. On increasing  $V_g$ , current peaks are measured for every extra electron that enters the dot. Figure 4.1 consists of many such current traces that have been offset horizontally by a value corresponding to  $B$ . The peaks are seen to evolve in pairs for  $B < 2$  T, implying that each single-particle state is filled with two electrons of opposite spin [4]. Kinks indicate crossings between single-particle states. The dotted line marks the evolution of the  $B$ -value at which all electrons occupy spin-degenerate states belonging to the lowest orbital Landau level (i.e. this corresponds to  $\nu = 2$  in a 2DEG). As  $B$  is increased further it becomes energetically favorable for an electron to flip its spin and move to the edge of the dot (see left diagram above Fig. 4.1). States at the edge have a larger angular



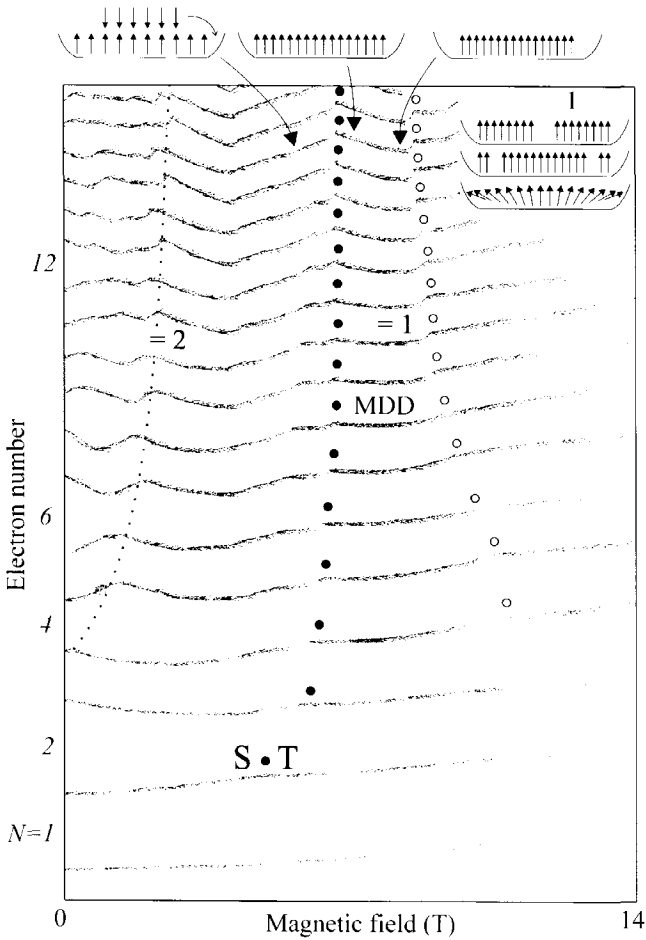


Figure 4.1: *Magnetic field evolution of the Coulomb blockade peaks for the first 18 electrons ( $V_{SD} = 100 \mu\text{V}$ ). The figure is built up of many current traces versus  $V_g$  (from  $-2.1 \text{ V}$  to  $-0.8 \text{ V}$ ) that have been offset by a value proportional to  $B$ . The solid (open) dots mark the beginning (end) of the MDD, which for  $N = 2$  is the singlet-triplet transition. The dotted line indicates filling factor  $\nu = 2$ . Top: schematic diagrams of the spin flip processes (left) and of the MDD at two  $B$ -fields (middle and right). Inset: schematic diagrams of three possible lower density droplet (LDD) states, with a hole in the center of the dot, at the edge, or a spintexture.*

momentum and a higher orbital energy. This increase is compensated by a gain in exchange energy due to the increase in the total spin and also by the reduction in direct Coulomb energy since the electrons are farther apart after the spin-flip. In this  $1 < \nu < 2$  regime, the confinement energy favors a compact electron distribution, while the direct Coulomb repulsion and exchange effects favor a diffuse occupation. As  $B$  is increased, the cost in orbital energy becomes smaller and one by one all the electrons become spin-polarized. From experimental [5] and theoretical [6, 7] studies it has become clear that self-consistency and exchange correlation are essential for quantitatively describing these spin-flip processes.

After the last spin-flip (filled circles in Fig. 4.1) all electrons are spin-polarized (i.e. the total spin  $S = N/2$ ) and the filling factor  $\nu = 1$ . Here, the  $N$  electrons occupy successive angular momentum states and the total angular momentum  $M = \frac{1}{2}N(N - 1)$ . This is the most dense, spin-polarized electron configuration allowed by the available quantum states and is therefore referred to as the maximum density droplet (MDD) [8]. Its observation was reviewed in Ref. [1]. For  $N = 2$  the spin-flip corresponds to a singlet ( $S = 0$ ) to triplet ( $S = 1$ ) transition where simultaneously  $M$  changes from 0 to 1 [9]. Also, the transitions in the  $N = 3$  to 6 traces have been identified as increases in  $S$  and  $M$  until the MDD is reached at the solid circle in Fig. 4.1 [10]. For larger  $N$  the beginning of the MDD first moves to larger  $B$  and then becomes roughly independent of  $N$ .

Once all electrons are spin-polarized (middle diagram above Fig. 4.1), the role of the exchange interaction reverses. The compact MDD state maximizes the overlap between the single-particle wavefunctions which are now occupied by electrons with parallel spins. This maximizes the gain in exchange energy, so that now exchange acts as a binding force. The direct Coulomb interaction continues to favor a diffuse occupation. When  $B$  is increased further the angular momentum states shrink in size such that the density of the MDD increases. We have pictured this in the right diagram above Fig. 4.1 as an electron droplet that does not spread out over the full available area of the confining potential. At some threshold  $B$ -value (open circles) the direct Coulomb interaction has become so large that the MDD breaks apart into a lower density droplet (LDD). Assuming that the droplet remains spin-polarized ( $S = N/2$ ) this implies that no longer all successive angular momentum states are occupied and that  $M > \frac{1}{2}N(N - 1)$ . Whether the unoccupied angular momentum states are located in the center [8] or at the edge [11] (see inset to Fig. 4.1) depends on the relative strengths of the confinement, exchange, and direct Coulomb interactions. It has also been suggested, especially when the Zeeman energy is small, that the MDD may become unstable towards the formation of a spin-texture [12]. The stability conditions for the MDD state (i.e. the  $B$ -range between solid and open circles) has been calculated in several

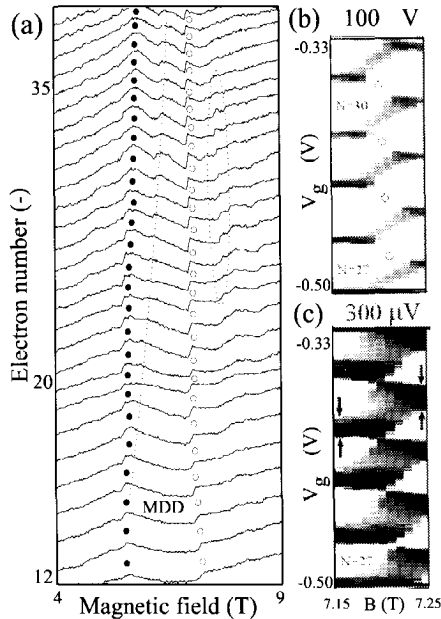


Figure 4.2: a) Peak positions versus  $B$  for  $N = 12$  to  $39$  extracted from a dataset as in Fig. 4.1 ( $V_g$  is swept from  $-0.9$  to  $-0.1$  V). Open and closed circles mark the same transitions as in Fig. 4.1. Dotted lines indicate additional steps. (b) and (c) Greyscale plots of the current versus  $V_g$  for  $B$ -values in a small interval around the step at the end of the MDD.  $V_{sd} = 100 \mu\text{V}$  in (b) and  $300 \mu\text{V}$  in (c). The arrows in (c) highlight that the peak width after the step is larger than before the step.

different theoretical approaches [7, 8, 13]. In our samples the direct Coulomb interaction is strongly screened by the electrons in the source and drain contacts. Since all theoretical works use an unscreened Coulomb interaction it is difficult to make a quantitative comparison. However, as we will now discuss, our data indicates that the MDD indeed abruptly changes into a droplet of larger area.

Fig. 4.2a shows the peak positions versus  $B$  for larger  $N$ . The kinks in the peak evolution that mark the boundaries of the MDD for small  $N$ , turn into abrupt steps for  $N \gtrsim 10$ . Within the boundaries of solid and open circles a new transition seems to develop for  $N > 15$ . This may indicate a new electronic configuration that limits the extent of the region where the MDD is the ground state. Also this transition becomes a step as  $N$  is increased. In addition, another

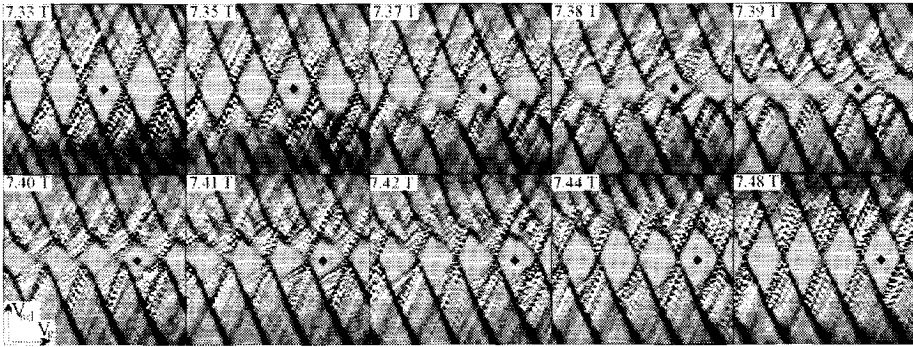


Figure 4.3: Greyscale plots of  $dI/dV_{SD}$  in the  $V_g - V_{SD}$  plane for ten  $B$ -values before, during, and after a particular step corresponding to different charge distributions ( $-1 \text{ mV} < V_{SD} < +1 \text{ mV}$  and  $-0.42 \text{ V} < V_g < -0.32 \text{ V}$ ).  $N = 31$  is marked by a solid diamond. The Coulomb blockade regions at the lowest and highest  $B$ -field have the familiar diamond shapes. In between, the Coulomb blockade regions are severely distorted. Excited state transitions are visible as dark lines [17]. As  $B$  is changed these evolve into the edges of the regular Coulomb blockade diamonds at the lowest and highest  $B$ -field.

step, marked with the dotted oval, can be discerned in Fig. 4.2a.

Fig. 4.2b and 4.2c show the current versus  $V_g$  ( $N = 27$  to  $31$ ) in greyscale for  $B$ -values around the step at the end of the MDD. For  $V_{SD} = 100 \mu\text{V}$  the peaks are much narrower than their spacings and the step width is about  $50 \text{ mT}$ . An increased source-drain voltage  $V_{SD} = 300 \mu\text{V}$  broadens the peaks. The important point is that the peak width,  $\Delta V_g$ , increases by about  $10 \%$  after crossing the step as indicated by the arrows. At low temperature  $\alpha \Delta V_g = eV_{SD}$ , where the  $\alpha$ -factor is roughly proportional to the inverse of the area of the droplet [14]. The change in peak width implies that while passing through the step the dot area changes abruptly by about  $10 \%$ .

It is clearly seen in Fig. 4.2c that the peak width during the step is about twice the width outside the step region. Other steps also show this behaviour. To study the nature of these unusual steps we have measured the excitation spectra. Fig. 4 presents  $dI/dV_{SD}$  in the  $V_{SD}-V_g$  plane for ten  $B$ -values around a particular step [15]. (In this case the step separates two LDD regions that have different charge distributions, however the same behaviour is found at all steps.) At the lowest and largest magnetic fields the Coulomb blockade regions have the

expected diamond shape. The diamond at  $B = 7.48$  T is about 10% smaller in the  $V_{SD}$  direction, indicating that the necessary energy to overcome Coulomb blockade has decreased by  $\sim 10\%$ . This is again consistent with a  $\sim 10\%$  larger dot after the charge redistribution. The shapes of the diamonds measured for  $B$  values during the step are severely distorted. The size of the Coulomb blockade region collapses here to as little as  $\sim 40\%$  of its value outside the step region. This is comparable to the peak broadening by about a factor of 2 during the steps in Fig. 4.2c where the charge distribution changed from MDD to LDD.

The distorted and collapsing Coulomb blockade regions can be explained by assuming different charge distributions [16]. In the standard model for Coulomb blockade the total energy  $U_N^{MDD}(V_g)$  belonging to the charge configuration of the MDD is described by a set of parabolas (solid parabolas in Fig. 4.4a). A transition from  $N$  to  $N+1$  is possible above a threshold voltage  $V_{SD}$  that depends linearly on  $V_g$  (solid lines and hatched regions in Fig. 4.4b). At crossings between adjacent parabolas this threshold voltage vanishes. The value of  $V_g$  where the crossing between the  $N^{th}$  and  $(N+1)^{th}$  parabolas occurs depends on the 'offset charge' of the MDD state. The total energy  $U_N^{LDD}(V_g)$  for the LDD configuration is also described by parabolas (dashed parabolas in Fig. 4.4a). However, since the LDD state has a different charge distribution, its offset charge can differ significantly from the MDD state. When  $B$  is changed the two sets of parabolas can become comparable in energy (Fig. 4.4c), such that at a particular  $V_g$ -value (open dots) the ground state of the  $N$ -electron system changes from MDD to LDD. This and the fact that transitions can occur between different charge distributions by tunneling, e.g. from  $U_N^{LDD}$  to  $U_{N+1}^{MDD}$  leads to more complex shapes of the Coulomb blockade regions (see Fig. 4.4c and d). To make a detailed comparison with this model we have replotted one dataset from Fig. 4 in Fig. 4.4f) together with a schematic representation of its main features (Fig. 4.4e). Three types of transitions can be distinguished Fig. 4.4e), which correspond to transitions between two solid parabolas (from  $U_N^{MDD}$  to  $U_{N+1}^{MDD}$ ), between two dashed parabolas (from  $U_N^{LDD}$  to  $U_{N+1}^{LDD}$ ), or between a dashed and a solid parabola (from  $U_N^{LDD}$  to  $U_{N+1}^{MDD}$ ). The first two types of transitions have the same slopes as the regular diamonds at the lowest and highest  $B$ -fields in Fig. 4 and are marked by solid and dashed lines in Fig. 4.4e). The latter transition (marked by thin lines in Fig. 4.4e) has a slope that is much smaller because the centers of the parabolas are much closer together. Note that when such a transition is made (i.e. during the step in Fig. 4.2b and 4.2c) the current is 2 to 3 times smaller than when a transition is made between two states with the same charge distribution, which implies that a transition between e.g. the MDD and the LDD has a smaller probability than a transition between two MDD states. A detailed

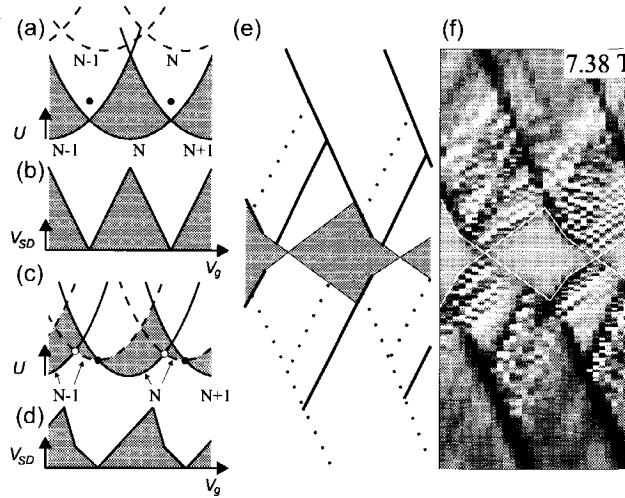


Figure 4.4: *a*) Total energy  $U(V_g)$  for two different charge distributions (solid and dashed curves, respectively). The three parabolas correspond to  $N - 1$ ,  $N$ , and  $N + 1$  electrons. Current flows when transitions can occur between parabolas of consecutive electron numbers. At low  $V_{SD}$  such transitions occur at the solid dots. In between two solid dots, the minimum  $V_{SD}$  for current is proportional to the difference in energy between the two parabolas (grey regions). *b*) Transition diagram in terms of  $V_g$  and  $V_{SD}$  (i.e. half Coulomb diamonds) corresponding to situation in *a*). *c*) same as in *a*) but at larger  $B$ . Now the dashed parabolas are comparable in energy to the solid parabolas which gives a transition of the  $N$ -electron system from MDD to LDD as  $V_g$  is varied (open dots). This leads to a different shape of the Coulomb blockade region shown in *d*). The transition diagram in *e*) shows transitions between two solid (dashed) parabolas as solid (dashed) lines, and those between a solid and a dashed parabolas as thin lines. In Fig. 4.3 the solid (dashed) lines become clearer as  $B$  is decreased (increased) and finally become the boundaries of the ordinary diamond-shaped Coulomb blockade regions at 7.33 T (7.48 T). *f*)  $dI/dV_{SD}$ -data around  $N = 31$  taken from Fig. 4.3 at 7.38 T. The edge of the Coulomb blockade regions have been emphasized with a white line.

comparison of the data in Fig. 4 with this model shows that the development of the Coulomb blockade regions as well as the excited state resonances observed in Fig. 4 is consistent with a gradual change in the relative displacement of the two sets of parabolas. From this we again conclude that the instability of the MDD is accompanied with a redistribution of charge.

We thank G. Bauer, S. Cronenwett, M. Danoesastro, M. Devoret, L. Glazman, R. van der Hage, J. Mooij, Yu. Nazarov, and S.J. Tans for experimental help and discussions. The work was supported by the Dutch Foundation for Fundamental Research on Matter (FOM).

## References

- [1] R. Ashoori, *Nature* **379**, 413 (1996).
- [2] L.P. Kouwenhoven and C.M. Marcus, *Phys. World* **11**, 35 (1998).
- [3] D.G. Austing et al., *Jap. J. Appl. Phys.* **34**, 1320 (1995), and *Semicond. Science and Technol.* **11**, 388 (1996).
- [4] S. Tarucha et al., *Phys. Rev. Lett.* **77**, 3613 (1996).
- [5] P.L. McEuen et al., *Phys. Rev. B* **45**, 11419 (1992); N.C. van der Vaart et al., *Phys. Rev. Lett.* **73**, 320 (1994); O. Klein et al., *Phys. Rev. Lett.* **74**, 785 (1995), and *Phys. Rev. B* **53**, R4221 (1996); D.G. Austing et al., submitted to *Jap. J. Appl. Phys.*, July 1998; P. Hawrylak et al., submitted to *Phys. Rev. B*, August 1998.
- [6] A.K. Evans et al., *Phys. Rev. B* **48**, 11120 (1993); J.H. Oaknin et al., *Phys. Rev. B* **49**, 5718 (1994); J.J. Palacios et al., *Phys. Rev. B* **50**, 5760 (1994); T.H. Stoof and G.E.W. Bauer, *Phys. Rev. B* **52**, 12143 (1995); A. Wojs and P. Hawrylak, *Phys. Rev. B* **56**, 13227 (1997).
- [7] M. Ferconi and G. Vignale, *Phys. Rev. B* **50**, 14722 (1994); S.R.-E. Yang et al., *Phys. Rev. Lett.* **71**, 3194 (1993); M. Ferconi and G. Vignale, *Phys. Rev. B* **56**, 12108 (1997).
- [8] A.H. MacDonald et al., *Aust. J. Phys.* **46**, 345 (1993).
- [9] M. Wagner et al., *Phys. Rev. B* **45**, 1951 (1992).
- [10] L.P. Kouwenhoven et al., *Science* **278**, 1788 (1997).
- [11] C. de C. Chamon and X.G. Wen, *Phys. Rev. B* **49**, 8227 (1994).
- [12] A. Karlhede et al., *Phys. Rev. Lett.* **77**, 2061 (1996); J.H. Oaknin et al., *Phys. Rev. B* **54**, 16850 (1996).

- [13] P.A. Maksym and T. Chakraborty, Phys. Rev. Lett. **65**, 108 (1990); J.H. Oaknin et al., Phys. Rev. Lett. **74**, 5120 (1995); Kang-Hun Ahn et al., Phys. Rev. B **52**, 13757 (1995); M. Eto, submitted to Jap. J. Appl. Phys, July 1998; A. Harju et al., Europhys. Lett. **41**, 407 (1998).
- [14] In a capacitance model  $\alpha = eC_g/C_\Sigma$ . The total capacitance  $C_\Sigma$  is in our geometry roughly proportional to the dot area, and the gate capacitance  $C_g$  increases slowly with the dot area. However, it is not clear whether an MDD state can be modelled by capacitances. For a review on quantum dots see: L.P. Kouwenhoven et al., in *Mesoscopic Electron Transport*, edited by L. Sohn et al., NATO ASI, Ser. E (Kluwer, Dordrecht, 1997). See also: <http://vortex.tn.tudelft.nl/~leok/papers/>.
- [15] An animation of the data in Fig. 4 can be found at [http://vortex.tn.tudelft.nl/~leok/MDD\\_movie/728-748.gif](http://vortex.tn.tudelft.nl/~leok/MDD_movie/728-748.gif).
- [16] S.J. Tans et al., Nature **394**, 761 (1998).
- [17] Due to the slight asymmetry between the barriers the excited state resonances lines in Fig. 4.3 are more pronounced when they run from the bottom right to the top left.



## Chapter 5

# Spectroscopy in lateral quantum dots

T.H. Oosterkamp, M. Uilenreef, Yu.V. Nazarov, S.F. Godijn,  
N.C. van der Vaart and L.P. Kouwenhoven.

### Abstract:

In this chapter we study the magnetic field evolution of the energy states in lateral rather than in vertical quantum dots. To quantify the evolution of the energy states we look at their magnetization, i.e. the derivative of the energy of a state with respect to the magnetic field. To obtain sharper resonances of the states and thereby a better energy resolution we have measured two quantum dots in series.

From such accurate measurements of the energy states in a double quantum dot we deduce the change in magnetization of the two dots due to the tunneling of a single electron. As a function of magnetic field we observe crossings and anti-crossings in the energy spectrum. The change in magnetization exhibits wiggles as a function of magnetic field with maximum values of a few effective Bohr magnetons in GaAs. These wiggles are a measure of the chaotic motion of the discrete energy states versus magnetic field. Our results show good agreement with a numeric calculation but deviate significantly from semiclassical estimates.

Orbital magnetization of small electron systems has become an important issue in the field of mesoscopics, for instance in relation to the issue of persistent currents in rings [1]. Altshuler et al. [2] have pointed out that a non-zero orbital magnetization can be present in any mesoscopic electron system, regardless the precise geometry. The point of interest is that the magnetization measures the cumulative motion of the occupied quantum states as a function of magnetic field. Generally, this motion is chaotic, except for very specific conditions of separable geometries [5]. The statistical properties of the chaotic motion are supposed to be universal in the sense that they do not depend on the details of the microscopic structure. Direct measurements of the magnetization of a mesoscopic object is a challenging task, since it requires the detection of tiny magnetic moments [3]. Here, we report on an experimental study of the magnetization of a quantum dot, by accurately measuring of its energy states. We show that semi-classical estimates can not explain our results.

We measure the energy evolution versus  $B$  of energy states near the Fermi energy  $E_F$ . The resolution is high enough that, for the first time, avoided crossings in the spectrum of a quantum dot can be resolved. We then obtain the magnetization by taking the derivative of energy with respect to  $B$ . Although this magnetization only includes contributions from states near  $E_F$ , this part largely determines the total magnetization [1]. Measurements of single-particle states versus  $B$  have previously been reported on single quantum dot devices [9, 10, 4], but have not been analyzed in terms of their magnetization. In this paper we address a *double* quantum dot system which allows for a much better energy resolution compared to single dots. From the energy dependence on  $B$  we calculate the magnetization. The advantage of our method is that the background magnetization of the whole heterostructure [12] is not measured so that we can concentrate on our mesoscopic system. As we explain below, we actually measure changes in the magnetization,  $\Delta M$ . We find that  $\Delta M$  induced by one electron tunneling between the two dots is of order one effective Bohr magneton,  $\mu_{GaAs} = e\hbar/2m_{GaAs} \simeq 0.87$  meV/T, which we determine with an accuracy of  $0.1 \mu_{GaAs}$ . The magnitude of  $\Delta M$  and the typical period of wiggles in  $\Delta M$  as a function of  $B$  are in good agreement with numerical calculations but, importantly, our results deviate from semiclassical estimates.

Figure 5.1a shows our double dot device. The metallic gates (1, 2, 3, and F) are fabricated on top of a GaAs/AlGaAs heterostructure with a 2DEG 100 nm below the surface. The 2DEG has a mobility of  $2.3 \times 10^6$  cm<sup>2</sup>/Vs and an electron density of  $1.9 \times 10^{15}$  m<sup>-2</sup> at 4.2 K. From the density and the effective mass  $m_{GaAs}^* = 0.067 m_e$ , follow the Fermi energy  $E_F = 6.9$  meV and the Fermi wave vector  $k_F = 1.1 \cdot 10^8$  m<sup>-1</sup>. Applying negative voltages to all the gates depletes

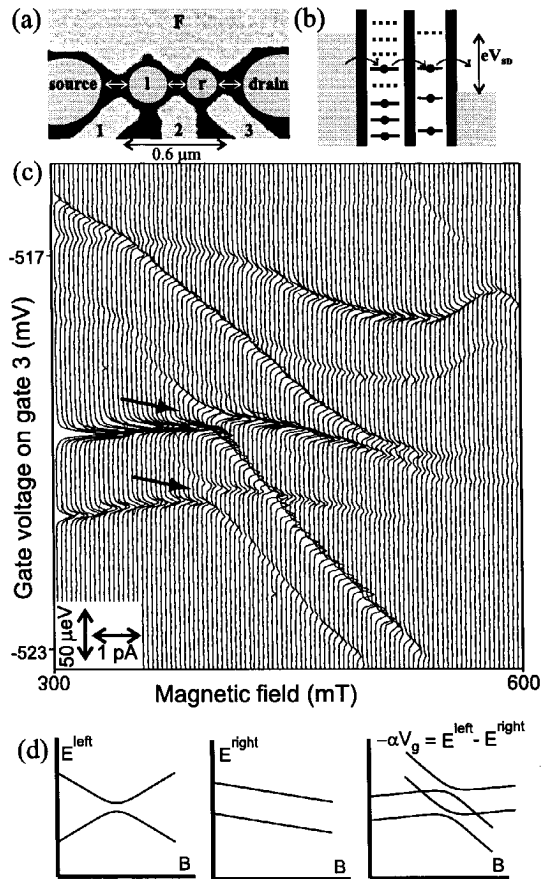


Figure 5.1: a) Geometrical layout of a double quantum dot: The gates are labeled F, 1, 2, and 3. Areas that form dots and bulk 2DEG are indicated by source, l, r, and drain. b) The energy diagram, uses black circles to indicate that a certain one-electron level is filled. Energy states at matching levels indicate that the electron can be transferred between the dots, which gives a peak in the current. Arrows illustrate the subsequent electron transfer through the system. c) Results of a typical measurement. We measure the current through the double dot sweeping the gate voltage at different magnetic fields. The curves are offset for clarity. From the leftmost to the rightmost curve, the magnetic field increases from 300 mT to 600 mT in 3 mT increments. d) The first two diagrams show how levels may evolve in each of the two dots as a function of magnetic field. When these four levels are scanned along each other by sweeping the gate voltage this will result in peak positions as sketched in the rightmost diagram.

the electron gas underneath them and forms two weakly coupled quantum dots with an estimated size of 170 nm by 170 nm for the left dot and 130 nm by 130 nm for the right dot (lithographic sizes are  $(320 \text{ nm})^2$  and  $(280 \text{ nm})^2$ ). These dots contain about 60 and 35 electrons, respectively. The sample is cooled in a dilution refrigerator to 10 mK. Noise enhances the effective electron temperature in the 2D source and drain contacts to  $\sim 80$  mK. We measure the current in response to a dc voltage  $V_{sd}$  applied between the source and drain contacts. The tunnel coupling between the dots and to the reservoirs can be controlled with the voltages on gates 1, 2 and 3. The experiments are performed in the weak coupling limit, meaning that mixing between quantum states in one dot with states in the other dot or in the leads is negligible.

In the weak coupling limit transport is governed by the physics of Coulomb blockade. We label the number of electrons in the left and right dot by  $(N_l, N_r)$ . Tunneling between two dots occurs when certain conditions for the Coulomb energies are fulfilled and when *simultaneously* a quantum state in the left dot aligns with a state in the right dot [4]. We first discuss the conditions for the Coulomb energy. A transition from the left to the right dot can occur when the Coulomb energy of having  $(N_l+1, N_r)$  exceeds the energy of  $(N_l, N_r+1)$ . To avoid transport through other charge states than  $N_l$ ,  $N_l+1$ ,  $N_r$  and  $N_r+1$ , we choose a source-drain voltage which is just smaller than the smallest of the charging energies of the individual dots. The measured charging energies are  $E_{C,left} = 1.2$  meV for the left dot and  $E_{C,right} = 1.8$  meV for the right dot. We sweep the gate voltages over small ranges and focus on a particular charging transition; i.e. transitions between  $(N_l+1, N_r)$  and  $(N_l, N_r+1)$  only. Since we discuss only one transition at a time, we can, for simplicity, leave out the Coulomb energies from the discussion and concentrate on the alignment of quantum states.

Figure 5.1b illustrates the case where a quantum state of the left dot is aligned with a quantum state in the right dot; this is a case where current can flow. In contrast to resonant tunneling in a single dot, where the peak width is determined by the thermal broadening in the leads, the width of the current resonance in the double dot is determined only by the alignment of the quantum states. The measured resonance can be an order of magnitude narrower than the thermal energy  $k_B T$  of the reservoirs [11]. We use this advantage of high energy resolution in a double dot system to obtain the magnetization with very high precision.

The quantum states (dotted and solid lines in Fig. 5.1b) we deal with are real many-body states of the dot systems. General labels for these states are  $E_i^{l, N_l}$  for the left dot and  $E_i^{r, N_r}$  for the right dot, which we simplify to  $E_i^l$  and  $E_i^r$ . When sweeping gate 3 the condition for tunneling between the lowest possible states, i.e. from ground state to ground state, is  $E_0^l = E_0^r - \alpha V_{g3}$ , where  $\alpha$  describes the

influence of gate 3 on the right level. The situation of Fig. 5.1b corresponds to tunneling from the first excited state to ground state, i.e.  $E_1^l = E_0^r - \alpha V_{g3}$ . The states  $E_i^l$  and  $E_i^r$ ,  $i = 0, 1, 2, \dots$  are separated by  $\sim 150\text{-}200 \mu\text{eV}$ .

Figure 5.1c shows a typical set of current traces for different magnetic fields while sweeping the voltage on gate 3. The bias voltage  $V_{SD} = 1.2 \text{ mV}$  such that several energy states in each dot are between the Fermi energies of the two leads. The *change* in peak positions versus  $B$  is proportional to the motion of the alignment  $\delta[E_i^l - E_i^r] = -\alpha \delta V_g^{peak}$ . (Note that if the states  $E_i^l$  and  $E_i^r$  have the same  $B$ -dependence, the peak would not change its position.) We determined the factor  $\alpha = 63 \mu\text{eV}/\text{mV}_g$  through independent measurements from which we deduced the energy scale for Fig. 5.1c that is indicated by the arrow in the lower left inset ( $\alpha$  does not change in this magnetic field range). The energy resolution of  $[E_i^l - E_i^r]$  is  $\sim 5 \mu\text{eV}$ .

The data in Fig. 5.1c contains several interesting features. First, we observe crossings between different peaks as well as anti-crossings (two are indicated by arrows). Second, pairs of peaks exhibit the same  $B$ -dependence. These are general features that we observe at many charge transitions  $(N_l, N_r)$ . We do not know of similar observations in other quantum dot experiments. Independent measurements on *one* of the individual dots also showed states evolving in pairs below  $B \sim 0.5 \text{ T}$ . The observed pairing and (anti)crossing of the peaks in the double dot experiments can then be explained as shown schematically in Fig. 5.1d. Suppose two energy states in one dot have an anti-crossing in their  $B$ -dependence. Then two paired energy states in the other dot, having the same  $B$ -dependence, will both probe this anti-crossing. At the points where two peaks actually cross two states in the left dot align with two states in the right dot simultaneously (though only one electron can tunnel at a time due to Coulomb blockade). These considerations explain our observations. The energy difference between paired states can be an exchange energy; e.g. when the higher energy state has spin zero and the lower state has spin one. In our experiments we find energy separations between paired states of typically  $100 \mu\text{eV}$  being constant within  $20 \mu\text{eV}$  over a field range of  $0.5 \text{ T}$ . Whether an exchange energy is giving rise to the energy separation is yet unclear. However, there have been other indications that exchange-correlation plays an important role in quantum dots [10, 13].

In Fig. 5.2a measurements of the current as the magnetic field is increased up to  $750 \text{ mT}$  are shown in a grayscale representation for different electron numbers  $(N_l, N_r)$ . The peak heights tend to vanish with higher magnetic fields, which limits the magnetic field range of our experiments. In Fig. 5.2b the peak positions are extracted and the gate voltage axis is converted to energy. Note that this data

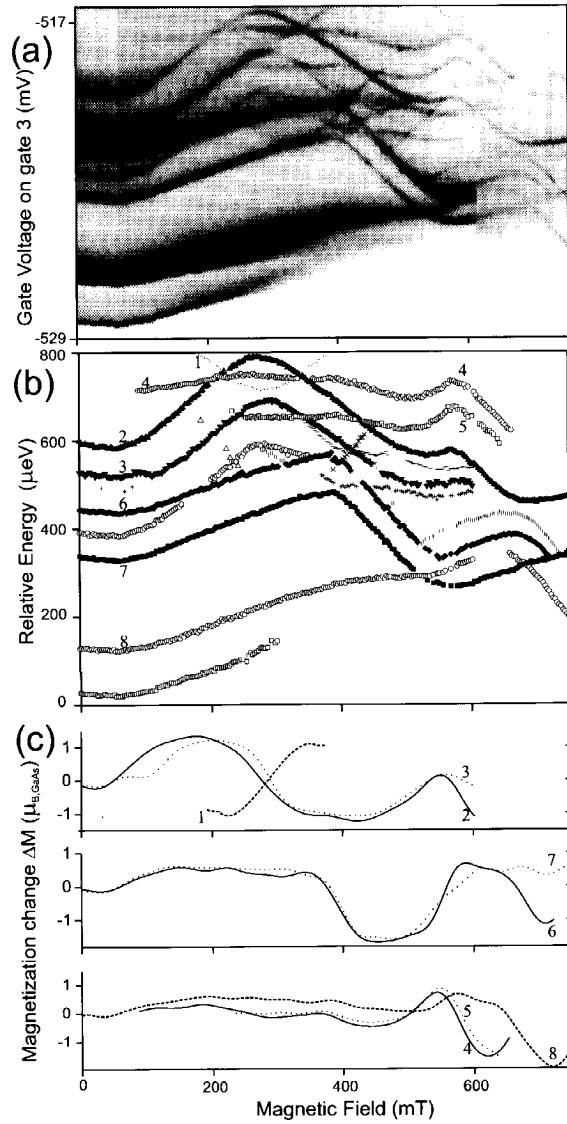


Figure 5.2: a) Grayscale representation of the current as a function of magnetic field. White is 0 fA, black is  $\geq 150$  fA. Peaks larger than 150 fA appear broader in the grey scale plot because they are truncated. b) Peakpositions converted to energy. c) Magnetization change  $\Delta M$  in units of  $\mu_{\text{GaAs}}$  as calculated from the numbered curves in b). Solid and dotted lines in one graph are taken from pairs: (2,3), (6,7) and (4,5).

also shows crossings and anti-crossings. We obtain the change in magnetization,  $\Delta M = M_{N_i+1, N_r, E_i^l} - M_{N_i, N_r+1, E_i^r}$ , by numerical differentiation:

$$\Delta M = -\frac{\delta[E_i^l - E_i^r]}{\delta B} = -\alpha \frac{\delta V_g^{peak}}{\delta B}. \quad (5.1)$$

Figure 5.2c shows examples of  $\Delta M$  in units of  $\mu_{GaAs}$  versus  $B$ , for several alignments of different discrete energy states.  $\Delta M$  shows wiggles with an amplitude of the order of  $\mu_{GaAs}$  and a typical period of 0.3 T to 0.4 T. Note that a magnetic field  $B_f$  between 0.1 and 0.2 T corresponds to one flux quantum penetrating the area of a single dot. Measurements such as those in Figures 5.1 and 5.2 were performed in three separate cooldowns and also for different electron numbers in the two dots. The magnetization at zero magnetic field is always zero due to symmetry  $E_i(B) = E_i(-B)$ . At finite magnetic fields, the sign of  $\Delta M$  can be positive as well as negative.

We can estimate the magnitude and the period of magnetization oscillations from semi-classical theory. The amplitude  $\Delta M$  is roughly the magnetic moment of one electron moving through a dot of size  $a$  with momentum  $p_F$ ,  $M_{sc} = I_{sc} \cdot S \simeq \mu_{GaAs} p_F a / 2\hbar$ , where  $I_{sc}$  is the current due to one electron encircling an area  $S$  in the dot. In our case,  $p_F a / 2\hbar \simeq 9$ , and thus  $\Delta M \simeq 9 \mu_{GaAs}$ , which is several times larger than what we observe. The characteristic period of the wiggles  $\Delta B$  can be estimated by equating magnetic energy  $\Delta M \Delta B$  with the mean spacing between particle-in-a-box states,  $\Delta E = \pi^2 \hbar^2 / 2m_{GaAs} a^2$ . This yields  $\Delta B \simeq B_f \pi \hbar / p_F a \simeq 0.02$  T, which is an order of magnitude smaller than seen in our experiment.

To comprehend this discrepancy we have performed numerical simulations. The results are plotted as solid lines in Fig. 5.3 for three different pairs of levels. We regard the dots as squares with sides of 170 and 130 nm. To lift degeneracies characteristic for the square geometry and to account for probable disorder, we add a custom random potential to the dot potential. The random potential is formed by several rectangular wells of random size and position and with a typical depth of  $\sim 0.1 E_F$ . Solving the Schrödinger equation we have calculated the energy levels in both dots versus  $B$ . From the difference of the magnetization of states close to the Fermi level in each of the two dots we obtain  $\Delta M$ . We have checked that the wiggles of the magnetization change are random depending on the realization of the potential. They do retain the same order of magnitude and the same typical period. To illustrate that the numerical results show a better agreement with the experimental data than the semiclassical estimate as far as the amplitude and the wiggle period is concerned, we have plotted magnetization measurements from Fig. 5.1 (squares and diamonds) and yet another data set (circles) that happen to fit the calculations reasonably well, even though, due to

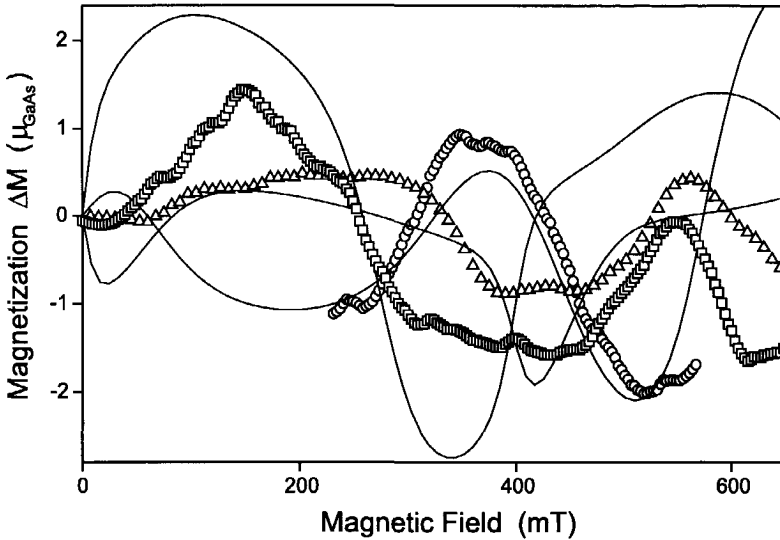


Figure 5.3: Magnetization change calculated numerically for two dots of the same sizes as in the experiment (solid lines) and experimental curves extracted from Fig. 5.1 (squares and triangles) and another dataset (circles).

the random nature of the disorder, an exact fit is not expected.

For larger electron numbers ( $N > 200$ ) our simulations begin to show agreement with the semi-classical estimates. This drives us to the conclusion that quantum dots with  $N < 100$  are too small to be satisfactorily described by semi-classical theory.

In conclusion, we used a new method to explore magnetic properties of an ultra small system by means of an accurate transport measurement. The high resolution in energy made it possible to observe clear avoided crossings of states. For the magnetization an accuracy of  $\sim 0.1 \mu_{\text{GaAs}}$  was achieved. Magnetization traces manifest the chaotic motion of energy levels in magnetic field. The system appears to be too small for this motion to be described by semi-classical theory. There is, however, good agreement with the results of numerical simulations that incorporate the microscopic description of the dot.

We thank Philips Laboratories and C. T. Foxon for providing the heterostructures and S. Cronenwett, C. Harmans, J. E. Mooij, C. W. J. Beenakker, M. Büttiker, G. Blatter, and A. I. Larkin for very instructive discussions. The work was supported by the Dutch Foundation for Fundamental Research on Matter



(FOM) and L.P.K. by the Royal Netherlands Academy of Arts and Sciences (KNAW).

## References

- [1] Y. Imry, in *Introduction to mesoscopic physics* (Oxford 1997).
- [2] B.L. Altshuler et al., Phys. Rev. Lett **66**, 88 (1991).
- [3] L. P. Lévy et al., Phys. Rev. Lett. **64**, 2074 (1990). V. Chandrasekar et al., Phys. Rev. Lett. **67**, 3578 (1991). D. Maily et al., Phys. Rev. Lett. **70**, 2020 (1993). L. P. Lévy et al., Physica B **189**, 204 (1994).
- [4] See for a review on quantum dots: L.P. Kouwenhoven et al., in *Mesoscopic Electron Transport*, edited by L. Sohn et al. (Kluwer Series E, 1997). See also <http://vortex.tn.tudelft.nl/mensen/leok/papers/>
- [5] F. Haake, *Quantum Signatures of Chaos* (Springer, Berlin 1992).
- [6] C.W.J. Beenakker, Rev. Mod. Phys. **69**, 731 (1997).
- [7] A.M. Chang et al. Phys. Rev. Lett. **76**, 1695 (1996). J.A. Folk et al., Phys. Rev. Lett. **76**, 1699 (1996).
- [8] U. Sivan et al., Phys. Rev. Lett. **77**, 1123 (1996). S. Patel et al., Superlattices and Microstructures **21**, 43 (1997) and cond-mat/9708090. F. Simmel et al., Europhys. Lett. **38**, 123 (1997).
- [9] Bo Su et al., Phys. Rev. B **65**, 7644 (1992). A.T. Johnson et al., Phys. Rev. Lett. **69**, 1592 (1992).
- [10] S. Tarucha et al., Phys. Rev. Lett. **77**, 3613 (1996). D.R. Stewart et al., Science **278**, 1784 (1997). L.P. Kouwenhoven et al., Science **278**, 1788 (1997).
- [11] N. C. van der Vaart et al., Phys. Rev. Lett. **74**, 4702 (1995).
- [12] S.A.J. Wiegers et al., Phys. Rev. Lett. **79**, 3238 (1997).
- [13] M. Stopa, cond-mat/9709119.



## Chapter 6

# Photon assisted tunneling in a single quantum dot

T.H. Oosterkamp, L.P. Kouwenhoven, A.E.A. Koolen,  
N.C. van der Vaart and C.J.P.M. Harmans.

### Abstract:

We have measured photon-assisted tunneling through a quantum dot with zero dimensional (0D) states. For photon energies smaller than the separation between 0D-states we observe photon sideband resonances of the ground state. When the photon energy exceeds the separation between 0D-states, we observe photon induced excited state resonances. We identify the different resonances by studying their dependence on photon frequency, magnetic field and microwave power.

## 6.1 Introduction

In analogy to spectroscopy on atoms it is interesting to study the interaction between light and electrons confined in quantum dots. However, since it is difficult to realize identical quantum dots the response of an ensemble of quantum dots to light excitation is strongly averaged over sample differences. Despite this averaging, excitation studies on quantum dot arrays by far-infrared light have shown the spectrum of collective modes [1] and inelastic light scattering experiments have probed single particle excitations [2]. The latter technique has also probed excitons in a single quantum dot [3]. We have used microwaves with relatively low frequency (up to 75 GHz) to study the discrete electron excitation spectrum in the conduction band of a single quantum dot. In contrast to the light transmission or luminescence measurements of the above spectroscopy techniques, we measure the photoresponse in the dc current.

Current can flow through a quantum dot when a discrete energy state is aligned to the Fermi energies of the leads. This current is carried by resonant elastic tunneling of electrons between the leads and the dot. An additional time-varying potential  $\tilde{V} \cos(2\pi ft)$  can induce *inelastic* tunnel events when electrons exchange photons of energy  $hf$  with the oscillating field. This inelastic tunneling with discrete energy exchange is known as photon-assisted tunneling (PAT). PAT has been studied before in superconductor-insulator-superconductor tunnel junctions [4], in superlattices [6], and in quantum dots [7, 9]. The quantum dots in Ref. 7 were rather large and effectively had a continuous density of states. So far, PAT through small quantum dots with discrete states has only been studied theoretically [10, 11]. In this paper we show for the first time different types of PAT processes through a quantum dot with well resolved discrete 0D-states. We first show that an elastic resonant tunneling peak in the current develops photon sideband resonances when we apply microwaves. We then use PAT as a spectroscopic tool to measure the energy evolution of the first excited state as a function of magnetic field [12].

## 6.2 PAT through a single junction

Our first step is to look at photon-assisted transport through a single tunnel junction. Suppose that we have an oscillating potential difference across a tunnel junction  $\tilde{V} \cos(2\pi ft)$ : in which  $\tilde{V}$  is the ac amplitude and  $f$  is the frequency. This gives a Hamiltonian  $H = H_0 + H_{int} = H_0 + e\tilde{V} \cos(2\pi ft)$ .  $H_0$  is the unperturbed Hamiltonian describing the two leads on either side of the tunnel junction. The effect of the oscillating potential is that the time dependent part

of the electron wave function, when expanded into a power series, contains the energy components  $E$ ,  $E \pm hf$ ,  $E \pm 2hf$ , ..., etc. where  $hf$  is the photon energy. These energy components are called sidebands. The expansion can be done as [4]:

$$\begin{aligned}
 \psi(r, t) &= \varphi(r) \exp\left(-i \int dt [E + e\tilde{V} \cos(2\pi ft)]/\hbar\right) \\
 &= \varphi(r) \exp(-iEt/\hbar) \sum_{n=-\infty}^{\infty} J_n(e\tilde{V}/hf) \exp(-in2\pi ft) \\
 &= \varphi(r) \left( \sum_{n=-\infty}^{\infty} J_n(e\tilde{V}/hf) \exp(-i[E + nhf]t/\hbar) \right) \quad (6.1)
 \end{aligned}$$

$\varphi(r)$  is the space dependent part of the wave function  $\psi(r, t)$ .  $J_n(\alpha)$  is the  $n$ th order Bessel function of the first kind evaluated at  $\alpha = e\tilde{V}/hf$ . The sidebands are only well-defined if the number of tunnel events per unit of time (i.e. the tunnel rates) are much smaller than the photon-frequency. Because there is no electric field in the scattering-free leads, mixing of electron states in the leads is absent [5]. The probability for tunneling from an occupied state  $E$  to an unoccupied state  $E + nhf$  is given by  $P(E \rightarrow E + nhf) = J_n^2(\alpha)$ . A positive (negative)  $n$  corresponds to the absorption (emission) of  $n$  photons during the tunnel process. Elastic tunneling without photons corresponds to  $n = 0$ .

A net current flows by introducing an asymmetry, for instance, by applying a dc source-drain voltage  $V_{SD}$  between the two leads. If tunneling is a weak perturbation, the current in the presence of microwaves  $\tilde{I}$  is given by [4]:

$$\begin{aligned}
 \tilde{I}(V_{SD}) &= c \sum_{n=-\infty}^{\infty} J_n^2(e\tilde{V}/hf) \\
 &\quad \times \int_{-\infty}^{\infty} dE [f_l(E - eV_{SD}) - f_r(E + nhf)] \rho_l(E - eV_{SD}) \rho_r(E + nhf) \\
 &= \sum_{n=-\infty}^{\infty} J_n^2(e\tilde{V}/hf) I(V_{SD} + nhf/e) \quad (6.2)
 \end{aligned}$$

$f(E)$  is the Fermi function,  $\rho_l$  and  $\rho_r$  are the unperturbed densities of states of the two leads,  $c$  is a constant which is proportional to the tunnel conductance, and  $I$  is the tunnel current without an oscillating field. For a *single* junction the dc current in the presence of microwaves is thus simply described in terms of the dc current without microwaves. Note that for a *double* junction equation 6.2 is not valid, as will be shown in the following.

### 6.3 The 0D-model based on a master equation

Transport through a quantum dot is dominated by Coulomb blockade effects [13]. The energy to add an extra electron to a quantum dot consists of a charging energy  $E_c$  for a single electron, and a finite energy difference  $\Delta\varepsilon$  arising from the confinement. A dot is said to have 0D-states if  $\Delta\varepsilon$  is larger than the thermal energy  $k_B T$  [13]. Assuming sequential tunneling of single electrons, the current can be calculated with a master equation [14, 15].

Our model is based on such a master equation approach with the inclusion of PAT. We assume  $E_c \gg \Delta\varepsilon$ ,  $k_B T$ ,  $hf$  such that we can use a two-state ( $N$  and  $N + 1$ ) model [16]. We neglect level broadening due to a finite lifetime of the electrons on the dot. A quantum dot state can be described by the total number of electrons on the dot (which is either  $N$  or  $N + 1$ ) together with  $\chi$  which describes the particular distribution of electrons over the 0D-states. The net current through the dot  $I$  follows from the probability  $P_{N,\chi}$  that a particular distribution is occupied together with the tunnel rates through one of the barriers:

$$I = \sum_{\chi} \sum_{j=\text{empty}} P_{N,\chi} \Gamma_{l,j}^{\text{in}} - \sum_{\chi'} \sum_{j=\text{full}} P_{N+1,\chi'} \Gamma_{l,j}^{\text{out}} \quad (6.3)$$

Here  $\Gamma_{l,j}^{\text{in(out)}}$  are the rates into (or out of) 0D-state  $j$ , through the left barrier:

$$\begin{aligned} \Gamma_{l,j}^{\text{in}}(\varepsilon_j) &= \Gamma_l \sum_n J_n^2(\alpha_l) f_l(\varepsilon_j - nhf + eV_{SD}) \\ \Gamma_{l,j}^{\text{out}}(\varepsilon_j) &= \Gamma_l \sum_n J_n^2(\alpha_l) [1 - f_l(\varepsilon_j - nhf + eV_{SD})] \end{aligned} \quad (6.4a)$$

where  $\Gamma_l$  is the tunnel rate of the left barrier determined by the barrier shape that we assume to be energy independent, and  $\varepsilon_j$  is the energy of 0D-state  $j$  measured relative to the Fermi energy of the right lead. An equivalent set of equations can be given for the right barrier taking  $V_{SD} = 0$ . In the following simulations we take equal ac amplitudes dropping across the left and right barriers; i.e.  $\alpha_l = \alpha_r = \alpha$ . The probabilities  $P_{N,\chi}$  are calculated from the set of master equations given by:

$$\begin{aligned} \dot{P}_{N,\chi} &= \sum_{\chi'} P_{N+1,\chi'} (\Gamma_{l,j_{\chi'}}^{\text{out}} + \Gamma_{r,j_{\chi'}}^{\text{out}}) \\ &\quad - P_{N,\chi} \sum_{j=\text{empty}} (\Gamma_{l,j}^{\text{in}} + \Gamma_{r,j}^{\text{in}}) \\ &\quad + \sum_{\chi'' \neq \chi} P_{N,\chi''} \Gamma_{\chi'' \rightarrow \chi} - P_{N,\chi} \sum_{\chi''' \neq \chi} \Gamma_{\chi \rightarrow \chi'''} \end{aligned} \quad (6.5)$$

and its equivalent for  $\dot{P}_{N+1,\chi'}$ . Note that for  $N = 2$  we have ten different  $\chi$  if we include five different 0D-states, so we have ten equations  $\dot{P}_{N,\chi}$ , and another ten equations  $\dot{P}_{N+1,\chi'}$ . The first two terms in equation (6.5) correspond to a change in the occupation probability of a certain distribution due to tunneling (the number of electrons on the dots changes). In the first term only the rates are taken into account that correspond to an electron tunneling out of state  $j_{\chi'}$  leaving the dot in the distribution  $(N, \chi)$ . For an electron tunneling out of the dot one needs to sum over all the states  $j$  that are filled when the dot is in state  $\chi$  (second term). In the last two terms the number of electrons on the dot stays the same, only the distribution over the states changes (i.e. electrons relax to a lower level or they are excited to a higher level. We take excitation rates equal to zero (no mixing of electron states in the dot due to the high frequency) and non-zero relaxation rates.

To find a stationary solution for the occupation probabilities in the dot these equations are set to zero and solved with the boundary condition:

$$\sum_{\chi} P_{N,\chi} + \sum_{\chi'} P_{N+1,\chi'} = 1 \quad (6.6)$$

The current is calculated for a fixed set of 0D-energies  $\{\varepsilon_j\}$ . The effect of a gate voltage is simulated by shifting the 0D-energies relative to the Fermi energy of the right reservoir.

Figure 6.1 shows simulations without relaxation between the states in the dot. We have taken  $\Delta\varepsilon = 3hf$  for the curves in the inset. Next to the main resonance we see that side-peaks develop at multiple values of  $hf/e$  when  $\alpha$  is increased. In the main figure we have taken  $\Delta\varepsilon = 0.75hf$ . Here not only side-peaks develop but we also see peaks at other gate voltages. These peaks arise due to the interplay between the 0D-states and the photon energy. Their locations are described by  $(m\Delta\varepsilon + nhf)/e$  where  $m = 0, \pm 1, \pm 2, \dots$  and  $n$  is the photon number. Similar simulation results have been reported by Bruder and Schoeller [11].

Figure 6.2 shows an expansion for the curve with  $\alpha = 1$ . We have assigned the excited states and the particular PAT process. The  $N + 1$  ground state is denoted by  $j = 0$ , positive  $j$ 's are excited states above  $\varepsilon_0$  and negative  $j$ 's are below  $\varepsilon_0$ .

The inset shows the effects of relaxation. It is seen that upon increasing the relaxation rate the peaks that correspond to transitions through excited states decrease, while the peaks corresponding to transitions through the ground state increase.

The diagrams in Fig. 6.3 show two relevant energy states for  $N$  electrons in the dot. For small dc bias voltage and no ac voltages a current resonance occurs

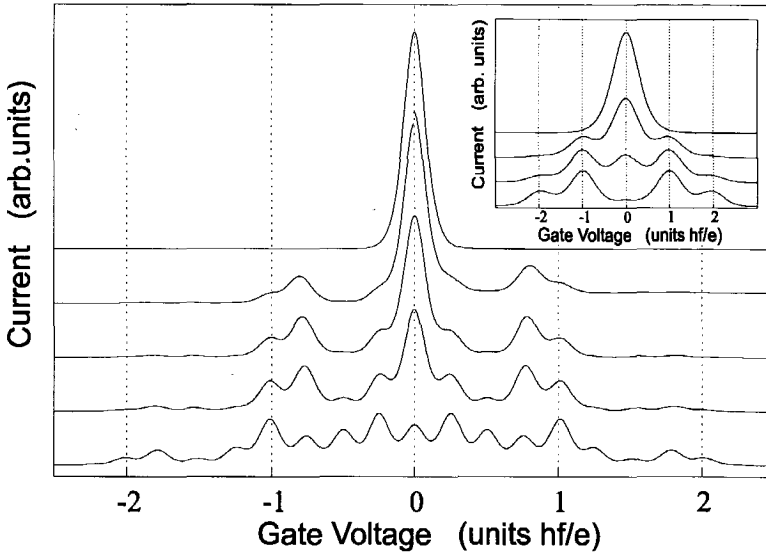


Figure 6.1: *Simulation without relaxation.* The parameters for the data in the inset are  $\Delta\varepsilon = 3hf$ ,  $hf = 5k_B T$ , and from top to bottom  $\alpha = 0, 1, 1.5, 2$ . The parameters for the main figure are  $\Delta\varepsilon = 0.75hf$ ,  $hf = 20k_B T$  and from top to bottom  $\alpha = 0, 0.5, 0.75, 1, 1.5$ .

when the topmost energy state (i.e. the electrochemical potential) of the quantum dot lines up with the Fermi levels of the leads (see the diagram  $\varepsilon_0$ ). When high frequency voltages drop across the two barriers, additional current peaks appear. We distinguish two mechanisms which were calculated in Ref. 11. The first mechanism gives photon induced current peaks when the *separation* between the ground state  $\varepsilon_0$  and the Fermi levels of the leads *matches* the photon energy (or  $nhf$ ), as depicted in the diagrams labeled by  $\varepsilon_0 + hf$  and  $\varepsilon_0 - hf$ . The minus and plus signs correspond to being before or beyond the main resonance. Note that also the case of  $\varepsilon_0 - hf$  involves photon absorption. Following the literature on the tunneling time we call these current peaks: *sidebands* [18]. The second mechanism leads to photon peaks when an excited state is in resonance with the Fermi levels of the leads (see diagram  $\varepsilon_1$ ). Without PAT, transport through the excited state  $\varepsilon_1$  is blocked since Coulomb blockade prevents having electrons in both the ground state and the excited state simultaneously. The electron in the ground state cannot escape from the dot because its energy is lower than the Fermi levels in the leads. PAT, however, empties the ground state  $\varepsilon_0$  when the



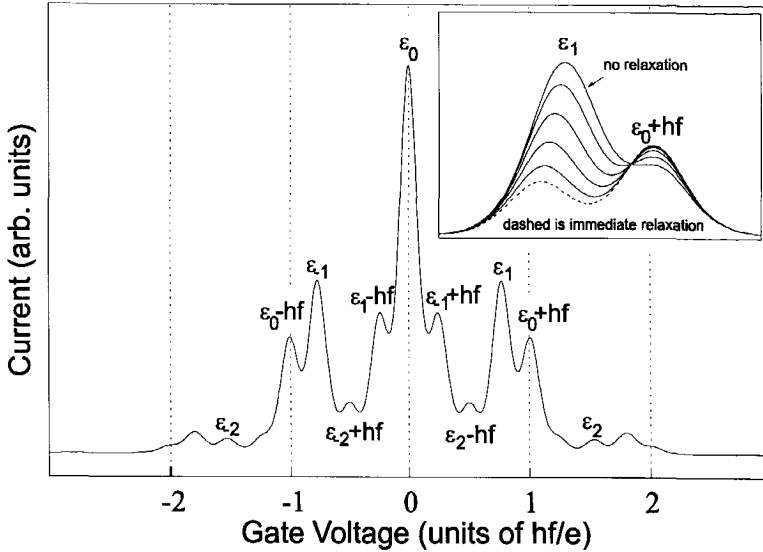


Figure 6.2: Expansion for the curve  $\alpha = 1$  from figure 6.1. The inset shows the effects of increasing relaxation. The relaxation rates divided by the tunnel rate are 0, 0.1, 0.35, 1, 3.5, and infinite.

electron in  $\varepsilon_0$  absorbs enough energy and leaves the dot. This process is analogous to photo ionization. Now, the  $N^{\text{th}}$  electron can tunnel resonantly via the excited state  $\varepsilon_1$  as long as the state  $\varepsilon_0$  stays empty. Note that for this second mechanism  $nhf$  has to *exceed*, but not necessarily *match* the energy splitting  $\Delta\varepsilon = \varepsilon_1 - \varepsilon_0$ . More photon peaks are generated when these two mechanisms are combined as in the diagrams labeled by  $\varepsilon_1 + hf$  and  $\varepsilon_1 - hf$ . We thus see that PAT can populate the excited states with the help of tunneling between dot and leads. So, even without direct intra-dot transitions we can perform photon spectroscopy on discrete quantum dot states.

## 6.4 Pumped current

It is important to note that in the diagrams of Fig. 6.3 only processes with tunneling from or to states close to the Fermi levels in the leads contribute to the net current. Tunnel processes that start with an electron from further below the Fermi level in one of the leads are cancelled by an electron from the other lead. This is only true when the ac voltage drop is the same for each barrier.

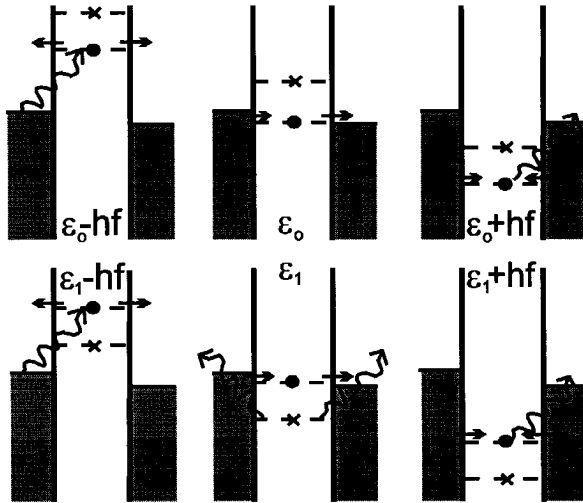


Figure 6.3: Diagrams depicting the sequence of tunneling events which dominantly contribute to the current through a quantum dot, for different gate voltages. A small dc bias raises the left Fermi level with respect to the right Fermi level.  $\varepsilon_0$  and  $\varepsilon_1$  denote the ground state and the first excited state of the  $N$  electron system. When the  $N^{\text{th}}$  electron tunnels to one of the two reservoirs, the energy states of the dot drop by the charging energy  $E_c$ . The corresponding diagrams for  $N - 1$  electrons are not shown. Note that only processes with tunneling from or to states close to the Fermi levels in the leads contribute to the net current.

When the ac voltage drops across the two barriers are unequal the dot acts as an electron pump[7, 11]. The resulting pumped current makes the current resonances discussed above less clear. For this reason we discuss this pumping mechanism in more detail here before proceeding further. Fig. 6.4 shows a calculation of the pumped current as a function of the gate voltage that occurs when the ac voltage drop over one barrier is 5% smaller than over the other barrier. We have taken zero dc bias voltage. To illustrate the origin of the pumped current the insets show the extreme case, when all the ac voltage drop is across the left barrier. In this case photon absorption occurs only at the left barrier. At negative gate voltage when the ground state level of the dot is *above* the Fermi level of the leads an electron can *enter* the dot from the left lead only (bottom left inset of Fig. 6.4). Once the electron is in the dot it can tunnel out through both of the tunnelbarriers. Only the electron tunneling out to the right lead contributes to

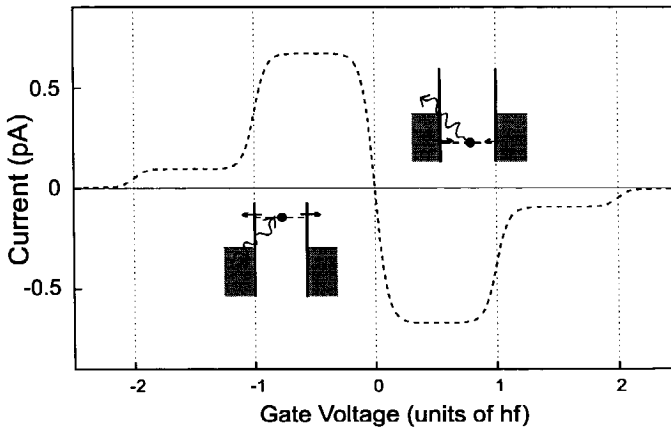


Figure 6.4: Calculation of the current as a function of gate voltage in the case where the ac voltage drop over one barrier is 5% smaller than over the other barrier.  $V = 0$ ,  $k_B T = 0.05 h f$ ,  $\Gamma = 5 \cdot 10^8 \text{ s}^{-1}$ . The insets depict which sequence of tunneling events is responsible for the pumped current when the ground state of the quantum dot is below or above the Fermi levels of the leads.

the net current. Therefore the net current is to the right. When the ground state level of the dot is *below* the Fermi level of the leads, however, an electron can only *leave* the dot to the left lead (upper right inset of Fig. 6.4). The dot can be filled from either lead once it is emptied. This time only the electron tunneling *in* from the right lead contributes to the net current. Therefore there is a net current to the left. The difference between these two situations is the shift in the ground state energy with respect to the Fermi levels of the leads. So, when the gate voltage is swept such that the ground state moves through the Fermi levels of the leads, the pumped current changes sign. The pumped current occurs over a width which scales with the photon energy. The extra shoulders at the far left and far right of the figure are due to two-photon processes.

## 6.5 Experiments

Our measurements are performed on a quantum dot defined by metallic gates (see Fig. 6.5) in a GaAs/AlGaAs heterostructure containing a 2 dimensional electron gas (2DEG) 100 nm below the surface. The 2DEG has mobility  $2.3 \cdot 10^6 \text{ cm}^2/\text{Vs}$  and electron density  $1.9 \cdot 10^{15} \text{ m}^{-2}$  at 4.2 K. By applying negative voltages

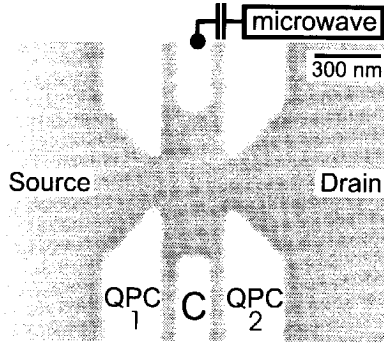


Figure 6.5: SEM photo of the sample. The lithographic size of the dot is  $(600 \times 300) \text{ nm}^2$ . Current can flow when we apply a voltage between source and drain. The microwave signal is coupled to one of the center gates.

to the two outer pairs of gates, we form two quantum point contacts (QPCs). An additional pair of center gates between the QPCs confines the electron gas to a small dot. No electron transport is possible through the narrow channels between the center gates and the gates forming the QPCs. The center gate voltage  $V_g$  can shift the states in the dot with respect to the Fermi levels of the leads and thereby controls the number of electrons in the dot. The energy shift is given by  $\Delta E = \kappa \cdot \Delta V_g$ . A small dc voltage bias is applied between source and drain and the resulting dc source-drain current is measured. From standard dc measurements we find that the effective electron temperature is approximately  $T = 200 \text{ mK}$  and the charging energy  $E_c = 1.2 \pm 0.1 \text{ meV}$ . We independently determine the level splitting  $\Delta \epsilon$  for different magnetic fields from current-voltage characteristics. In addition to the dc gate voltages we couple a microwave signal (10-75 GHz) capacitively into one of the center gates. The microwave will not couple in the same way to the dot as to the leads, which results in an ac voltage drop over both barriers.

### 6.5.1 pumping

In the following we first present some experimental results with a strongly pumped current. Then we discuss the measurements on the photon resonances. Fig. 6.6 shows measurements of the current at  $B = 1.96 \text{ T}$  for three frequencies

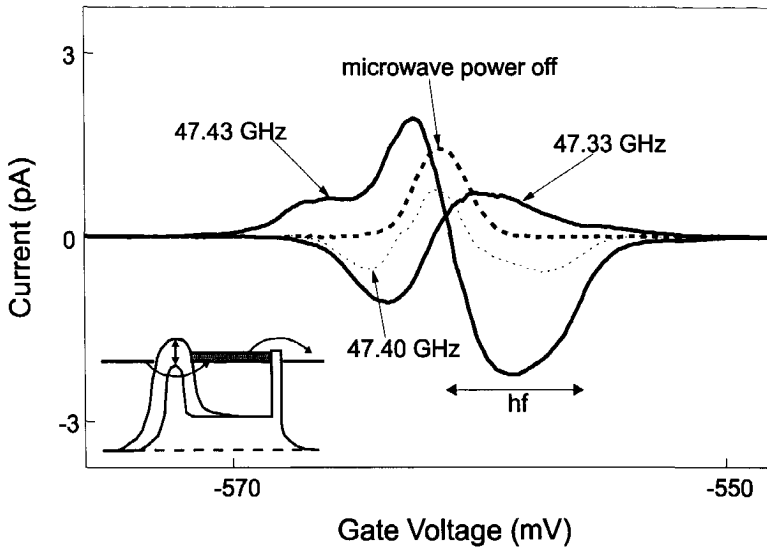


Figure 6.6: *Measurements of the pumped current at  $B = 1.96$  T,  $V_{SD} = 13$   $\mu$ V, and for frequencies around 47.4 GHz. Dashed line is without microwaves. The dotted line shows the smallest asymmetry, but shows evidence for a pumping mechanism which is not included in our model.*

around 47.4 GHz (the arrow denotes  $hf$ ). The dashed line is the current without microwaves. All curves are taken with a bias voltage of  $V_{SD} = 13$   $\mu$ V. It can be seen that for the lowest frequency the current is pumped in one direction whereas for the highest frequency it is pumped in the opposite direction, meaning that while at 47.33 GHz the left barrier has the *smaller* ac voltage drop, at 47.43 GHz the left barrier has the *larger* ac voltage drop. This illustrates how sensitively the asymmetry of the voltage drops over the two barriers depends on the frequency. This sensitivity is ascribed to the standing waves in the sample holder. The dotted line shows the current measured at an intermediate frequency, where we expect the ac voltage drop to be equal over both barriers. In contrast to the two solid curves, the dotted line is lower than the dashed line without microwaves over the whole gate voltage range. This cannot be explained by the pumping mechanism in our model. Our model only includes the oscillation of the potential of the leads and the dots which always results in a pumped current which changes sign at the resonance. This pumped current which is negative over the whole gate voltage range is attributed to the effect of the microwaves on the barrier height. The inset shows how a quantum dot can act as a pump when one tunnelbarrier

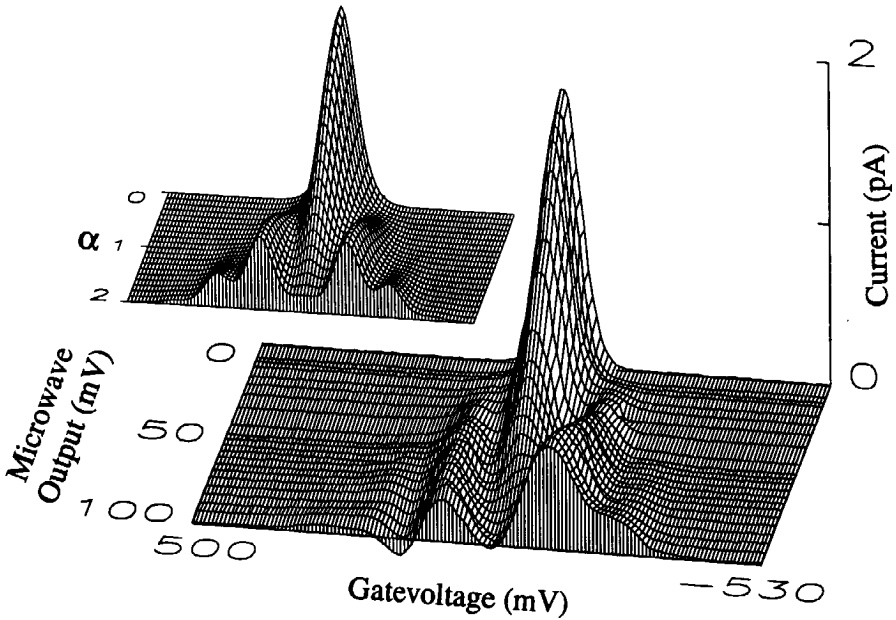


Figure 6.7: Measurement of the current through the quantum dot as a function of the center gate voltage and the output voltage of the microwave supply. These data are taken in the single level regime ( $hf < \Delta\varepsilon$ ).  $hf = 110 \mu\text{eV}$  for  $f = 27 \text{ GHz}$ ,  $\Delta\varepsilon = 165 \mu\text{eV}$  at  $B = 0.84 \text{ T}$ , and  $V_{SD} = 13 \mu\text{V}$ . Note that the gate voltage axis runs from positive to negative. Inset: calculation of the current as a function of the gate voltage and the ac voltage parameter  $\alpha = e\tilde{V}/hf$ , taking the same values for  $T$ ,  $f$ , and  $V$  as in the experiment.

is periodically modulated in height. During one part of the cycle when the left barrier is low electrons enter the dot ( $\Gamma_L^{low} > \Gamma_R$ ) while they escape the dot through the right barrier in the second half of the cycle when the left barrier is high ( $\Gamma_L^{high} < \Gamma_R$ ). This essentially is a classical mechanism that has been verified experimentally in the MHz regime [8].

For observing photon resonances we choose frequencies that do not lead to a dc current in the absence of a dc bias voltage, in order to minimize both types of pumping. It is then easier to distinguish the photon resonances. We concentrate on a single Coulomb peak and study the modification of the shape of the peak induced by the microwave signal [?].

### 6.5.2 low frequency regime $hf < \Delta\varepsilon$

First, we study the photon sidebands of the ground state at a magnetic field  $B = 0.84$  T [19]. The main part of Fig. 6.7 shows measured curves of the current as a function of the gate voltage at different microwave powers for the case  $hf < \Delta\varepsilon$  ( $hf = 110$   $\mu\text{eV}$  for  $f = 27$  GHz and  $\Delta\varepsilon = 165$   $\mu\text{eV}$ ). Here current flows primarily via the ground state and its photon sidebands (i.e. upper diagrams in Fig. 6.3). On increasing the microwave power we see in Fig. 6.7 that the height of the main resonance decreases to zero while additional resonances develop with increasing amplitude. When we convert gate voltage to energy we find that the additional resonances are located at  $\varepsilon_0 \pm hf$  and  $\varepsilon_0 \pm 2hf$  [20]. The power dependence is in agreement with the behaviour of the Bessel functions:  $J_0^2(\alpha)$  for the main resonance  $\varepsilon_0$ ,  $J_1^2(\alpha)$  for the one-photon sidebands  $\varepsilon_0 \pm hf$ , and  $J_2^2(\alpha)$  for the two-photon sidebands  $\varepsilon_0 \pm 2hf$ . For comparison we show a calculation in the inset of Fig. 6.7 for the same values for the temperature, frequency and bias voltage as in the experiment. We have assumed equal ac voltages across the two barriers. The small difference between measured and calculated data is attributed to an asymmetry in the ac coupling.

### 6.5.3 high frequency regime $hf > \Delta\varepsilon$

We now discuss the higher frequency regime where  $hf > \Delta\varepsilon$  such that PAT can induce current through excited states. Fig. 6.8 shows measurements of the current at  $B = 0.91$  T (here  $\Delta\varepsilon = 130$   $\mu\text{eV}$ ). In the top section  $f = 61.5$  GHz and in the bottom section  $f = 42$  GHz. As we increase the power we see extra peaks coming up. We label the peaks as in Fig. 6.3. On the right side of the main resonance a new resonance appears, which we assign to photo ionization followed by tunneling through the first excited state. At higher powers the one-photon sidebands of the main resonance as well as those of the excited state resonance appear. We do not observe the peak for  $\varepsilon_0 + hf$ , in this measurement. This can be explained, at least in part, by the fact that here an electron can also tunnel into  $\varepsilon_1$  which blocks the photon current through  $\varepsilon_0 + hf$ . Simulations confirm that the peak for  $\varepsilon_0 + hf$  can be several times weaker than the peak for  $\varepsilon_0 - hf$  [17]. Also it is masked by the high peak for  $\varepsilon_1$  right next to it. The arrows underneath the curves mark the photon energy given by the corresponding frequency. The peaks  $\varepsilon_0$  and  $\varepsilon_1$  remain in place when we change the frequency, since the photon energy evidently does not alter the energy splitting. The other peaks,  $\varepsilon_0 - hf$  and  $\varepsilon_1 \pm hf$ , shift by an amount that corresponds to the change in photon energy as indicated by the arrows. This reflects that the sidebands originate from matching

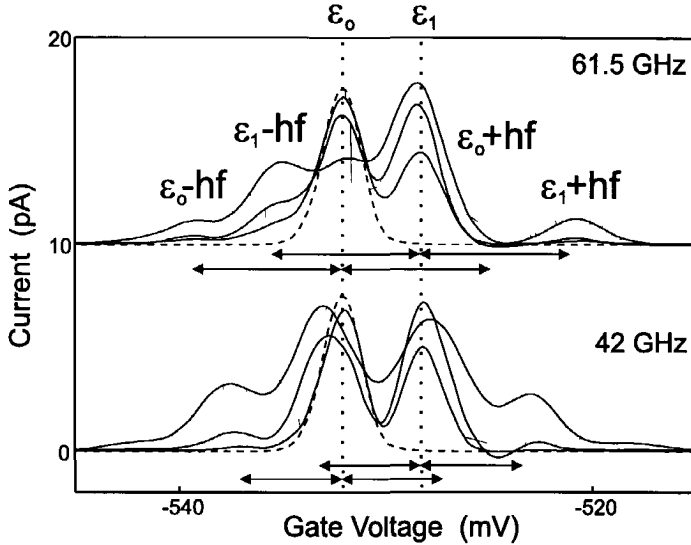


Figure 6.8: Measured current as a function of center gate voltage for different microwave powers. The dashed curve is without microwaves.  $B = 0.91$  T,  $V_{SD} = 13$   $\mu$ V, in the top section the frequency is  $f = 61.5$  GHz, in the bottom section  $f = 42$  GHz. As the frequency of the microwaves is reduced between top and bottom sections, the ground state resonance  $\varepsilon_0$  and the resonance attributed to the excited state  $\varepsilon_1$  remain at the same gate voltage position. The other peaks,  $\varepsilon_0 - hf$  and  $\varepsilon_1 \pm hf$ , shift inward by an amount which corresponds to the change in photon energy as indicated by the arrows. We do not observe  $\varepsilon_0 + hf$  in this measurement.

the states  $\varepsilon_0$  and  $\varepsilon_1$  to the Fermi levels of the leads by a photon energy  $hf$ .

We further substantiate the peak assignment by studying detailed frequency, magnetic field and power dependence.

#### 6.5.4 frequency dependence

First, we discuss the frequency scaling. Fig. 6.9 shows the spacing between a resonance and its photon sidebands as a function of the photon energy. Different markers correspond to different photon peaks. The factor  $\kappa = 35$   $\mu$ eV/mV to convert the peak spacings in mV gate voltage into energy is independently determined from dc measurements. The full width at half maximum value (FWHM) of the resonance without microwaves, indicated by the arrow, is proportional to



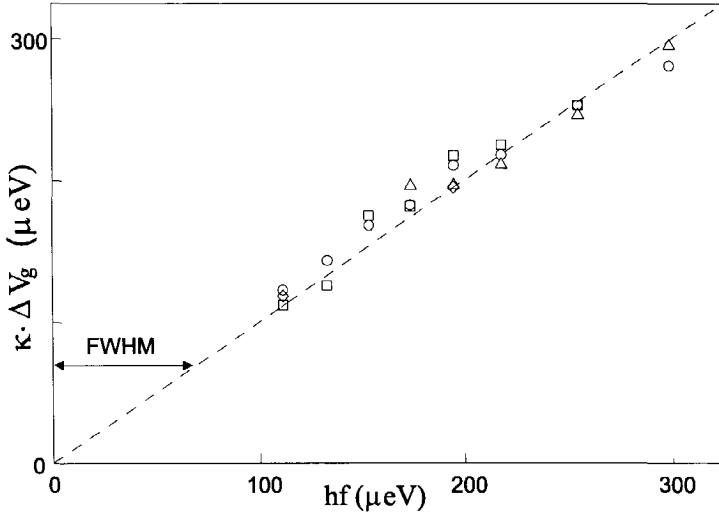


Figure 6.9: *Peak spacings versus the photon energy.*  $\square$ : spacing between  $\varepsilon_0$  and  $\varepsilon_0 - hf$ .  $\diamond$ : spacing between  $\varepsilon_0$  and  $\varepsilon_0 + hf$ .  $\triangle$ : spacing between  $\varepsilon_1$  and  $\varepsilon_1 - hf$ .  $\circ$ : spacing between  $\varepsilon_1$  and  $\varepsilon_1 + hf$ . The dashed line is based on the gate voltage to energy conversion factor  $\kappa$  independently determined from dc measurements, and has the theoretically expected slope equal to 1. The arrow indicates the FWHM of the peak.

the effective electron temperature in the leads. Structure due to photon energies below this value is washed out by the thermal energy  $k_B T$ . The frequency scaling firmly establishes PAT as the transport mechanism [4, 6, 7, 9]. The observation that the sidebands move linearly with frequency while the ground and excited state resonances stay fixed supports our identification of the different peaks.

### 6.5.5 magnetic field dependence

We can now use a magnetic field to change the energy separation between the ground state and the first excited state [12] while keeping the distance to the sidebands fixed. Fig. 6.10a shows the positions in gate voltage of all observed peaks for 52.5 GHz as a function of magnetic field. The filled circles reflect the evolution of  $\varepsilon_0$  with magnetic field. This ground state weakly oscillates with a periodicity of  $\sim 80$  mT which roughly corresponds to the addition of an extra fluxquantum to the dot. The filled diamonds reflect the evolution of  $\varepsilon_1$ . The

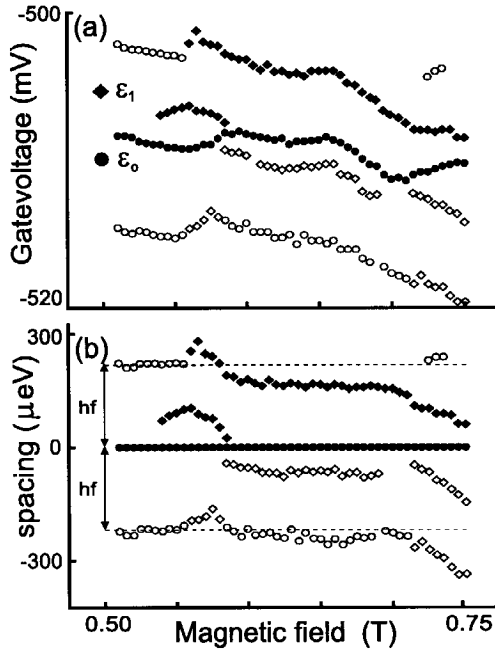


Figure 6.10: (a) Peak positions at different magnetic fields at 52.5 GHz. Solid symbols denote peaks which are independent of frequency. Open symbols denote peaks that scale with frequency. (b) Peak spacings relative to the main resonance converted to energy. Closed circles:  $\epsilon_0$ ; open circles:  $\epsilon_0 \pm hf$ ; closed diamonds:  $\epsilon_1$ ; open diamonds:  $\epsilon_1 - hf$  and  $\epsilon_1 - 2hf$ .

open circles (diamonds) show the sidebands  $\epsilon_0 \pm hf$  ( $\epsilon_1 \pm hf$ ). Fig. 6.10b shows the magnetic field evolution of the excited state and the photon sideband peaks relative to the ground state (i.e. we have subtracted  $\epsilon_0(B)$  from the other curves). We see that the energy splitting decreases on increasing the magnetic field and for  $0.54 \text{ T} < B < 0.58 \text{ T}$  a degeneracy of the ground state is temporarily lifted and actually two excited states are observed [21]. The dashed lines denote the photon energy  $hf = 217 \mu\text{eV}$  for 52.5 GHz. The open circles close to these lines are the photon processes  $\epsilon_0 \pm hf$  demonstrating that they indeed move together with the ground state. The open diamonds are the  $\epsilon_1 - hf$  and  $\epsilon_1 - 2hf$  processes. Their motion follows the motion of  $\epsilon_1$ . We have thus shown that we can vary the states  $\epsilon_0$  and  $\epsilon_1$  with the magnetic field and, independently, vary the separation to the sidebands with the microwave frequency.

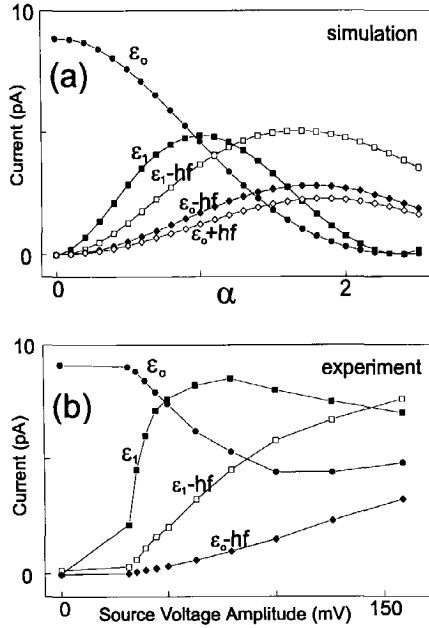


Figure 6.11: (a) calculation of the peak heights as a function of the ac voltage drop across the barriers  $\alpha = \frac{e\tilde{V}}{hf}$ .  $T = 200$  mK,  $V = 13$   $\mu$ V,  $f = 52.5$  GHz. The tunnelrates from the leads to the groundstate and the excited state are set to  $\Gamma_{\epsilon_0} = 5 \cdot 10^8$  s $^{-1}$  and  $\Gamma_{\epsilon_1} = 14 \cdot 10^8$  s $^{-1}$ , respectively. The relaxation rate from the excited state to the ground state is assumed to be zero in the calculation. (b) experimentally obtained peak heights as a function of the ac voltage amplitude (measured at the microwave source).  $V = 13$   $\mu$ V,  $f = 52.5$  GHz. The tunnelrates, obtained from dc current-voltage characteristics, are  $\Gamma_{\epsilon_0} = 5 \cdot 10^8$  s $^{-1}$  and  $\Gamma_{\epsilon_1} = 6 \cdot 10^8$  s $^{-1}$ .

### 6.5.6 power dependence

Fig. 6.11a shows a calculation of the peak heights as a function of the ac voltage drop across the barriers  $\alpha = \frac{e\tilde{V}}{hf}$ . These results were obtained using the master equation approach described in Ref. 17. Temperature, bias voltage, and frequency are taken from the experiment described below:  $T = 200$  mK,  $V_{SD} \approx 13$   $\mu$ V, and  $f = 52.5$  GHz. The tunnelrates from the leads to the groundstate and the excited state are set to  $\Gamma_{\epsilon_0} = 5 \cdot 10^8$  s $^{-1}$  and  $\Gamma_{\epsilon_1} = 14 \cdot 10^8$  s $^{-1}$ , respectively. The relaxation rate from the excited state to the ground state is assumed to be zero in the calculation. The effect of a finite relaxation rate is to reduce the

height of  $\varepsilon_1$  with respect to the other peaks since it would make the process  $\varepsilon_1$  described above less effective. The calculated peak heights roughly follow the Bessel functions in Eq. 6.4a. The groundstate resonance  $\varepsilon_0$  follows  $J_0^2(\alpha)$  since it involves only elastic tunnel events (see Fig. 6.3, diagram  $\varepsilon_0$ ). The photon sidebands follow  $J_1^2(\alpha)$ , since they solely depend on the probability of photon absorption. For example the process  $\varepsilon_0 - hf$  is due to a photon assisted tunnel event which fills the dot. Once the dot is filled, however, it does not matter whether the dot is emptied via an elastic or an inelastic event. The process  $\varepsilon_1$  follows the product of the first and second order Bessel functions  $J_0^2(\alpha)J_1^2(\alpha)$  since it requires that the ground state is emptied via a PAT process but also that the following tunneling processes through the excited state  $\varepsilon_1$  are elastic. Fig. 6.11b shows the experimental results for the peak heights at  $B = 0.91$  T and  $f = 52.5$  GHz as a function of the ac voltage amplitude at the output of the source. The measurements are in good qualitative agreement below an ac source voltage of 100 mV. At higher ac voltages the pumped current starts to become important. The values for the tunnel rates to  $\varepsilon_0$  and to  $\varepsilon_1$  derived from the dc current-voltage characteristic are  $\Gamma_{\varepsilon_0} = 5 \cdot 10^8 \text{ s}^{-1}$  and  $\Gamma_{\varepsilon_1} = 6 \cdot 10^8 \text{ s}^{-1}$ . The value for  $\Gamma_{\varepsilon_1}$  in the calculation is larger than the experimentally determined value but still the calculated value for the height of the  $\varepsilon_1$  resonance is smaller than the experimental value. It is a general trend in most of our data that the peak  $\varepsilon_1$  is higher than predicted by our model and that  $\varepsilon_0 + hf$  is lower than expected from simulations. At present this is poorly understood [22].

Simulations show that the pumped current is quite independent of the bias voltage when  $eV_{SD} \ll hf$  while current due to the photon resonances increases linearly with the bias voltage when  $eV_{SD} < k_B T$ . Therefore it is possible to improve the quality of our data by separating the pumped current from the photon resonances. This could be done by doing measurements for different bias voltages at every microwave power. This would allow for better comparison with calculations over a wider range of microwave powers.

In conclusion, we have used photon-assisted tunneling to study the interaction between microwave light and electrons occupying discrete 0D-states in a single quantum dot. The quality of our data shows the feasibility of recently proposed experiments on Rabi-type oscillations between coupled quantum dots [23].

We thank S.F. Godijn, K. Ishibashi, P. Lukey, P.L. McEuen, J.E. Mooij, Yu.V. Nazarov, and T.H. Stoof for discussions and experimental help. We thank Philips Laboratories and C.T. Foxon for providing the heterostructures. The work was supported by the Dutch Foundation for Fundamental Research on Matter (FOM). L.P.K. was supported by the Royal Netherlands Academy of Arts and Sciences (KNAW).

## References

- [1] U. Merkt, *Physica B* **189**, 165 (1993) and references therein.
- [2] R. Strenz et al., *Phys. Rev. Lett.* **73**, 3022 (1994) and references therein.
- [3] K. Brunner et al., *Phys. Rev. Lett.* **73**, 1138 (1994).
- [4] P.K. Tien and J.R. Gordon, *Phys. Rev.* **129**, 647 (1963).
- [5] Mixing is described by J. Inarrea, G. Platero and C. Tejedor, *Phys. Rev. B* **50**, 4581 (1994).
- [6] P.S.S. Guimares et al. *Phys. Rev. Lett.* **70**, 3792 (1993); B.J. Keay et al., *Phys. Rev. Lett.* **75**, 4098, (1995); B.J. Keay et al., *Phys. Rev. Lett.* **75**, 4102, (1995).
- [7] L.P. Kouwenhoven et al., *Phys. Rev. B* **50**, 2019 (1994); L.P. Kouwenhoven et al., *Phys. Rev. Lett.* **73**, 3433 (1994).
- [8] L.P. Kouwenhoven et al., *Zeitschrift für Physik* **85**, 381 (1991).
- [9] R.H. Blick et al., *Appl. Phys. Lett.* **67**, 3924 (1995).
- [10] D. Sokolovski, *Phys. Rev. B* **37**, 4201 (1988).
- [11] C. Bruder and H. Schöller, *Phys. Rev. Lett.* **72**, 1076 (1994).
- [12] A. T. Johnson et al., *Phys. Rev. Lett.* **69**, 1592 (1992).
- [13] See for reviews on quantum dots: U. Meirav and E.B. Foxman, *Semiconductor Science and Technology* **10**, 255 (1995); L.P. Kouwenhoven and P.L. McEuen, to be published in: *Nano-Science and Technology*, G. Timp ed. (AIP Press, New York).
- [14] D.V. Averin, A.N. Korotkov and K.K. Likharev, *Phys. Rev. B* **43**, 6199 (1991).
- [15] C.W.J. Beenakker, *Phys. Rev. B* **44**, 1646 (1991).
- [16] J.C. Wan et al., *Phys. Rev. B* **43**, 9381 (1991).
- [17] T.H. Oosterkamp et al., *Semiconductor Science and Technology*, to be published; and *Physica Scripta*, to be published.
- [18] M. Büttiker and R. Landauer, *Phys. Rev. Lett.* **49**, 1739 (1982).
- [19] PAT is also observed at  $B = 0$  but with less resolution due to a higher effective electron temperature at  $B = 0$ .
- [20] Because  $2hf > \Delta\varepsilon$  the excited state  $\varepsilon_1$  is weakly visible at  $V_g \sim -508$  mV in Fig. 6.7 where it overlaps with  $\varepsilon_0 + 2hf$ .

- [21] Our measurement of the evolution of the excited state  $\varepsilon_1$  agrees with the data in Fig. 4 of Ref. 12 and in Fig. 11 of P.L. Mc Euen et al., *Physica B* **189**, 70 (1993). However, we do not know of a theory that properly describes the observed magnetic field dependence of excited states.
- [22] Simulations reported by Ph. Brune, C. Bruder and H. Schöller, *Phys. Rev. B* **56**, 4730 (1997), included transitions from the ground-state to an excited state and give a better fit to the data. It is not clear, however, why these transitions would be so frequent. Other recent calculations reporting deviations from a simple Tien Gordon model were reported by M.H. Pedersen and M. Büttiker, *Phys. Rev. B* **58**, 12993 (1998).
- [23] T.H. Stoof and Yu.V. Nazarov, *Phys. Rev. B* **53**, 1050 (1996); C.A. Stafford and N.S. Wingreen, *Phys. Rev. Lett.* **76**, 1916 (1996).

## Chapter 7

# Microwave spectroscopy of a quantum dot molecule

T.H. Oosterkamp, T. Fujisawa, W.G. van der Wiel, K. Ishibashi,  
R.V. Hijman, S. Tarucha and L.P. Kouwenhoven.

### Abstract:

Quantum dots are small conductive regions in a semiconductor, containing a variable number of electrons ( $N=1$  to 1000) that occupy well defined discrete quantum states. They are often referred to as artificial atoms [1] with the unique property that they can be connected to current and voltage contacts. This allows one to use transport measurements to probe the discrete energy spectra. To continue the analogy with atoms, two quantum dots can be connected to form an 'artificial molecule'. Depending on the strength of the inter-dot coupling, the two dots can have an ionic binding [2-6] (i.e. electrons are localized on the individual dots) or a covalent binding (i.e. electrons are delocalized over both dots). The covalent binding leads to a bonding and an anti-bonding state with an energy splitting proportional to the tunnel coupling. In the dc current response to microwave excitation [5-8] we observe a transition from an ionic bonding to a covalent bonding, when we vary the inter-dot coupling strength. This demonstrates controllable quantum coherence in single electron devices.

When particles are allowed to tunnel back and forth between two quantum systems, the energy states of the individual systems mix and form new states that extend over both systems. The extended states are referred to as the bonding- or symmetric state, and the anti-bonding- or anti-symmetric state. In solid state systems the energy splitting between bonding and anti-bonding states have been observed in quantum well structures [9,10], superconducting tunneling devices [11,12], and exciton systems [13].

Quantum dots are uniquely engineered solid state systems in the sense that they have discrete states and the electrons on the dots are strongly interacting. The question whether different dots can be coupled together in a quantum-mechanically coherent way is non-trivial. The reason is that quantum dots composing single-electron devices are embedded in an environment with many electronic degrees of freedom. The electron that occupies the covalent state of a double dot system, has a Coulomb interaction with all the other electrons confined on the dots and also with the electrons in the current and voltage leads. These interactions can lead to dephasing of the quantum mechanical wave function resulting in a breakdown of the covalent state. For realistic devices there is no theory yet that can calculate reliable dephasing rates.

Nevertheless, if elements like quantum dots will ever be integrated in little quantum circuits [14-16], it is necessary that dots can be coupled coherently. This chapter reports on experiments that demonstrate this ability and, in our opinion, the cleanliness of the results are promising for manipulation of electrons in more complicated circuits. We have used microwave spectroscopy (0-50 GHz) to measure the energy differences between states in the two dots of the device [2] shown in Fig. 7.1a. We show that these energy differences, including the bonding-antibonding splitting, is controlled by gate voltages which tune the tunnel coupling between the dots. We first discuss the weak-coupling regime.

Electrons are strongly localized on the individual dots when tunneling between the two dots is weak. Electron transport is then governed by single-electron charging effects [8]. The charging energies can be tuned away by means of the gate voltages. It is then energetically allowed for an electron to tunnel between dots when a discrete state in the left dot is aligned with a discrete state in the right dot. External voltages also control the alignment of the discrete states. A current can flow when electrons can tunnel, while conserving energy, from the left lead, through the left and right dots, to the right lead. Note that energy is also conserved when photons of energy  $hf$  are absorbed from the microwave field which match the energy difference between the states of the two dots (see Fig. 7.1b).

The resonance in the lowest trace in Fig. 7.1c is due to an alignment of discrete



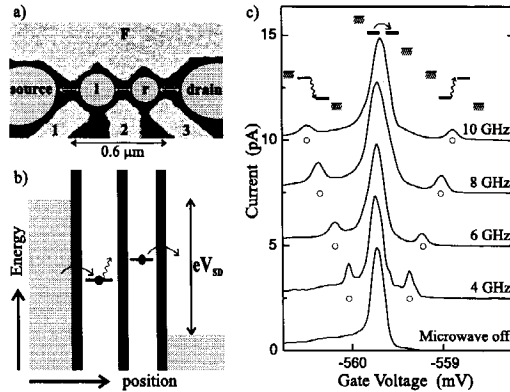


Figure 7.1: a) Photo of the double quantum dot sample. The source and drain regions as well as the left and right dots are indicated schematically. The tunnel barriers are depicted as arrows. The metallic gates (1, 2, 3, and F) are fabricated on top of a GaAs/AlGaAs heterostructure with a 2-dimensional electron gas (2DEG) 100 nm below the surface. At 4.2 K the 2DEG mobility is  $2.3 \times 10^6$  cm<sup>2</sup>/Vs and the electron density is  $1.9 \times 10^{15}$  m<sup>-2</sup>. Applying negative voltages to all the gates depletes the electron gas underneath them and forms two dots with estimated sizes of (170 nm)<sup>2</sup> and (130 nm)<sup>2</sup>. We measure the dc photo current in response to a microwave signal (0-50 GHz) that is capacitively coupled to gate 2. The tunnel coupling between the two dots and to the reservoirs can be controlled with the voltages on gate 1, 2 and 3. The dots contain about 60 and 35 electrons, respectively. The sample is cooled in a dilution refrigerator yielding an electron temperature in the source and drain contacts of  $\sim 100$  mK. b) Diagram of the electron energies in the dot for the case that an electron needs to absorb a photon in order to contribute to the current. Shaded areas represent the electron states in the leads that are continuously filled up to the Fermi levels. A voltage  $V_{SD}$  applied between the source and drain contacts shifts one Fermi level relative to the other. The discrete energy states in the two dots can be adjusted independently by changing the gate voltages. c) The upper diagrams illustrate three situations of the energy state in the left dot relative to the state in the right dot. The hatched lines denote the Fermi levels in the leads. The bottom curve shows the current as a function of the voltage on gate 1 for  $V_{SD} = 500$   $\mu$ V without applying microwaves. A single resonance occurs when two states line up. Other curves, which have been offset for clarity, show the current when microwaves with frequency  $f$  from 4 to 10 GHz are applied. Now, two additional satellite resonances occur when the two states are exactly a photon energy apart. The corresponding photon-assisted tunneling processes are illustrated in the upper diagrams.

states. The other traces are measured while applying a microwave signal. The satellite resonances are due to photon assisted tunneling processes which involve the emission (left satellite) or absorption (right satellite) of a microwave photon.

Stoof and Nazarov [17] give a detailed description of photon assisted tunneling in a double quantum dot. The basic idea is that electrons can absorb fixed quanta of energy  $hf$  from a classical oscillating field. An ac voltage drop  $V = V_{ac} \cos(2\pi ft)$  across a tunnel barrier modifies the tunnel rate through the barrier as [18]:

$$\tilde{\Gamma}(E) = \sum_{n=-\infty}^{+\infty} J_n^2(\alpha) \Gamma(E + nhf). \quad (7.1)$$

Here  $\tilde{\Gamma}(E)$  and  $\Gamma(E)$  are the tunnel rates at energy  $E$  with and without an ac voltage, respectively.  $J_n^2(\alpha)$  is the square of the  $n^{\text{th}}$  order Bessel function evaluated at  $\alpha = \frac{eV_{ac}}{hf}$ , which describes the probability that an electron absorbs or emits  $n$  photons of energy  $hf$ .

Figure 7.2 shows the current for several microwave powers. The dashed curve shows the main resonance measured at zero power. As the power is increased, satellite peaks appear corresponding to the absorption of multiple photons which are observed up to  $n = 11$ . At these high powers the microwaves strongly perturb tunneling. This is reflected by the non-linear dependence of the peak heights on power (left inset of Fig. 7.2), which is in agreement with the expected Bessel function behavior.

The right inset to Fig. 7.2 shows that the separation of the satellite peaks from the main peak depends linearly on frequency between 1 and 50 GHz. As we discuss below, this linearity implies that the tunnel coupling is negligible. The electrons are thus localized on the individual dots and they have an ionic bonding. The line proportional to  $2hf$  is taken from data at higher microwave powers where electrons absorb or emit two photons during tunneling.

In contrast to the case of weakly-coupled dots, covalent bonding occurs when two discrete states that are spatially separated become *strongly* coupled. Electrons then tunnel quickly back and forth between the dots. In a quantum mechanical description this results in a bonding and an anti-bonding state which are lower and higher in energy, respectively, than the original states. Our strong-coupling measurements were made on a second type of double-dot sample (see inset to Fig. 7.4). To single out the current only due to microwaves we operate the device as an electron pump driven by photons in a way described theoretically by Stafford and Wingreen [19] and by Brune et al. [20] (see the diagrams of Fig. 7.3a-c). By sweeping the gate voltages we vary  $\Delta E = E_{\text{left}} - E_{\text{right}}$ , where  $E_{\text{left}}$  and  $E_{\text{right}}$  are the energies of the uncoupled states in the left and

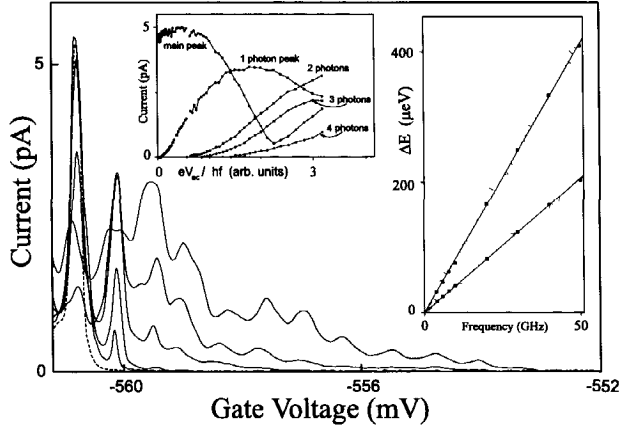


Figure 7.2: *Current versus gate voltage of a weakly coupled double-dot. The dashed curve is without microwaves and only contains the main resonance. The solid curves are taken at 8 GHz for increasing microwave powers resulting in an increasing number of satellite peaks. At the right side of the main peak these correspond to photon absorption. The source drain voltage  $V_{SD} = 700 \mu\text{V}$  and the photon energy  $hf = 33 \mu\text{eV}$  at 8 GHz. At the highest power we observe eleven satellite peaks, demonstrating multiple photon absorption. Left inset: Height of the first four satellite peaks as a function of the microwave amplitude. The observed height dependence agrees with the expected Bessel function behavior. Right inset: Distance between main resonance and first two satellites as a function of the applied frequency from 1 to 50 GHz. The distance is transferred to energy through  $\Delta E = \kappa \Delta V_g$  where  $\kappa$  is the appropriate capacitance ratio for our device that converts gate voltage to energy [8]. The agreement between data points and the two solid lines, which have slopes of  $h$  and  $2h$ , demonstrates that we observe the expected linear frequency dependence of the one and two photon processes.*

right dot. The bonding and anti-bonding states, that are a superposition of the wavefunctions corresponding to an electron in the left or in the right dot, have an energy splitting of  $\Delta E^* = E_{\text{anti-bond}} - E_{\text{bond}} = \sqrt{(\Delta E)^2 + (2T)^2}$ , where  $T$  is the tunnel coupling between the two dots. When the sample is irradiated, a photo current may result as illustrated in Fig. 7.3a-c. A non-zero current indicates that an electron was excited from the bonding state to the anti-bonding state, thereby fulfilling the condition  $hf = \Delta E^*$ , or conversely

$$\Delta E = \sqrt{(hf)^2 - (2T)^2}. \quad (7.2)$$

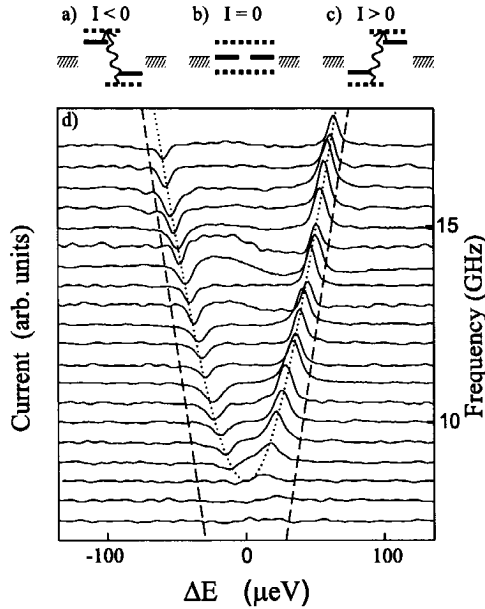


Figure 7.3: a) - c) Energy diagrams. Solid lines depict the energy states  $E_{left}$  and  $E_{right}$  in the two dots for the case that the coupling is weak and that their energy difference is simply  $\Delta E = E_{left} - E_{right}$ . When the dots are strongly-coupled, the states delocalize over both dots, thereby forming a bonding and an anti-bonding state. These are indicated by two dotted lines. Their energy difference is  $\Delta E^* = \sqrt{\Delta E^2 + (2T)^2}$ . Electrons are transferred from the bonding to the anti-bonding state when  $\Delta E^* = hf$ . In (a)  $E_{left} > E_{right}$  which results in electron pumping from right to left corresponding to a negative current. In (b) the whole system is symmetric ( $E_{left} = E_{right}$ ) and consequently the net electron flow must be zero. In (c)  $E_{left} > E_{right}$  which gives rise to pumping from left to right and a positive current. (d) Measured pumped current through the strongly-coupled double-dot. Gates 1 and 3 are swept simultaneously in such a way that we vary the energy difference  $\Delta E$ . The different traces are taken at different microwave frequencies and are offset such that the right vertical axis gives the frequency. The main resonance is absent since we have set  $V_{SD} = 0$ . The satellite peaks typically have an amplitude of 0.5 pA. For weakly-coupled dots the satellite peaks are expected to move linearly with frequency, thereby following the straight dashed lines. In contrast, we observe that the satellite peaks follow the fitted hyperbola  $hf = \sqrt{\Delta E^2 + (2T)^2}$  using  $T$  as a fitting parameter.

Figure 7.3 shows measured current traces as a function of the uncoupled energy splitting  $\Delta E$ , where from top to bottom the applied microwave frequency is decreased from 17 to 7.5 GHz in 0.5 GHz steps. The distance between the pumping peaks, which is proportional to  $2\Delta E$ , decreases as the frequency is lowered. However, the peak distance decreases faster than linear in frequency; the peaks follow the hyperbola rather than the straight lines. The distance goes to zero when the frequency approaches the minimum energy gap between bonding and anti-bonding states,  $hf = 2T$ . For frequencies smaller than the coupling,  $hf < 2T$ , the photon energy is too small to induce a transition from the bonding to the anti-bonding state.

The coupling between the dots can be decreased by changing the gate voltage on the center gate to more negative values or by applying a magnetic field perpendicular to the sample. In Fig. 7.4 we have plotted the energy spacing  $\Delta E$  at which the pumping current is at a maximum, as a function of frequency. Different labels correspond to different center gate voltage settings and magnetic fields. The solid lines are fits of equation (7.2) to the measured data. It follows that the coupling  $2T$  has been tuned from 11 to 60  $\mu\text{eV}$ . The good agreement with equation 2 and the clear non-linear frequency dependence demonstrates the control over the formation of a covalent bonding between the two dots.

Quantum dots have been suggested as possible candidates for building a quantum computer [14-16]. We have shown that it is indeed possible to coherently couple dots, and that one can induce transitions between the extended states. The next crucial step towards quantum logic gates is to show that the coherence of the superposition is preserved on time scales much longer than the time needed for manipulating the electron wave functions. A lower bound for the dephasing time is  $\tau_\phi > 1$  ns, which we deduce from our narrowest peaks and from the smallest energy gaps between the bonding and anti-bonding states that we have resolved. Future experiments include measurements of the decoherence time in which the states are manipulated by applying the microwaves in short pulses.

We thank R. Aguado, S.M. Cronenwett, S.F. Godijn, P. Hadley, C.J.P.M. Harmans, K.K. Likharev, J.E. Mooij, Yu. V. Nazarov, R.M. Schouten, T.H. Stoof and N.C. van der Vaart for experimental help and useful discussions. This work was supported by the Dutch Organization for Research on Matter (FOM) and by the EU via the TMR network. L.P.K. was supported by the Dutch Royal Academy of Arts and Sciences (KNAW).

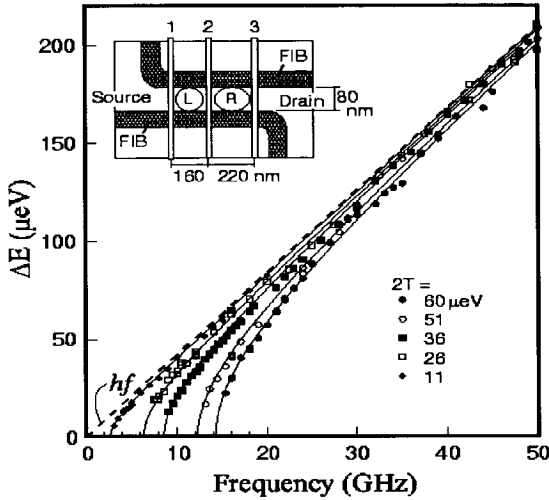


Figure 7.4: Half the spacing in gate voltage between the positive and negative satellite peaks as a function of frequency. Gate voltage spacing has been transferred to energy difference  $\Delta E$  (see also figure caption 2). Different curves correspond to different coupling constants  $T$ . Solid lines are theoretical fits to  $\Delta E = \sqrt{(hf)^2 - (2T)^2}$ . The resulting values for  $2T$  are given in the figure. In the limit of weak-coupling this reduces to  $\Delta E = hf$  which is indicated by the dashed line. The coupling is varied by applying different voltages to the center gate (2) or by changing the magnetic field ( $\blacklozenge$ :  $B = 3.3$  T;  $\blacksquare$ :  $B = 2.2$  T; other curves:  $B = 0$ ). The upper left inset shows a diagram of the sample<sup>5</sup>. A narrow channel is defined by locally depleting the 2DEG using focussed ion beam implantation (FIB). Two dots are then formed by applying negative voltages to the three gates (1, 2, 3) that cross the channel. Microwaves are capacitively coupled to gate 2.

## References

- [1] R. Ashoori, *Electrons in artificial atoms*, Nature **379**, 413-419 (1996).
- [2] N.C. van der Vaart et al., *Resonant tunneling through two discrete energy states*, Phys. Rev. Lett. **74**, 4702-4705 (1995).
- [3] C. Livermore et al., *The Coulomb blockade in coupled quantum dots*, Science **274**, 1332-1335 (1996).

- [4] R. Blick et al., *Single electron tunneling through a double quantum dot: The artificial molecule*, Phys. Rev. B **53**, 7899-7902 (1996).
- [5] T. Fujisawa and S. Tarucha, *Photon assisted tunneling in single and coupled quantum dot systems*, Superlattices and Microstructures **21**, 247-254 (1997).
- [6] T. Fujisawa and S. Tarucha, *Multiple photon assisted tunneling between two coupled quantum dots*, Jpn. J. Appl. Phys. **36**, 4000-4003 (1997).
- [7] T.H. Oosterkamp et al., *Photon sidebands of the ground state and first excited state of a quantum dot*, Phys. Rev. Lett. **78**, 1536-1539 (1997).
- [8] L.P. Kouwenhoven et al., *Electron transport in quantum dots*, in *Mesoscopic Electron Transport*, edited by L. Sohn et al., 105-214 (Kluwer Series E, 1997). See also <http://vortex.tn.tudelft.nl/~leok/papers>.
- [9] K. Leo et al., *Coherent oscillations of a wave packet in a semiconductor double-quantum well structure*, Phys. Rev. Lett. **66**, 201-204 (1991).
- [10] E. E. Mendez and G. Bastard, *Wannier-Stark ladders and Bloch oscillations in superlattices*, Physics Today, 34-42 (June 1993).
- [11] D.J. Flees et al., *Interband transitions and band gap measurements in Bloch transistors*, Phys. Rev. Lett. **78**, 4817-4820 (1997).
- [12] Y. Nakamura et al., *Spectroscopy of energy-level splitting between two macroscopic quantum states of charge coherently superposed by Josephson coupling*, Phys. Rev. Lett. **79**, 2328-2331 (1997).
- [13] G. Schedelbeck et al., *Coupled quantum dots fabricated by cleaved edge overgrowth: From artificial atoms to molecules*, Science **278**, 1792-1795 (1997).
- [14] R. Landauer, *Minimal energy requirements in communication*, Science **272**, 1914-1918 (1996).
- [15] A. Barenco et al., *Conditional quantum dynamics and logic gates*, Phys. Rev. Lett. **74**, 4083-4086 (1995).
- [16] D. Loss and D.P. DiVincenzo, *Quantum computation with quantum dots*, Phys. Rev. A **57**, 120-126 (1998).
- [17] T.H. Stoof and Yu.V. Nazarov, *Time-dependent resonant tunneling via two discrete states*, Phys. Rev. B **53**, 1050-1053 (1996).
- [18] P.K. Tien and J.R. Gordon, *Multiphoton process observed in the interaction of microwave fields with the tunneling between superconductor films*, Phys. Rev. **129**, 647-651 (1963).

- [19] C.A. Stafford and N.S. Wingreen, *Resonant photon-assisted tunneling through a double quantum dot: An electron pump from spatial Rabi oscillations*, Phys. Rev. Lett. **76**, 1916-1919 (1996) .
- [20] Ph. Brune et al., *Photon-assisted transport through a double quantum dot with a time-dependent interdot barrier*, Physica E **1**, 216-218 (1997).



## Chapter 8

# Spontaneous emission spectrum in double quantum dot devices

T. Fujisawa, T.H. Oosterkamp, W.G. van der Wiel,  
B.W. Broer, R. Aguado, S. Tarucha and  
L.P. Kouwenhoven.

### **Abstract:**

A double quantum dot device is a tunable two-level system for electronic energy states. A dc electron current directly measures the rates for elastic and inelastic transitions between the two levels. For inelastic transition energy is exchanged with bosonic degrees of freedom in the environment. The inelastic transition rates are well described by the Einstein coefficients, relating absorption with stimulated and spontaneous emission. The most effectively coupled bosons in the specific environment of our semiconductor device are acoustic phonons. The experiments demonstrate the importance of vacuum fluctuations in the environment for little circuits of coherent quantum devices.

Electronic quantum devices explore quantum mechanical properties of electrons confined to small regions in a solid by means of modern fabrication techniques. Existing devices include semiconductor resonant tunneling diodes [1] (based on quantum mechanical confinement), superconducting Josephson junction circuits [2] (based on macroscopic phase coherence), metallic single electron transistors [3] (based on quantization of charge), and molecular electronic devices [4]. The principle of operation in circuits of these devices is based on controlling energy states, for instance, by means of an external (gate) voltage. One source for unwanted transitions and errors is always the thermal energy from a non-zero temperature. However, even at zero temperature vacuum fluctuations in the environment can give rise to transitions between states of non-equal energy by spontaneous emission of an energy quantum. Such inelastic transitions cause errors in many proposed schemes for quantum circuits. We have studied inelastic transitions in a fully-controllable, two-level quantum system realized in a double quantum dot device. We can relate the transition rates involving emission to absorption rates by the Einstein coefficients over our full energy and temperature range. At our lowest temperature we directly measure the energy-dependent rate for spontaneous emission. In our specific semiconductor device this energy is emitted into the environment formed by acoustic phonons.

Our double quantum dot (Fig. 8.1a) is fabricated in the two-dimensional electron gas (2DEG) of an AlGaAs/GaAs semiconductor heterostructure [5]. The source and drain are large 2DEG regions which serve as leads for contacting current and voltage wires. The two dots,  $L$  and  $R$ , are separated from each other and from the leads, by potential barriers induced by negative voltages applied to the three metallic gates. Tunneling between the different regions is sufficiently strong to detect current, but weak enough such that the number of electrons in each dot is a well-defined integer. The energy states in such fully confined regions are discrete, 0D-states; resembling discrete atomic states [6,7]. The discrete energies include contributions from single-electron charging energies, arising from Coulomb interactions, and from quantum-mechanical confinement. The lowest energy state for one additional electron in the left dot is labeled in Fig. 8.1b-d as  $E_L$  and similarly  $E_R$  for the right dot. Fig. 8.1c illustrates the resonance condition,  $E_L = E_R$ , in which case an electron can tunnel elastically from an occupied state in the source via  $E_L$  and  $E_R$  to an empty state in the drain. Such tunneling sequences of single electrons are regulated by the Coulomb charging energies [3,7]. When the two states are not aligned,  $E_L \neq E_R$ , only inelastic transitions are allowed for which some energy needs to be exchanged with the environment. A measured off-resonance current, therefore, directly provides information about the coupling between electrons on the dots to degrees of freedom in the envi-

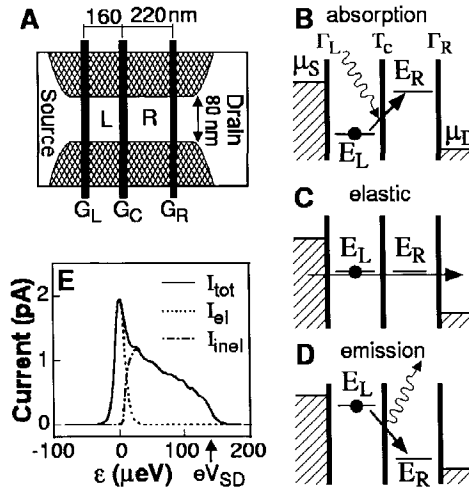


Figure 8.1: a) Double quantum dot device defined in the 2DEG of a GaAs/AlGaAs hetero structure by focused ion beam implantation. The narrow channel connects the large 2D source and drain leads. Negative voltages ( $V_{GL}$ ,  $V_{GC}$ , and  $V_{GR}$ ) applied to the metal gates ( $G_L$ ,  $G_C$ , and  $G_R$ ; widths are 40 nm) induce three tunable tunnel barriers in the wire. The two quantum dots, L and R, respectively, contain  $\sim 15$  and  $\sim 25$  electrons; charging energies are  $\sim 4$  and  $\sim 1$  meV; and the measured average spacing between single-particle states are  $\sim 0.5$  and  $\sim 0.25$  meV. (b, c, and d) Energy diagrams (vertical axis) along the spatial axis through the dots (horizontal axis) for the tunnel situations: absorption, elastic and emission. Thick vertical lines denote tunnel barriers. The continuous electron states in the leads are filled up to the Fermi energies  $\mu_S$  and  $\mu_D$ . The external voltage  $V_{sd}$  between leads opens a transport window of size:  $eV_{sd} = \mu_S - \mu_D$ . The energy,  $\epsilon \equiv E_L - E_R$ , is defined as the difference between the topmost filled discrete-state of the left dot,  $E_L$ , and the lowest discrete-state for adding an extra electron to the right dot,  $E_R$ . (The inter-dot capacitance prevents that  $E_L$  and  $E_R$  are simultaneously occupied.) An elastic current can flow when  $\epsilon = 0$ , otherwise a non-zero current requires absorption ( $\epsilon < 0$ ) or emission of energy ( $\epsilon > 0$ ).  $T_C$  is the tunnel coupling and  $\Gamma_i$  is the inelastic rate between the two dots.  $\Gamma_L$  and  $\Gamma_R$  are the tunnel rates across the left and the right barriers. (e) Typical measurement of the current (solid) versus  $\epsilon$  at 23 mK. The measured current is decomposed in an elastic (dashed) and an inelastic (dotted-dashed) part.

ronment. The inelastic rates can be analyzed with well-developed methods in quantum optics [8,9].

Figure 8.1e shows a typical current spectrum versus  $\varepsilon \equiv E_L - E_R$  at our lowest lattice temperature  $T = 23$  mK [10]. The gate voltages  $V_{GR}$  and  $V_{GL}$  are swept simultaneously such that the respective energies are like in Fig. 8.1b-d; that is,  $\varepsilon = 0$  occurs in the middle between the Fermi energies of source and drain,  $\mu_S$  and  $\mu_D$ , and  $|\varepsilon| = eV_{SD}$  is maximal corresponds to having the states  $E_L$  and  $E_R$  aligned to one of the Fermi energies. To analyze the large asymmetry, we decompose the total current  $I_{tot}(\varepsilon) = I_{el}(\varepsilon) + I_{inel}(\varepsilon > 0)$  into a symmetric part  $I_{el}(\varepsilon) = I_{el}(-\varepsilon)$  (dashed curve) and the remaining asymmetric part  $I_{inel}(\varepsilon > 0)$  (dotted-dashed curve). At  $T = 0$ ,  $I_{el}(\varepsilon)$  is due to elastic tunneling and has a Lorentzian lineshape  $I_{el}(\varepsilon) = I_{el,max}w^2/(w^2 + \varepsilon^2)$  [11]. The full width at half maximum (FWHM),  $2w$ , can be tuned by the central gate voltage  $V_{GC}$  roughly from 4 to 20  $\mu\text{eV}$ . From measurements of  $I_{el}(\varepsilon)$  at positive and negative  $V_{SD}$  it is possible to extract values for the tunnel couplings  $\Gamma_L$ ,  $\Gamma_R$  and  $T_c$  [11,12].

The remaining current,  $I_{inel}(\varepsilon > 0)$ , which is non-zero only for  $\varepsilon > 0$  (at  $T = 0$ ), is due to inelastic tunneling. In Fig. 8.1e,  $I_{inel}$  is non-zero over an energy range of  $\sim 100$   $\mu\text{eV}$ ; this despite that the thermal energy  $k_B T$  (23 mK) = 2  $\mu\text{eV}$  is much smaller. (The irregular fine structure is discussed below.) In general we find that  $I_{inel}$  vanishes when one of the levels,  $E_L$  or  $E_R$ , crosses one of the two Fermi energies. In the specific case of Fig. 8.1e,  $E_L$  and  $E_R$  cross the Fermi energies simultaneously, implying that  $I_{inel}$  is cut off at  $\varepsilon = eV_{SD}$ . Below this cut off, the value of  $I_{inel}$  was not influenced by the value of  $V_{SD}$  [13]. For  $T = 0$ , we can write the condition for a non-zero inelastic current as  $\mu_S > E_L > E_R > \mu_D = \mu_S - eV_{SD}$ . The amount of inelastic current depends on the transition rates as:  $I_{inel}(\varepsilon) = e(\Gamma_L^{-1} + \Gamma_i^{-1}(\varepsilon) + \Gamma_R^{-1})^{-1}$ . When the inelastic rate  $\Gamma_i(\varepsilon)$  from  $E_L$  to  $E_R$  is much smaller than the rates through the outer barriers, this reduces to  $I_{inel}(\varepsilon) = e\Gamma_i(\varepsilon)$ .

The effect of a non-zero temperature on the current is shown in Fig. 8.2a. A higher temperature  $T$ , enhances  $I_{tot}$  on both the emission ( $\varepsilon > 0$ ) and the absorption ( $\varepsilon < 0$ ) side. The absorption spectrum shows an exponential temperature dependence,  $e^{\varepsilon/kT}$  (dashed lines) for absolute energies larger than the elastic current measured at 23 mK, that is  $|\varepsilon| > w$ .

To analyze the temperature dependence, we assume boson statistics for the degrees of freedom in the environment. The average occupation number  $\langle n \rangle$  of environmental modes at energy  $\varepsilon$  is given by the Bose-Einstein distribution function:  $\langle n \rangle = 1/(e^{\varepsilon/kT} - 1)$ . The rates for absorption,  $W_a$ , and emission,  $W_e$ , can be expressed very generally by  $W_a = B_a\rho$  and  $W_e = A + B_e\rho$ , where the Einstein coefficients stand for spontaneous emission ( $A$ ), stimulated emission

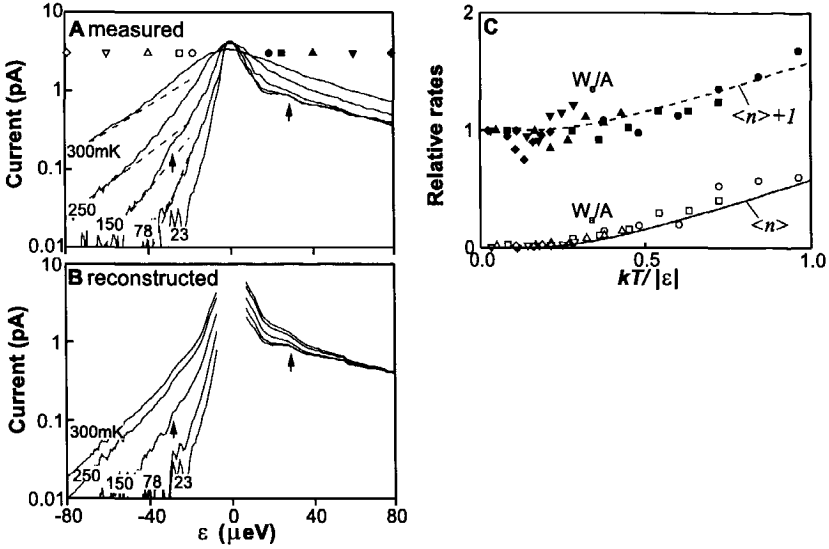


Figure 8.2: a) Measured current versus  $\epsilon$  for  $T = 23$  to  $300$  mK. The current is measured for  $eV_{SD} = 140$   $\mu\text{eV}$  while sweeping  $V_{GR}$  and  $V_{GL}$  simultaneously in opposite directions such that we change the energy difference  $\epsilon$ . Gate voltage is translated to energy  $\epsilon$  by a calibration better than 10% using photon-assisted tunneling measurements (16). Dashed lines indicate exponential dependence,  $e^{\epsilon/kT}$ , for  $|\epsilon| \gg kT$ . Arrows point at step-like structure on the emission side ( $\epsilon > 0$ ) and a shoulder on the absorption side ( $\epsilon < 0$ ). From fits (11) to the elastic current part at 23 mK we obtain  $\hbar\Gamma_L \approx \hbar T_c \approx 1$   $\mu\text{eV}$  and  $\hbar\Gamma_R \approx 0.1$   $\mu\text{eV}$  for this dataset. (b) Reconstructed current for different  $T$ . The spontaneous emission spectrum derived from the measured data at 23 mK and Eqs. 8.1 are used to reconstruct the full temperature and energy dependence. (c) The absorption rate  $W_a$  (open symbols) and emission rate  $W_e$  (closed symbols) normalized by the spontaneous emission rate  $A$  versus  $kT/|\epsilon|$ . Circles, squares, upper- and lower-triangles, and diamonds are taken at  $|\epsilon| = 18, 24, 40, 60,$  and  $80$   $\mu\text{eV}$ , respectively (see also symbols in a). The solid line indicates the Bose-Einstein distribution,  $\langle n \rangle$ , whereas the dashed line shows  $\langle n \rangle + 1$ .

( $B_e$ ) and absorption ( $B_a$ ), and  $\rho$  is the energy density [8]. From the Einstein relations,  $B_a = B_e = A\langle n \rangle / \rho$  [8], we obtain:

$$\begin{aligned}\Gamma_i(\varepsilon < 0) &= W_a(\varepsilon) = \langle n \rangle A(-\varepsilon) \\ \Gamma_i(\varepsilon > 0) &= W_e(\varepsilon) = (\langle n \rangle + 1)A(\varepsilon)\end{aligned}\quad (8.1)$$

To test whether the inelastic current follows emission and absorption statistics, we calculate the full current spectrum from Eqs. 8.1. First, we obtain the spontaneous emission rate from  $A(\varepsilon) = I_{inel}(\varepsilon > 0, T = 23 \text{ mK})/e$ . The trace at 23 mK is effectively at zero temperature for  $\varepsilon \gg 2 \mu\text{eV}$  since then  $\langle n \rangle \ll 1$ . The emission current at higher temperatures follows from  $I_{inel}(\varepsilon > 0, T) = e(\langle n \rangle + 1)A(\varepsilon)$ , whereas the absorption current follows from  $I_{inel}(\varepsilon < 0, T) = e\langle n \rangle A(-\varepsilon)$ . The reconstructed current spectrum is shown in Fig. 8.2b. The central part of the curves ( $|\varepsilon| < 10 \mu\text{eV}$ ) is kept blank since Eq. 8.1 does not include the  $T$ -dependence of  $I_{el}$ . The calculated current reproduces the measured current well up to 200 mK. Even the small step-like feature seen at  $\varepsilon \sim 30 \mu\text{eV}$  is reflected by a shoulder-like feature at  $\varepsilon \sim -30 \mu\text{eV}$  in the measured and in the calculated absorption spectra (indicated by arrows). For  $T > 200 \text{ mK}$  the measured current significantly exceeds the calculated current, which is probably due to thermally excited electrons (Eq. 8.1 only describes the  $T$ -dependence of the environment. The thermal excitations in the electron leads are not included.) Further confirmation of the applicability of the Einstein relations to our quantum dot system follows from the prediction:

$$\frac{I_{inel}(\varepsilon > 0) - I_{inel}(\varepsilon < 0)}{eA(|\varepsilon|)} = \frac{W_e - W_a}{A} = 1$$

which is valid independent of temperature. Fig. 8.2c shows a plot of the normalized rates,  $W_a/A$  and  $W_e/A$ , versus  $k_B T/|\varepsilon|$  for various  $\varepsilon$  and  $T$  up to 200 mK. The measured data closely follow the prediction  $\frac{W_e - W_a}{A} = 1$ ; that is, the normalized rates,  $W_a/A$  and  $W_e/A$ , differ by one over the temperature range  $T < 200 \text{ mK}$  without fitting any parameter.

The inelastic rate for a two-level system coupled to a bosonic environment at  $T = 0$  is expected to have a  $T_c^2$  dependence [14,15]. Still without identifying the bosonic environment, we can test this dependence on the elastic tunnel coupling  $T_c$  between the two dots. Figure 8.3a shows that the inelastic current clearly increases with  $T_c$ . For the largest coupling we obtain a saturation where the elastic current peak can no longer be distinguished. By fitting the elastic current part to a Lorentzian lineshape [11] we can obtain rough estimates for  $T_c$  as long as the current is less than the saturation value. We find that with these fitted values, the inelastic current scales as  $T_c^\alpha$  with an exponent  $\alpha = 2.5 \sim 3$ , may be somewhat

larger than expected. Figure 8.3b shows the effect of the increased coupling on the symmetric part of the current at low temperature. For small tunnel coupling, we always obtain Lorentzian lineshapes. For increasing couplings, the data still fits to a Lorentzian tail on the absorption side. However, we generally find significant deviations for small  $\varepsilon$ , implying that for large coupling the elastic and inelastic rates can become of the same order. This may form a significant limitation for the coherence time in coupled quantum devices [16].

The importance of fluctuations in the environment on electron tunneling through quantum devices has been recognized for a long time. Environmental studies on Coulomb blockade devices have only discussed effects due to absorption [3]. For emission it is required that electrons are first pumped to a higher energy state. This has recently been done in a superconducting Cooper pair transistor under microwave irradiation [17]. In the case of a double dot, pumping occurs when  $E_L > E_R$  and an electron tunnels in from the left reservoir to  $E_L$ . A double dot thus offers a unique two-level system that is pumped by a dc voltage without inducing heating currents. It is therefore possible to reach an out-of-equilibrium situation so close to  $T = 0$  that vacuum fluctuations become the main source for generating electron transport.

To identify whether photons, plasmons, or phonons form the bosonic environment, we measured spontaneous emission spectra while placing the double dot in different electromagnetic environments. In the regime 10-100  $\mu\text{eV}$ , the typical wavelengths are 1-10 cm for photons and 0.3 to 30 cm for 2DEG plasmons. We have tested the coupling to the photonic environment by placing the sample in microwave cavities of different size [18]. To check the coupling to plasmons, we have measured different types of devices with largely different dimensions of the 2DEG leads, gate pads, and bonding wires. Both types of variation had no effect at all on the emission spectra; even the finestructure was reproduced.

The third option of acoustic phonons is the most likely possibility [19]. Phonon emission rates have been calculated for single dots [20]. For a double dot system, we can obtain the general energy dependence [15]. For a deformation potential we expect a rate dependence of  $\varepsilon^{D-2}$  ( $\varepsilon$  for 3D phonons and constant for 2D phonons) and for piezo-electric interaction of  $\varepsilon^{D-4}$  ( $1/\varepsilon$  for 3D phonons and  $1/\varepsilon^2$  for 2D surface acoustic waves) [21]. In Fig. 8.3c we compare traces measured on two different types of devices. Here, the emission current is plotted versus  $\varepsilon$  on a log-log scale. Ignoring the bumps, we find an energy dependence between  $1/\varepsilon$  and  $1/\varepsilon^2$ . This implies that the dominant emission mechanism is the piezo-electric interaction with 2D or 3D acoustic phonons. Note that a  $1/\varepsilon$  or  $1/\varepsilon^2$  dependence should be avoided in coherent devices, since the inelastic rate becomes large near resonance ( $\varepsilon \sim 0$ ) [16].

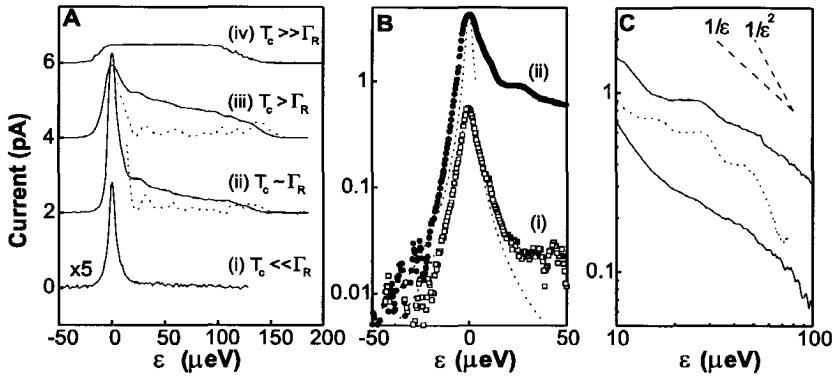


Figure 8.3: Current spectrum for different coupling energies at 23 mK. (a) The magnetic field is 1.6 T for (i) and 2.4 T for the other curves (10). The curves have an offset, and curve (i) is multiplied by 5. Rough estimates for the coupling energies are: (i)  $hT_c \ll h\Gamma_R$  ( $\sim 0.1 \mu\text{eV}$ ), (ii)  $hT_c \approx h\Gamma_R$  ( $\sim 1 \mu\text{eV}$ ), (iii)  $hT_c > h\Gamma_R$  ( $\sim 0.1 \mu\text{eV}$ ), and (iv)  $hT_c \gg h\Gamma_R$  ( $\sim 0.01 \mu\text{eV}$ ) and  $\Gamma_L \gtrsim \Gamma_R$  for all curves. The two dotted curves are the derivatives  $-dI/d\varepsilon$  in arbitrary units for curves (i) and (ii) to enhance the bump-structure. (b) Logarithmic-linear plots for (i) and (ii). Dashed lines are Lorentzian fits. For (ii) we chose parameters that fit the tail for negative  $\varepsilon$ . (c) Logarithmic-logarithmic plots of the emission spectrum for two different samples. The solid lines are taken on the FIB sample in Fig. 1A (upper trace is the same as (ii) in a; lower trace is for coupling energies between (i) and (ii) in a). The dotted line is taken on a surface gate sample with a distance between left and right barriers of 600 nm (12). The dashed lines indicate a  $1/\varepsilon$  and  $1/\varepsilon^2$  dependence expected for piezo-electric interaction with 3D and 2D phonons, respectively.

The bumps observed in both type of devices, suggest the existence of resonances, for instance, due to a finite size in the phonon environment. The bumps are particularly clear in the derivative of the current to energy (dotted curves in Fig. 8.3a). The large bump in Fig. 8.3a at  $\varepsilon = 30 \mu\text{eV}$  corresponds to a frequency of  $f = \varepsilon/h = 7.3 \text{ GHz}$ . For 3D phonons this yields a wavelength  $\lambda^{3D} = s^{3D}/f = 640 \text{ nm}$  ( $s^{3D} = 4800 \text{ m/s}$  is the 3D sound velocity), whereas for 2D surface acoustic waves  $\lambda^{2D} = s^{2D}/f = 380 \text{ nm}$  ( $s^{2D} = 2800 \text{ m/s}$ ). These wavelengths both, more or less, fit with the dimensions of the two quantum dot devices. We have not yet been able to control these resonance by studying devices



with a variety of gate dimensions. However, we believe that it is possible to gain control over the phonon environment by making 3D phonon cavities in hanging bridges [22] or by creating a 2D phonon bandgap using a periodic gate geometry [23].

We thank M. Devoret, L. Glazman, S. Godijn, Y. Hirayama, J. Mooij, Yu. Nazarov, Y. Tohkura, N. Uesugi, M. Uilenreef, and N. van der Vaart for help and discussions. Supported by the Dutch Foundation for Fundamental Research on Matter (FOM), L.P.K. by the Royal Netherlands Academy of Arts and Sciences.

## References

- [1] H. Mizuta and T. Tanoue, *The Physics and Applications of Resonant Tunneling Diodes* (Cambridge Univ. Press, Cambridge).
- [2] *The New Superconducting Electronics, Proceedings of a NATO Advanced Study Institute*, H. Weinstock and R.W. Ralston Eds. (Kluwer, Dordrecht, 1992), ser. E, vol. 251.
- [3] *Single Charge Tunneling*, H. Grabert and M. H. Devoret, Eds., (Plenum Press, New York, 1992) Ser. B, vol. 294.
- [4] P. L. McEuen, *Nature*, **393**, 15 (1998); S. J. Tans, A. R. M. Verschueren, and C. Dekker, *Nature*, **393**, 49 (1998).
- [5] T. Fujisawa and S. Tarucha, *Superlattices and Microstructures* **21**, 247 (1997); *Jpn. J. Appl. Phys.* **36**, 4000 (1997).
- [6] See for recent popular reviews: R. Ashoori, *Nature* **379**, 413 (1996); L. P. Kouwenhoven and C. M. Marcus, *Physics World*, pp.35-39 (June 1998).
- [7] For a review, see L. P. Kouwenhoven et al., in *Mesoscopic Electron Transport, Proceedings of a NATO Advanced Study Institute*, L. L. Sohn, L. P. Kouwenhoven, and G. Schön, Eds., (Kluwer, Dordrecht, 1997), ser. E, vol. 345, pp. 105-214; available on line at <http://vortex.tn.tudelft.nl/~leok/papers/>.
- [8] P. W. Milonni, *The Quantum Vacuum, an Introduction to quantum electrodynamics* (Academic Press, San Diego, 1994).
- [9] The statistics of our inelastic emission should be regulated by the statistics of single-electron tunneling, see A. Imamoglu and Y. Yamamoto, *Phys. Rev. B* **46**, 15982 (1992).
- [10] The sample was cooled in a dilution refrigerator with a lowest temperature of 23 mK. Due to noise, the effective electron temperature is  $\sim 50$  mK in the leads. In all measurements we apply a perpendicular magnetic field between

- 1.6 and 2.4 T to maximize the single-particle spacing such that we can neglect transport through excited states.
- [11] The elastic current is given by the formula  $I_{elastic}(\varepsilon) = eT_c^2\Gamma_R/(T_c^2(2 + \Gamma_R/\Gamma_L) + \Gamma_R^2/4 + (\varepsilon/h)^2)$ , see Yu. V. Nazarov, *Physica B* **189**, 57 (1993); T. H. Stoof and Yu. V. Nazarov, *Phys. Rev. B* **53**, 1050 (1996).
- [12] N. C. van der Vaart, et al., *Phys. Rev. Lett.* **74**, 4702 (1995).
- [13] Also co-tunneling can give excess current for  $\varepsilon \neq 0$ . In our measurements, however, the co-tunneling current is less than 0.01 pA and can be neglected. For a review on co-tunneling see D. V. Averin and Yu. V. Nazarov, in Ref. 3, pp. 217-247.
- [14] A. J. Leggett, et al., *Rev. Mod. Phys.*, **59**, 1 (1987).
- [15] A  $T_c^2$ -dependence can also be obtained from perturbation theory when  $T_c \ll \varepsilon$ , see L. I. Glazman and K. A. Matveev, *Sov. Phys. JETP* **67**, 1276 (1988).
- [16] We have reported a coherent coupling effect in double quantum dots using photon-assisted tunneling experiments, in the previous chapter. These observations are made when a small bias voltage is applied. In this case emission processes do not give rise to current.
- [17] Y. Nakamura, C. D. Chen, and J. S. Tsai, *Phys. Rev. Lett.* **79**, 2328 (1997).
- [18] We used a cylindrical cavity (36 mm $\phi$   $\times$  84 mm) which has a minimum resonance energy of about 20  $\mu$ eV, and a rectangular cavity (22  $\times$  19  $\times$  8 mm<sup>3</sup>) with resonance frequency of about 40  $\mu$ eV.
- [19] Coupling to optical phonons is efficient only at much larger energies.
- [20] U. Bockelmann, *Phys. Rev. B* **50**, 17271 (1994).
- [21] For phonons the inelastic rate at  $T = 0$  can be written as  $\Gamma_i \sim (T_c/\varepsilon)^2 J(\varepsilon/\hbar)$  where  $J(\varepsilon) \sim \frac{c^2(\varepsilon)}{\varepsilon} g(\varepsilon)$  is the spectral function [14]. The phonon density of states  $g(\varepsilon) \sim \varepsilon^{D-1}$ , such that  $\Gamma_i \sim T_c^2 c^2(\varepsilon) \varepsilon^{D-4}$ . When we neglect possible fine structure in  $c(\varepsilon)$ , we have for deformation potential  $c \sim \varepsilon$  and thus  $\Gamma_i \sim \varepsilon^{D-2}$ , while for piezo-electric interaction  $c \sim \text{constant}$  and thus  $\Gamma_i \sim \varepsilon^{D-4}$ .
- [22] A. N. Cleland and M. L. Roukes, *Nature*, **392**, 160 (1998).
- [23] J. M. Shilton, et al., *J. Phys.: Cond. matter* **8**, L531 (1997).

## Chapter 9

# A tuneable Kondo effect in quantum dots

S.M. Cronenwett, T.H. Oosterkamp, and L.P. Kouwenhoven.

### **Abstract:**

We demonstrate a tuneable Kondo effect realized in small quantum dots. We can switch our dot from a Kondo system to a non-Kondo system as the number of electrons on the dot is changed from odd to even. We show that the Kondo temperature can be tuned by means of a gate voltage as a single-particle energy state nears the Fermi energy. Measurements of the temperature and magnetic field dependence of a Coulomb-blockaded dot show good agreement with predictions of both equilibrium and non-equilibrium Kondo effects.

Quantum dots are small solid state devices in which the number of electrons can be made a well-defined integer  $N$ . The electronic states in dots can be probed by transport when a small tunnel coupling is allowed between the dot and nearby source and drain leads. This coupling is usually made as weak as possible to prevent strong fluctuations in the number of confined electrons. A well-defined number of electrons also implies a definite confined charge; i.e.  $N$  times the elementary charge  $e$ . The quantization of charge permits the use of a simple model in which all the electron-electron interactions are captured in the single-electron charging energy  $e^2/C$ , where  $C$  is the capacitance of the dot. This simple model has been successful in describing a wealth of transport phenomena which are generally known as single-electron transport and Coulomb blockade effects [1].

If the tunnel coupling to the leads is increased, the number of electrons on the dot becomes less and less well-defined. When the fluctuations in  $N$  become much larger than unity, the quantization of charge is completely lost. In this open regime, theories of non-interacting electrons usually give a proper description of transport. The theory is much more complicated in the intermediate regime where the tunnel coupling is relatively strong but the discreteness of charge still plays an important role. Here, the transport description needs to incorporate higher-order tunneling processes via virtual, intermediate states. When spin is neglected these processes are known as cotunneling [2]. When one keeps track of the spin it can be convenient to view tunneling as a magnetic exchange coupling. In this case, the physics of a quantum dot connected to leads becomes similar to the physics of magnetic impurities coupled to the conduction electrons in a metal host; i.e. the Kondo effect [3,4]. Recent theory has predicted new Kondo phenomena in quantum dots [5-7]. This unique spin system allows one to study an individual, artificial, magnetic impurity and tune in-situ the parameters in the Kondo problem. The first experimental demonstration for a Kondo effect in quantum dots was recently reported by Goldhaber-Gordon et al. [8]. In the present paper, we report more extensive measurements of the temperature dependence of the equilibrium and non-equilibrium Kondo effect in quantum dots which agree well with the results of reference [8]. In addition, we present data using both perpendicular and parallel magnetic fields which unambiguously identify the Kondo physics, and we demonstrate the tunability of the Kondo temperature with an applied gate voltage.

In order to explain the important parameters for the Kondo effect we use the energy diagrams of Fig. 9.1. We treat the dot as an electron box separated from the leads by tunable tunnel barriers with a single spin-degenerate energy state  $\epsilon_0$  occupied by one electron of either spin up or spin down. The addition of a second

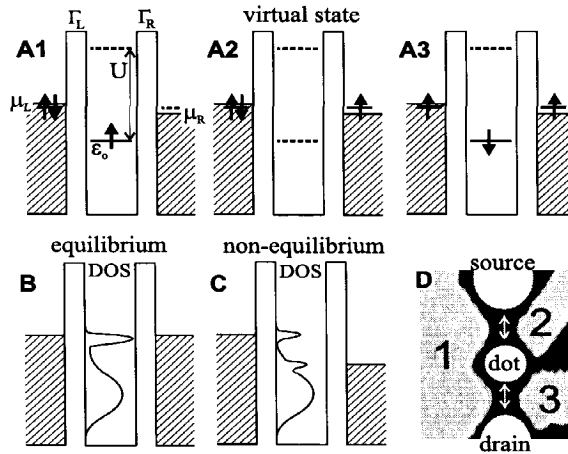


Figure 9.1: a) Schematic energy diagram of a dot with one spin-degenerate energy level  $\varepsilon_0$  occupied by a single electron.  $U$  is the single-electron charging energy, and  $\Gamma_L$  and  $\Gamma_R$  give the tunnel couplings to the left and right leads. The parameters  $\varepsilon_0$ ,  $\Gamma_L$ , and  $\Gamma_R$  can be tuned by the gate voltages. The states in the source and drain leads are continuously filled up to the electrochemical potentials,  $\mu_L$  and  $\mu_R$ . The series (A1, A2, A3) depicts a possible virtual tunnel event in which the spin-up electron tunnels off the dot and a spin-down electron tunnels on the dot. Such virtual tunnel events which involve spin-flips build up a macroscopically correlated state with properties that are known as the Kondo effect. (b) The Kondo effect can be pictured as a narrow resonance in the density-of-states (DOS) of the dot at the Fermi energies of the leads,  $\mu_L = \mu_R$ . The lower energy bump in the DOS is the broadened single particle state  $\varepsilon_0$ . (c) A source-drain voltage  $V$  results in the difference:  $eV = \mu_L - \mu_R$ . For finite  $V$ , the DOS peak splits in two; one peak located at each chemical potential. (d) SEM photo of the gate structure which defines our quantum dots in the two-dimensional electron gas (2DEG) which is about 100 nm below the surface of a GaAs/AlGaAs heterostructure. Dot 1 has an estimated size of 170 nm x 170 nm and confines  $\sim 60$  electrons while dot 2 is about 130 nm x 130 nm containing  $\sim 35$  electrons (see ref. 13 for more details). We measure Coulomb oscillations by simultaneously sweeping the voltages on gates 1 and 3.

electron to this state costs an on-site Coulomb energy  $U = e^2/C$ . In the case of Fig. 9.1a first-order tunneling is blocked. An electron cannot tunnel onto the dot since the two electron energy  $\varepsilon_0 + U$  exceeds the Fermi energies of the leads,  $\mu_L$  and  $\mu_R$ . Also, the electron on the dot cannot tunnel off because  $\varepsilon_0 < \mu_L, \mu_R$ . This blockade of tunneling is known as the Coulomb blockade (CB) [1]. In contrast to first-order tunneling, higher-order processes in which the intermediate state costs an energy of order  $U$  are allowed for short time-scales. In particular, we are interested in virtual tunneling events which effectively flip the spin on the dot. One such example is depicted in Figs. 9.1a(1,2,3). Successive spin-flip processes effectively screen the local spin on the dot such that the electrons in the leads and on the dot together form a spin-singlet state. This macroscopically correlated state gives rise to the Kondo effect, which is well-known from low-temperature resistivity measurements on metals containing a small fraction of magnetic impurities [9]. In a quantum dot, the Kondo effect can be described as a narrow peak in the density-of-states (DOS) at the electrochemical potentials of the leads,  $\mu_L = \mu_R$ , as shown in Fig. 9.1b [3-7]. This Kondo resonance gives rise to enhanced conductance through the dot. Out of equilibrium, when a bias voltage  $V$  is applied between the source and drain,  $eV = \mu_L - \mu_R$ , the Kondo peak in the DOS splits into two peaks, each pinned to one chemical potential (Fig. 9.1c) [5,7]. This splitting leads to two specific features in transport. First, at zero magnetic field, the differential conductance  $dI/dV$  versus  $V$  mimics the Kondo resonance in the DOS, so a peak in  $dI/dV$  is expected around zero voltage. Second, a magnetic field lifts spin degeneracy resulting in a  $dI/dV$  versus  $V$  showing two peaks at  $eV = \pm g\mu_B B$  [5,10], where  $g$  is the Landé factor and  $\mu_B$  is the Bohr magneton.

Figure 9.1d shows the gate structure of our GaAs/AlGaAs quantum dot devices. Negative voltages applied to the gates control the parameters  $\varepsilon_0$ , the electron number  $N$ , and  $\Gamma_L, \Gamma_R$ , the energy broadening of the discrete states due to the coupling to the left and right leads. The conductance shows CB oscillations on varying the gate voltage  $V_g$ ; see for example Fig. 9.2a. Although the exact number of electrons  $N$  is not known, each period corresponds to a change of one electron on the dot.  $N$  should thus oscillate between an even and an odd number. If we assume spin-degenerate filling of the single-particle states [11], the total spin on the dot is zero when  $N = \text{even}$  (i.e. all states are double occupied with anti-parallel spins) while for  $N = \text{odd}$  the total spin is  $\pm \frac{1}{2}$  (i.e. the topmost state is singly occupied with either spin up or down). In other words, for even  $N$  the dot is non-magnetic while for odd  $N$  the dot has a net spin magnetic moment [12]. This property allows quantum dots to be tuned between a Kondo and a non-Kondo system as we vary  $N$  with the gate voltage.

Measurements were made on two quantum dots of similar shape (Fig 9.1d)

[13] in a dilution refrigerator with an effective electron base temperature  $T_{base} \sim 45$  mK [14]. The spin coupling interactions which give rise to Kondo physics contribute significantly only for temperatures comparable to or lower than the Kondo temperature  $T_K \sim [U \Gamma]^{1/2} \exp[-\pi(\mu - \varepsilon_0/2\Gamma)]$ , where  $\Gamma = \Gamma_L + \Gamma_R$  [15]. To make this regime accessible experimentally,  $\Gamma$  is made as large as possible by setting the gate voltages  $V_g$  such that the broadened CB oscillations in Fig. 9.2a slightly overlap. This implies that  $\Gamma \sim \Delta$  where  $\Delta$  is the single-particle level spacing measured as 0.1 meV and 0.15 meV in dots 1 and 2 respectively [16]. The respective Coulomb energies in the weak tunneling regime were measured as  $U = 1$  meV and 1.3 meV.  $U$  decreases by a factor of  $\sim 2$  in the stronger coupling regime of our measurements [17].

The dc conductance  $G = I/V$  from dot 1 is shown in Fig. 9.2a for electron temperatures of 45 and 150 mK. The base temperature ( $T_{base} \sim 45$  mK) measurement shows even-odd peak spacings (inset, Fig. 9.2b) which arise from the filling of spin-degenerate energy states. The energy cost to add an odd numbered electron onto an unoccupied energy state of the dot is the Coulomb energy plus the single particle spacing,  $U + \Delta$ , while the energy is only  $U$  to add an even electron to fill the same energy state. Although the absolute value of  $N$  is not known, we obtain the parity of the electron number for the valleys in Fig. 9.2a from the even-odd spacings together with magnetic field measurements [11]. We note that valleys with smaller peak spacings ( $N = \text{odd}$ ) also have a larger base temperature conductance than their neighbors, a result of the Kondo peak in the DOS enhancing the valley conductance when  $N = \text{odd}$ . Comparing the valley conductances, we see that valleys 3, 5 and 7, decrease when  $T$  is increased to 150 mK, while the even valleys increase. This even-odd effect is illustrated in more detail in Fig. 9.2b where we plot the change in valley conductance with temperature,  $\delta G_{valley}(T) = G_{valley}(T) - G_{valley}(T_{base})$ . While all the valley conductances for  $N = \text{even}$  increase with  $T$ , for  $N = \text{odd}$  the spin-correlation is destroyed by an increasing  $T$  such that  $G_{valley}$  first decreases. The minimum in  $\delta G_{valley}$  strongly resembles the resistance minimum in metallic Kondo systems [9].

Measurements on dot 2 also show agreement with expectations of the Kondo effect. The middle valley in Fig. 9.3a is identified as a "Kondo" valley because it shows a larger base temperature conductance than the neighboring valleys. The detailed  $T$  dependence in Fig. 9.3b shows that this Kondo valley also has a minimum conductance around 200 mK. Furthermore, the conductance peaks on either side of the Kondo valley decrease and move apart with increasing  $T$  (see also Fig. 9.3b) in qualitative agreement with theory [4,5]. The motion of the peak position, which has not been previously reported, is attributed to a renormalization of the non-interacting energy state  $\varepsilon_0$  due to fluctuations in  $N$ .

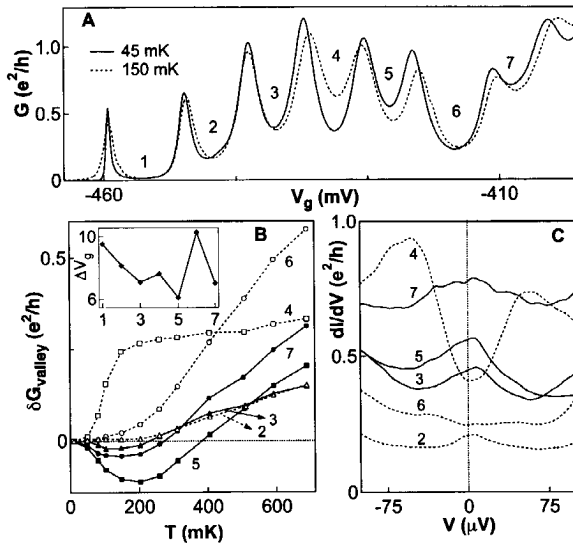


Figure 9.2: a) Linear response conductance  $G = I/V$  versus gate voltage  $V_g$  measured in dot 1 at  $B = 0$  for  $V = 7.9 \mu V$  at 45 mK (solid) and 150 mK (dashed). The parity of the valley numbering is indicated by an odd or even number of  $N$ . From left to right, the CB peaks become broader (i.e.  $G$  is increasing) because the tunnel barrier induced by gates 1 and 2 decreases when increasing the voltage on gate 1. Increasing  $T$  from 45 to 150 mK increases the conductance of the even numbered valleys but decreases the conductance of valleys 3, 5 and 7. The detailed temperature dependence is shown in (b) where we plot the change in valley conductance  $\delta G_{\text{valley}}(T) = G_{\text{valley}}(T) - G_{\text{valley}}(T_{\text{base}})$  with  $T_{\text{base}} \sim 45$  mK. The inset to (b) shows the spacings  $\Delta V_g$  between adjacent peaks. We observe a larger (smaller) peak spacing for even (odd)  $N$ . (c) Differential conductance,  $dI/dV$ , as a function of  $V$  for the center of each CB valley in (a). The odd valleys have a pronounced zero-bias maximum.

To investigate the Kondo effect out of equilibrium we measure the differential conductance  $dI/dV$  in the center of the Kondo valley of Fig. 9.3A. At base temperature, the  $dI/dV$  has a peak at  $V = 0$  (Fig. 9.3c, bold curve). The peak has a width  $\sim 50$  mV which is narrow compared to the energy scales of  $U$ ,  $\Delta$ , and  $G$ . Increasing  $T$  broadens the  $dI/dV$  peak until it completely disappears at  $\sim 300$  mK. The insets to Fig. 9.3c give the temperature dependence of the  $dI/dV$  peak maximum on a logarithmic scale and the peak width (the full-width



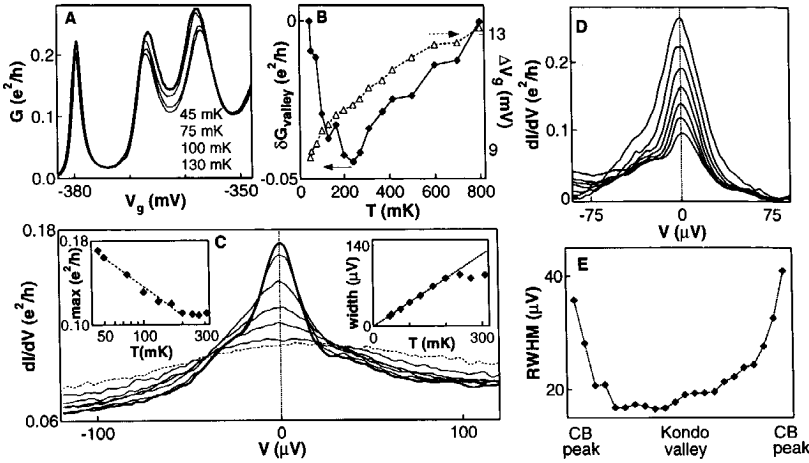


Figure 9.3: *a*) Conductance  $G$  for  $B = 0$  and  $V = 5.9 \mu\text{V}$  at 45 (bold curve), 75, 100 and 130 mK in dot 2. Due to the smaller size of dot 2, the tunnel barriers increase more quickly with negative gate voltage so we can observe only 3 consecutive valleys in the Kondo regime. The middle valley shows pronounced Kondo behavior. This figure shows the dependence on  $T$ ,  $V$  and  $\varepsilon_0$ . *(b)* Left axis:  $\delta G_{\text{valley}}(T)$  (solid diamonds) for the center of the middle, Kondo valley in *(A)*. Right axis: gate voltage spacing  $\Delta V_g(T)$  of the peaks bordering the Kondo valley. Increasing  $T$  results in a Kondo minimum in  $\delta G_{\text{valley}}$ . Simultaneously, we observe an increasing peak spacing which is ascribed to a renormalization of the energy level  $\varepsilon_0$ . *(c)* Differential conductance  $dI/dV$  versus  $V$  for  $T = 45$  (bold), 50, 75, 100, 130, 200, and 270 (dashed) mK. The gate voltage is set in the center of the middle valley. The peak maximum (left inset) is logarithmic in  $T$ . The peak width (the full width at  $\frac{3}{4}$  max, right inset) is linear in  $T$  with a slope of  $4.8 k_B$  (dotted line). The asymmetry in the zero-bias peak is probably because  $\Gamma_L \neq \Gamma_R$ . *(d)* Zero-bias peak in  $dI/dV$  at 45 mK for different gate voltages stepping from the center of the Kondo valley in *(a)* (bottom curve,  $V_g = -363$  mV) up the left side of the CB peak (top curve,  $V_g = -366$  mV). The curves have been shifted so the background values align at  $\sim 75 \mu\text{V}$ . The amplitude of the zero-bias peak increases as the conductance  $G$  increases moving up the flank of the CB peak. *(e)* We measure the right half-width at half-max (RWHM) of the zero-bias peak (relative to the baseline  $dI/dV$  at  $\sim 75 \mu\text{V}$ ) which begins to increase halfway up the CB peak on either side. The increasing width follows the increase of the Kondo temperature  $T_K$  above  $T_{\text{base}}$ . The increase in  $T_K$  results from bringing  $\varepsilon_0$  towards the Fermi energies  $\mu_L = \mu_R$  by tuning the gate voltages.

at  $\frac{3}{4}$  max) on a linear scale. The logarithmic  $T$  dependence of the maximum is expected for  $T_K \lesssim T$  [3]. At low temperatures, the width is expected to saturate at  $\sim T_K$ . We do not observe such saturation which suggests that  $T_K < 45$  mK in the middle of the Kondo valley.

In order to increase  $T_K \sim [U \Gamma]^{1/2} \exp[-\pi(\mu - \varepsilon_0/2\Gamma)]$ , we decrease the distance between  $\varepsilon_0$  and the Fermi energy by moving away from the Kondo valley towards a neighboring CB peak. The zero-bias  $dI/dV$  peak is seen to increase in both height and width when tuning  $\varepsilon_0$  towards the Fermi energy (Fig. 9.3b). The width of the  $dI/dV$  peak, shown in Fig. 9.3e, is determined by the larger of  $T_K$  or  $T$ . The increase in width when approaching the CB peaks on either side of the Kondo valley indicates that here  $T_K$  exceeds  $T$ . Figure 9.3e demonstrates the first control of  $T_K$  in a Kondo system. The largest value we obtain for  $T_K$  can be estimated from the largest  $dI/dV$  peak in Fig. 9.3d. From a width of  $\sim 80 \mu\text{V}$  we get  $T_K \sim 1$  K.

The absence and presence of a zero-bias peak for  $N =$  even or odd, respectively can be seen in the  $dI/dV$  measurements for the valleys of dot 1 in Fig. 9.2c. Valleys 3, 5 and 7 indeed have a narrow zero-bias peak. Valley 4 has a minimum in the  $dI/dV$  [18] while valley 6 has a flat  $dI/dV$ . Note that valley 2 shows a slight maximum at  $V = 0$ . This could arise from a dot with a net spin of  $\pm 1$  instead of 0. Occasionally we observe small shoulders on the sides of peaks in  $dI/dV$ . It is yet unclear whether these shoulders are related to the fact that our dots have multiple levels [16].

A magnetic field  $B_{\parallel}$  in the plane of the two-dimensional electron gas (2DEG) splits the spin-degenerate states of the quantum dot by the Zeeman splitting,  $\varepsilon_{\pm} = \varepsilon_0 \pm g\mu_B B_{\parallel}/2$ . When the dot has an unpaired electron, the Kondo peak in the DOS at each chemical potential is expected to split by twice the Zeeman energy,  $2g\mu_B B_{\parallel}$  [5]. In equilibrium, there is no longer a peak in the DOS at  $\mu_L = \mu_R$ , and the zero-bias conductance is not enhanced. Instead, one expects the peak in  $dI/dV$  to be shifted to a finite bias:  $V = \pm g\mu_B B_{\parallel}/e = \pm 25 \mu\text{V}/\text{T}$ , where  $g = -0.44$  for bulk GaAs. In Fig. 9.4a we show that indeed the zero-bias peak splits into two peaks when we increase  $B_{\parallel}$  from 0 to 7 T. The peak positions, shown in Fig. 9.4b, fall directly on top of the theoretical prediction,  $\pm 25 \mu\text{V}/\text{T}$  (dashed lines) [19].

The correct splitting of the  $dI/dV$  peak with magnetic field has been heralded as the most distinct sign of Kondo physics [5]. Probing the Zeeman doublet single-particle state with the differential conductance could also reveal a peak split linear in  $B_{\parallel}$ . However, in this case, the splitting is gate voltage dependent. A gate voltage independent peak split by  $2g\mu_B B_{\parallel}$  distinctively identifies the Kondo effect with no free parameters. Figures 9.4d and 9.4e show a grayscale plot of the

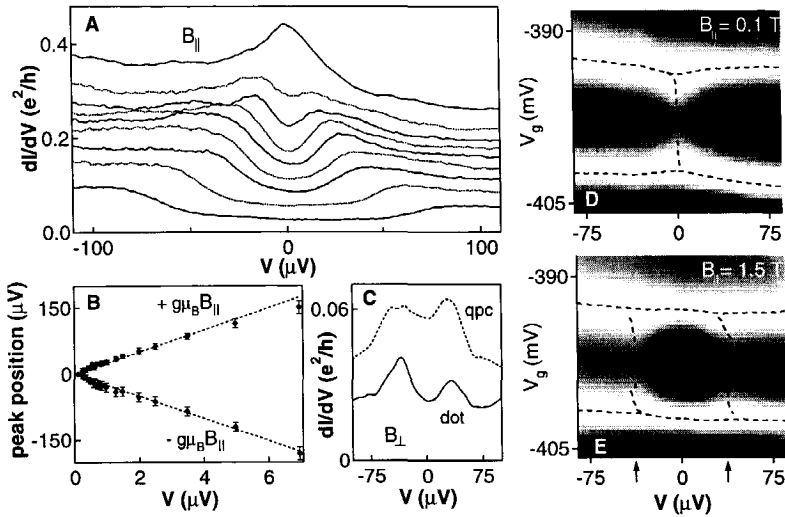


Figure 9.4: a) The splitting of the zero-bias peak in the differential conductance  $dI/dV$  with a magnetic field  $B_{\parallel}$  in the plane of the 2DEG. From top to bottom:  $B_{\parallel} = 0.10, 0.43, 0.56, 0.80, 0.98, 1.28, 1.48, 2.49,$  and  $3.49$  Tesla. The curves are offset by  $0.02 e^2/h$ . Above  $\sim 0.5$  T we resolve a splitting which increases linearly with  $B_{\parallel}$ . (b) Position, in bias voltage, of the  $dI/dV$  maxima as a function of  $B_{\parallel}$  up to 7 T. The dashed line indicates the theoretical splitting of  $\pm 2g\mu_B B/e \pm 25 \mu V/T$  with  $g = -0.44$  for GaAs. (c) Split peaks at  $36 \mu V/T$  are observed in the  $dI/dV$  of the quantum dot and also in a single point contact (qpc) (formed by a negative voltage on gates 1 and 3 only) in a perpendicular magnetic field  $B_{\perp} = 1.89$  T. The Landau level filling factor is 4 at this field in the bulk 2DEG. Measurements at other  $B_{\perp}$  and in other qpcs also showed similar structure. In contrast, the  $dI/dV$  of a qpc in high  $B_{\parallel}$  is flat. (d, e) Grayscales of  $dI/dV$  as a function of  $V_g$  and  $V$  show the zero-bias peak for  $B_{\parallel} = 0.1$  T split into two shoulder peaks at  $B_{\parallel} = 1.5$  T. This valley is the Kondo valley from Fig. 9.3a. The contour of the CB peaks (horizontal) and the maxima in the  $dI/dV$  (vertical) are indicated by dashed lines. The valleys on either side of the Kondo valley do not show a zero-bias or split  $dI/dV$  peak. The arrows on the bottom axis of (e) indicate the theoretical splitting, which should be independent of  $V_g$ , with a value of  $\pm 37.5 \mu V$  at  $B_{\parallel} = 1.5$  T. The arrows matches the experimental results very well.

$dI/dV$  as a function of  $V$  and  $V_g$  over a Kondo valley. The maximum of the CB peaks (horizontal) and the Kondo  $dI/dV$  peak (vertical) are indicated by dashed lines. In both Fig. 9.4d and 9.4e, the maxima in  $dI/dV$  occur only for the Kondo valley and not for the neighboring valleys. We point out that the location of the split maxima for  $B_{||} = 1.5$  T are independent of  $V_g$  throughout the valley.

Peaks in  $dI/dV$  reported in [8] were split by  $33 \mu\text{V/T}$  in a magnetic field  $B_{\perp}$  perpendicular to the plane of the 2DEG. This value, significantly smaller than the expected  $50 \mu\text{V/T}$ , could be a result of the formation of quantum Hall states in the leads. Figure 9.4c shows the  $dI/dV$  at  $B_{\perp} = 1.89$  T for both our quantum dot (solid) and a single quantum point contact (dashed). Note that each shows split peaks in  $dI/dV$  at  $36 \mu\text{V/T}$ . The point contacts of both our dots showed significant structure around  $\sim 35 \mu\text{V/T}$  in a perpendicular magnetic field. What might cause a field dependent splitting in the  $dI/dV$  of a quantum point contact is unclear. However, the orbital changes caused by  $B_{\perp}$  severely complicate the identification of Kondo physics in a perpendicular magnetic field. Furthermore, with the formation of spin-polarized Landau levels in the leads, a single electron on the dot cannot equally couple to both spin states in the leads which should suppress the Kondo resonance.

In conclusion, we have presented a coherent dataset illustrating the Kondo effect in quantum dots. We have demonstrated the tunability of the Kondo effect between valleys with even and odd numbers of electrons. As well, we have shown that the Kondo temperature in a quantum dot can be tuned with a gate voltage, and we have directly measured the Kondo peak in the DOS at  $B_{||} = 0$  and the split Kondo peaks at  $B_{||} \neq 0$ .

We thank R. Aguado, B. Broer, L. I. Glazman, S. F. Godijn, K. K. Likharev, C. M. Marcus, J. E. Mooij, and N. C. van der Vaart for help and discussions and Philips Laboratories and C. T. Foxon for providing the heterostructure. This work was supported by the Dutch Foundation for Fundamental Research on Matter (FOM), L.P.K by the Royal Netherlands Academy of Arts and Sciences, and S.M.C. by the NSF under grant DMR-945805.

## References

- [1] For a review, see L. P. Kouwenhoven et al., *Mesoscopic Electron Transport*, Proceedings of the NATO Advanced Study Institute, L. Sohn, L. P. Kouwenhoven, G. Schön, Eds., Curaçao, 25 June to 5 July 1996 (Series E, 345, 105, Kluwer, Dordrecht, Netherlands, 1997). Also available online at <http://vortex.tn.tudelft.nl/~leok/papers/>.

- [2] For a review on cotunneling see D. V. Averin and Yu. V. Nazarov, Single Charge Tunneling, Proceedings of a NATO Advanced Study Institute, H. Grabert and M. H. Devoret, Eds., Les Houches, France, 5 March to 15 March, 1991 (Series B, 294, 217, Plenum Press, New York, 1991).
- [3] L. I. Glazman and M. É. Raikh, Pisma Zh. Eksp. Teor. Fiz. 47, 378 (1988) [JETP Lett. 47, 452 (1988)].
- [4] T. K. Ng and P. A. Lee, Phys. Rev. Lett. 61, 1768 (1988); A. Kawabata, Journal Phys. Soc. Japan 60, 3222 (1991).
- [5] Y. Meir, N. S. Wingreen, P. A. Lee, Phys. Rev. Lett. 70, 2601 (1993); N. S. Wingreen and Y. Meir, Phys. Rev. B 49, 11040 (1994).
- [6] S. Hershfield, J. H. Davies, J. W. Wilkins, Phys. Rev. Lett. 67, 3720 (1991).
- [7] J. König, J. Schmid, H. Schoeller, G. Schön, Phys. Rev. B 54, 16820 (1996); For further references see H. Schöller Mesoscopic Electron Transport, Proceedings of the NATO Advanced Study Institute, L. Sohn, L. P. Kouwenhoven, G. Schön, Eds. (Series E, 345, 291, Kluwer, Dordrecht, Netherlands, 1997).
- [8] D. Goldhaber-Gordon et al., Nature 391, 156 (1998).
- [9] J. Kondo in Solid State Physics, H. Ehrenreich, F. Seitz, D. Turnbull, Eds. (Academic, New York, 1969), vol. 23, p. 183.
- [10] D. C. Ralph and R. A. Buhrman, Phys. Rev. Lett. 72, 3401 (1994); I. K. Yanson et al., Phys. Rev. Lett. 74, 302 (1995).
- [11] In measurements of the evolution of the CB peaks versus  $B$  we observe pairing in the motion between adjacent peaks. This indicates spin-degenerate filling of the energy states which is in contrast to the results of D. R. Stewart et al., Science 278, 1784 (1997) who report non-spin-degenerate filling of the energy states.
- [12] Y. Wan, P. Phillips, Q. Li, Phys. Rev. B 51, 14782 (1995).
- [13] The two quantum dots form the double dot structure discussed in detail by N. C. van der Vaart et al., Phys. Rev. Lett. 74, 4702 (1995). Each dot was measured independently by biasing only the gate voltages that define a single dot.
- [14] Measurements were taken using a variable dc bias and/or an ac bias of 1  $\mu$ V at 13.5 Hz for lock-in detection. The effective electron base temperature,  $T_{base} \sim 45$  mK, was measured from CB peak widths in the weak tunneling regime.

- [15] N. E. Bickers, *Rev. Mod. Phys.* 59, 845 (1987).
- [16] The presence of more than one state in our dots is expected to enhance the Kondo temperature. For an analyses of multiple level effects see T. Inoshita et al., *Phys. Rev. B* 48, 14725 (1993); T. Inoshita, Y. Kuramoto, and H. Sakaki, *Superlattices and Microstructures* 22, 75 (1997); T. Pohjola et al., *Europhys. Lett.* 40, 189 (1997).
- [17] E. B. Foxman et al., *Phys. Rev. B* 47, 10020 (1993).
- [18] The  $dI/dV$  minimum of valley 4 resembles the form predicted by J. König, H. Schöller, and G. Schön, *Phys. Rev. Lett.* 76, 1715 (1996) for a quantum dot with  $N = \text{even}$ .
- [19] Note that our data fit well to the theoretical predictions using the g-factor for bulk GaAs,  $g = -0.44$ , whereas the g-factor in the 2DEG of a typical GaAs/AlGaAs heterostructure has been experimentally determined to be smaller than in the bulk by M. Dobers, K. v. Klitzing, G. Weimann, *Phys. Rev. B* 38, 5453 (1988).

# Summary

This thesis presents an experimental study of the transport properties of semiconductor quantum dots. Vertical and lateral quantum dots are investigated. The vertical quantum dots are etched from a semiconductor double-barrier heterostructure (DBH) and a metal gate electrode is deposited around it. Electrons are confined on the dot in all three dimensions. The surface potential together with the gate potential confines the electrons in the lateral  $x$ - and  $y$ -directions while the DBH provides the confinement in the growth  $z$ -direction. The lateral quantum dots are defined in the two dimensional electron gas (2DEG) of GaAs/AlGaAs heterostructures by means of metallic gates, which are fabricated on top of the heterostructure. Applying negative voltages to the gates depletes the electron gas underneath them and forms an isolated island of electron gas in the 2DEG.

The islands of confined electrons in both systems are weakly coupled to the leads by tunnelbarriers. The addition of a single electron, charges the dot by the elementary charge  $e$ . This costs a finite charging energy  $e^2/C$ , where  $C$  is the capacitance between the dot and its surroundings. At low temperatures, this charging energy can block the current through the island and give rise to Coulomb oscillations in the conductance, as a function of the voltage on one of the gates.

In chapter 2, we use single-electron tunneling spectroscopy to probe electronic states of a few-electron vertical quantum dot-atom. At zero magnetic field the addition energy reveals a shell structure associated with a 2D harmonic potential. As a function of magnetic field, current peaks evolve in pairs, arising from the antiparallel filling of spin-degenerate states. Close to zero magnetic field, however, this pairing behavior is altered to favour the filling of states with parallel spins in line with Hund's rule. The results are in good agreement with an extended constant interaction model. For the system with two electrons  $N = 2$ , we investigate a singlet-triplet transition. In this case the extended constant interaction is not sufficient to explain the value of the magnetic field at which the transition occurs.

In chapter 3, a study of the ground and excited states in quantum dots containing 1 to 12 electrons shows that the quantum numbers of the states in the excitation spectra can be identified and compared to exact calculations. A magnetic field induces transitions between ground and excited states. These transitions are discussed in terms of crossings between single-particle states, singlet-triplet transitions, spin polarization, and Hund's rule. These impurity-free quantum dots

allow "atomic physics" experiments to be performed in magnetic field regimes not accessible for atoms.

In chapter 4, we have measured electron transport at high magnetic fields, through a vertical quantum dot with up to 40 electrons. Over some region in magnetic field the electrons are spin polarized and occupy successive angular momentum states, i.e. the maximum density droplet (MDD) state. The stability region where the MDD state is the ground state, decreases for increasing electron number. The instability of the MDD is accompanied by a redistribution of charge which increases the area of the electron droplet.

In chapter 5, we study the magnetic field evolution of the energy states in lateral rather than in vertical quantum dots. To quantify the evolution of the energy states we look at their magnetization, i.e. the derivative of the energy of a state with respect to the magnetic field. To obtain sharper resonances of the states and thereby a better energy resolution we have measured two quantum dots in series.

In chapter 6, we have used photon-assisted tunneling to study the interaction between microwave light and electrons occupying discrete zero dimensional (0D) states in a single lateral quantum dot. We have measured photon-assisted tunneling through a quantum dot with 0D-states. For photon energies smaller than the separation between 0D-states we observe photon sideband resonances of the ground state. When the photon energy exceeds the separation between 0D-states we observe photon induced excited state resonances. We identify the different resonances by studying their dependence on photon frequency, magnetic field and power.

In chapter 7, two quantum dots are connected to form an 'artificial molecule'. Depending on the strength of the inter-dot coupling, the two dots can have an ionic binding (i.e. electrons are localized on the individual dots) or a covalent binding (i.e. electrons are delocalized over both dots). The covalent binding leads to a bonding and an anti-bonding state with an energy splitting proportional to the tunnel coupling. In the dc current response to microwave excitation, we observe a transition from an ionic bonding to a covalent bonding, when we vary the inter-dot coupling strength.

In chapter 8, the double quantum dot device is used as a tunable two-level system for electronic energy states. A dc electron current directly measures the rates for elastic and inelastic transitions between the two levels. For inelastic transitions, energy is exchanged with bosonic degrees of freedom in the environment. The inelastic transition rates are well described by the Einstein coefficients, relating absorption with stimulated and spontaneous emission. The most effectively coupled bosons in the specific environment of our semiconductor device



are acoustic phonons. The experiments demonstrate the importance of vacuum fluctuations in the environment for little circuits of coherent quantum devices.

In chapter 9, we demonstrate a tunable Kondo effect realized in small quantum dots. We can switch our dot from a Kondo system to a non-Kondo system as the number of electrons on the dot is changed from odd to even. We show that the Kondo temperature can be tuned by means of a gate voltage as a single-particle energy state is shifted relative to the Fermi energy. Measurements of the temperature and magnetic field dependence of a Coulomb-blockaded dot, show good agreement with predictions of both equilibrium and non-equilibrium Kondo effects.



# Samenvatting

In dit proefschrift wordt een experimenteel onderzoek beschreven aan de elektrische eigenschappen van halfgeleider quantum dots. Zowel verticale als laterale quantum dots worden bestudeerd. De verticale dots zijn pilaartjes die geëetst zijn uit een dubbele barrière heterostructuur. Hieromheen is een metalen gate gedeponereerd. Electronen in de dot zijn dan in drie dimensies opgesloten. De dubbele barrière heterostructuur sluit de electronen op in de z-richting, tussen de twee barrières. De oppervlakte potentiaal gecombineerd met de potentiaal die veroorzaakt wordt door de gate sluit de electronen op in de x en y richting. De laterale quantum dots zijn gedefinieerd in een twee dimensionaal electronen gas (2DEG) gemaakt van een GaAs/AlGaAs heterostructuur. Boven dit 2DEG, aan het oppervlak van de heterostructuur, zijn metalen gates aangebracht. Door een negatieve spanning op deze gates te zetten kunnen de electronen weggedrukt worden in het 2DEG eronder. Hierdoor kan een eilandje van elektronen gemaakt worden in het 2DEG.

De eilandjes van opgesloten elektronen zijn zowel in de verticale als laterale dots zwak gekoppeld aan de buitenwereld via tunnelbarrières. Als er een extra electron op een van de dots gebracht wordt dan wordt de dot opgeladen. Dit heeft tot gevolg dat de potentiaal van de dot stijgt met een waarde  $e^2/2C$ , de ladings energie, waarin  $C$  de capaciteit is van de dot naar de omgeving. Bij zeer lage temperatuur kan deze ladingsenergie ervoor zorgen dat geleiding door de dot oscillaties vertoont als de spanning op een van de gates wordt veranderd. Deze oscillaties worden Coulomb oscillaties genoemd.

In het tweede hoofdstuk van dit proefschrift gebruiken we een spectroscopie techniek gebaseerd op enkel-electron-tunneling, om de elektronische toestanden van een verticale dot met weinig electronen te bestuderen. Als er geen magneetveld aanwezig is dan vertoont de additie-energie die betaald moet worden om een extra electron toe te voegen een schillenstructuur die overeenkomt met een twee dimensionale harmonische potentiaal. Brengen we langzaam een magneetveld aan, dan bewegen de Coulomb pieken zich in paren als functie van dit magneetveld. Dit komt doordat elke elektronische toestand met twee electronen (met tegengestelde spin) wordt gevuld. Op sommige punten echter is het voordeliger om electronen met gelijk georiënteerde spin te vullen, volgens de regel van Hund. Deze resultaten zijn in goede overeenstemming met een model gebaseerd op constante interactie tussen de electronen. Voor het systeem met twee electronen is ook de de singlet-triplet overgang bestudeerd. In dat geval is het constante interactie model niet voldoende om de overgang te verklaren.

In hoofdstuk 3 worden de grondtoestanden en geëxciteerde toestanden in

quantum dots, gevuld met 1 tot 12 electronen, bestudeerd. Er kunnen quantumgetallen toegekend worden aan de verschillende toestanden en deze kunnen goed vergeleken worden met exacte berekeningen. Het aanbrengen van een magneetveld zorgt voor overgangen tussen de grondtoestand van een electron en zijn geëxciteerde toestand. Deze overgangen worden verklaard in het kader van het kruisen van enkele deeltjes-toestanden, singlet-triplet overgangen, spin polarisatie en de gegeneraliseerde regel van Hund. Deze quantum dots, die nauwelijks tot geen verontreinigingen hebben, bieden de mogelijkheid om 'atoomfysica' te beoefenen in een magneetveldgebied dat niet in echte atomen toegankelijk is.

In hoofdstuk 4 wordt het transport van electronen gemeten in verticale quantum dots bij hoog magnetisch veld. De dot bevat tot 40 electronen. Over een bepaald gebied in magneetveld zijn alle electronen spin-gepolariseerd en vullen opeenvolgende baanimpulsmoment-toestanden op. Dit wordt de maximale dichtheid druppel (MDD) genoemd. Het magneetveldgebied waarin deze MDD toestand de grondtoestand is, neemt af als het aantal electronen in de dot toeneemt. Als de MDD toestand instabiel wordt, dan gaat dit gepaard met een herverdeling van de lading in de dot, die tot gevolg heeft dat de electronen in de dot over een groter gebied verspreid zijn.

In hoofdstuk 5 wordt de magneetveld afhankelijkheid van toestanden in laterale quantum dots bestudeerd. Om de afhankelijkheid van energietoestanden te quantificeren wordt gekeken naar de afgeleide van de energie naar het magneetveld. Om scherpere resonanties te krijgen, die een betere energieresolutie tot gevolg hebben, is gekeken naar twee laterale dots in serie.

In hoofdstuk 6 zijn tunnelprocessen die geïnduceerd worden door fotonen bestudeerd, om te kijken naar de interactie tussen (microgolf-) licht en discrete nul dimensionale toestanden in een enkele laterale dot. Als de energie van de fotonen kleiner is dan de energieopsplitsing tussen 0D toestanden, dan zijn er 'sideband' resonanties van de grondtoestand zichtbaar. Als de energie van de fotonen de 0D opsplitsing overschrijdt, dan zijn resonanties te zien die overeenkomen met de aangeslagen toestanden van de dot. Verschillende resonanties zijn te verklaren door hun afhankelijkheid te volgen, van het magneetveld en van de frequentie en intensiteit van het microgolfveld.

In hoofdstuk 7 zijn twee laterale dots op een dusdanige manier met elkaar verbonden dat een 'kunstmatig molecuul' gevormd wordt. Afhankelijk van de koppeling tussen de dots hebben de dots een ionische binding (waarbij de electronen zijn gelokaliseerd op een van de individuele dots) of een covalente binding (waarbij de electronen zijn gedelokaliseerd over beide dots). De covalente binding heeft tot gevolg dat de energie opsplijst in een symmetrische en een anti-symmetrische. De opsplitsing is afhankelijk van de koppeling tussen de dots. De dc-stroom ten

gevolge van microgolfstraling laat een overgang zien van een ionische naar een covalente binding als de koppeling tussen de dots wordt gevarieerd.

In hoofdstuk 8 wordt een dubbele dot gebruikt als een instelbaar twee niveau systeem voor electronische energie toestanden. Een dc-stroom meet direkt de overgangswaarschijnlijkheid van de elastische en inelastische overgangen tussen de twee niveau's. Voor inelastische overgangen wordt er energie uitgewisseld met de Bosonische vrijheidsgraden in de omgeving. De inelastische overgangswaarschijnelijkheden worden goed beschreven door de Einstein coëfficiënten die de absorptie relateren aan gestimuleerde en spontane emissie. De meest efficiënt gekoppelde Bosonen in de omgeving van het halfgeleider systeem dat wij hebben doorgemeten zijn acoustische phononen. De experimenten laten zien dat vacuumfluctuaties in de omgeving van zeer kleine coherente quantum systeem belangrijk zijn.

In hoofdstuk 9 is een controleerbaar Kondo effect gerealiseerd in een kleine quantum dot. De dot kan veranderd worden van een Kondo systeem in een niet-Kondo systeem als het aantal elektronen op de dot veranderd wordt van een oneven in een even aantal elektronen. De Kondo temperatuur kan gevarieerd worden door de spanning op de gate te veranderen en daarmee de enkele deeltjes toestanden te verschuiven ten opzichte van de Fermi energie. Metingen als functie van magneetveld en temperatuur van een dot in het Coulomb blokkade gebied vertonen goede overeenkomsten met voorspellingen van Kondo effecten in evenwicht en in niet-evenwicht situaties.



# Curriculum Vitae

Tjerk H. Oosterkamp

- 9-10-1972      Born in Eindhoven, The Netherlands.
- 1983-1988      V.W.O. at the 'Stedelijk Gymnasium', Arnhem.
- 1988-1990      Los Gatos High School, Los Gatos, California.
- 1990-1994      M.Sc. Applied Physics,  
Delft University of Technology.  
Graduate research in the Quantum Transport group of  
prof. dr. ir. J. E. Mooij.  
Subject: Moving vortices in charged Josephson-junction  
arrays.
- 1994-1998      Ph.D. research,  
Delft University of Technology, Applied Physics  
Quantum Transport group of prof. dr. ir. J. E. Mooij.  
Subject: Electron transport through Quantum dots.





## List of publications

1. *Photon-assisted tunneling through a quantum dot.*

T.H. Oosterkamp, L.P. Kouwenhoven, A.E.A. Koolen, N.C. van der Vaart, and C.J.P.M. Harmans.

Semicond. Sci. and Technol. **11**, 1512-1515 (1996).

2. *Photon-assisted tunneling through discrete states in a quantum dot.*

T.H. Oosterkamp, L.P. Kouwenhoven, and C.J.P.M. Harmans.

Proceedings for the International Conference on the Physics of Semiconductors (ICPS Berlin, 1996), p. 1569-1572, M. Scheffler and R. Zimmermann eds. (World Scientific, Singapore 1996).

3. *Photon sidebands of the ground state and first excited state of a quantum dot.*

T.H. Oosterkamp, L.P. Kouwenhoven, A.E.A. Koolen, N.C. van der Vaart, and C.J.P.M. Harmans.

Phys. Rev. Lett. **78**, 1536-1539 (1997).

4. *Photon induced resonances in the current through a quantum dot with zero-dimensional states.*

T.H. Oosterkamp, L.P. Kouwenhoven, A.E.A. Koolen, N.C. van der Vaart, and C.J.P.M. Harmans.

Physica Scripta **T69**, 98-102 (1997).

5. *Coulomb oscillations in few-electron quantum dots.*

L.P. Kouwenhoven, T.H. Oosterkamp, S. Tarucha, D.G. Austing, and T. Honda. Proceedings of the International conference on Electronic Properties of Two Dimensional Electron Gasses (EP2DS), Tokyo, September 20-24 1997.

Physica B **249-251**, 191-196 (1998).

6. *Excitation spectra of circular few-electron quantum dots.*

L.P. Kouwenhoven, T.H. Oosterkamp, M.W.S. Danoesastro, M. Eto, D.G. Austing, T. Honda, and S. Tarucha.

Science **278**, 1788-1792 (1997); See also cond-mat/9708229.

7. *Changes in the magnetization of a double quantum dot.*

T.H. Oosterkamp, S.F. Godijn, M.J. Uilenreef, Y.V. Nazarov, N.C. van der Vaart, and L.P. Kouwenhoven.

Phys. Rev. Lett. **80**, 4951-4954 (1998); See also cond-mat/9802118.

8. *Electronic states in quantum dot atoms and molecules.*

S. Tarucha, T. Honda, D.G. Austing, Y. Tokura, K. Muraki, T.H. Oosterkamp, J.W. Janssen, and L.P. Kouwenhoven.

Proceedings of the Mauterndorf Winterschool, Austria, February 23-27 1998.

9. *A tunable Kondo effect in quantum dots.*

S.M. Cronenwett, T.H. Oosterkamp, and L.P. Kouwenhoven.

Science **281**, 540-544, (1998); See also cond-mat/9804211.

10. *Microwave spectroscopy on a quantum-dot molecule.*

T.H. Oosterkamp, T. Fujisawa, W.G. van der Wiel, K. Ishibashi, R.V. Hijman, S. Tarucha, and L.P. Kouwenhoven.

Nature **395**, 873-876 (1998).

11. *Electron ground states in a few-electron quantum dot.*

T.H. Oosterkamp, W.G. van der Wiel, L.P. Kouwenhoven, D.G. Austing, T. Honda and S. Tarucha.

Proceedings of the German Physical Society meeting in Regensburg, March 26 1998. To appear in Advances in Solid State Physics.

12. *Several- and many-electron artificial-atoms at filling factors between 2 and 1.*

G. Austing, Y. Tokura, T. Honda, S. Tarucha, M. Danoesastro, J. Janssen, T. Oosterkamp, and L.P. Kouwenhoven.

Submitted to Jpn. J. Appl. Phys., June 1998.

13. *Singlet-triplet transitions in a few-electron quantum dot.*

W.G. van der Wiel, T.H. Oosterkamp, J.W. Janssen, L.P. Kouwenhoven, D.G. Austing, T. Honda, S. Tarucha.

Physica B **256-258**, 173-177 (1998).

14. *Coupling effects in semiconductor double quantum dots in the Coulomb Blockade regime.*

K. Ishibashi, T.H. Oosterkamp, R.V. Hijman, L.P. Kouwenhoven.

Submitted to Jpn. J. Appl. Phys. (1998).

15. *Stability of the maximum density droplet in quantum dots at high magnetic fields.*

T.H. Oosterkamp, J.J. Janssen, L.P. Kouwenhoven, D.G. Austing, T. Honda and S. Tarucha.

Submitted to Phys. Rev. Lett. (1998)

16. *Spontaneous emission spectrum in double quantum dot devices.*

T. Fujisawa, T.H. Oosterkamp, W.G. van der Wiel, B. Broer, R. Aguado, S. Tarucha and L.P. Kouwenhoven.

Science 282, 932-935 (1998).

